Control of particle properties in low-pressure radio frequency gas discharges

Doctoral Thesis

by

Benedek Horváth

prepared in

Wigner Research Centre for Physics, Budapest, Hungary

under the supervision of

Dr. Aranka Derzsi, PhD, Senior Research Fellow

Head of Doctoral School: *Head of Doctoral Programme:*

Prof. Jenő Gubicza   Prof. Gábor Horváth

Doctoral School of Physics

Programme for Statistical Physics, Biological Physics and Physics of Quantum Systems

Eötvös Loránd University

July 2023

Acknowledgements

This thesis could not have been prepared without the work and support of many people. I am grateful to all of them.

First of all, to Aranka Derzsi, my supervisor, for mentoring me during all the years of my scientific work. I am grateful for all our discussions, for being thorough and precise while also supportive and patient.

To Zoltán Donkó, who was my first teacher in plasma physics and a second mentor during my scientific career, and was always available for a discussion.

To Julian Schulze, who always had some ideas how to improve my paper.

To my colleagues Peter Hartmann and Ihor Korolov, for contributing to the results.

Finally, to my family, especially my wife Zsófi, for all her support and patience.

Contents

Abbreviations

CCP	capacitively coupled plasma
RF	radiofrequency
PIC/MCC	particle-in-cell/Monte Carlo collisions
PROES	phase-resolved optical emission spectroscropy
PE	primary electron
SE	secondary electron
SEE	secondary electron emission
DA	drift-ambipolar
TVW	tailored voltage waveform
FWHM	full width at half maximum

Chapter 1

Introduction

1.1   Background and motivation

Plasmas are gas phase systems containing free charged particles. The electrostatic forces among the particles and the possible collision processes between the wide range of plasma particles (electrons, ions, metastables, photons, cosmic particles) and neutral gas atoms/molecules (if such particles are present) make the system complex, consisting of a number of sub-systems between which the degree of coupling varies significantly. Since approximately 99 % of the known matter in the universe is in the plasma state, an outstandingly wide variety of plasmas exists in nature. Several kinds of plasmas are represented in figure 1.1, in the plane of charged particle density and temperature. The charged particle density varies within a range of 30 orders of magnitude, and the temperatures cover 10 orders of magnitude. The plasma with the lowest density and temperature is the interstellar gas. The hottest and most dense plasmas are the cores of stars, especially white dwarfs. In Earth, low-density plasmas are observed in the form of Northern lights, when gas particles are ionized by cosmic jets in the ionosphere, the highest region of the atmosphere. Lightning is also an instantaneous gas discharge, and air is in the form of low-density plasma in flames as well.
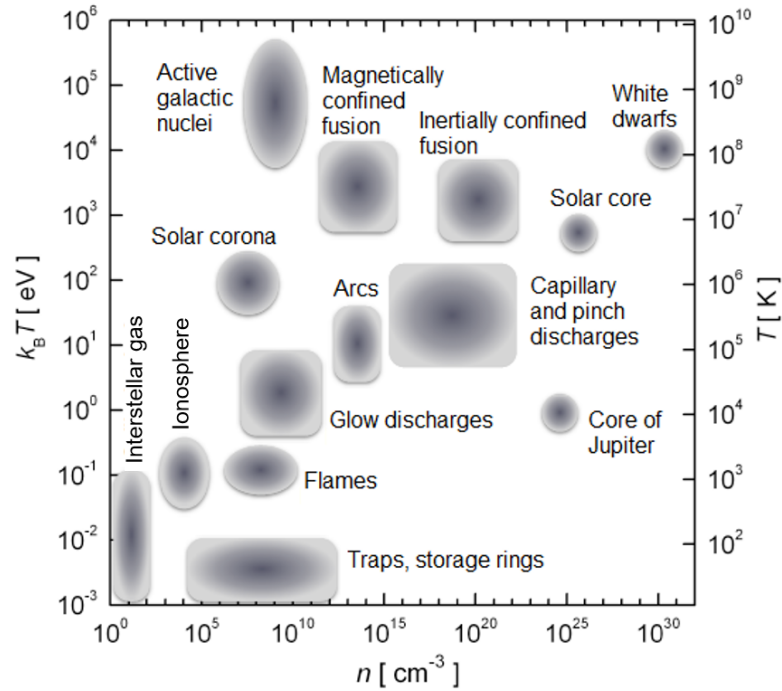
FIGURE 1.1: Plasmas in nature and lab. The horizontal axis corresponds to the density of charged particles and the vertical axes represent the thermal energy of particles (left axis) and the equivalent temperature (right axis) [1].

In laboratory, two main types of plasmas are common: (i) fully ionized high-temperature plasmas, which are magnetically confined and planned to be applied for controlled fusion and (ii) low-ionization-degree electrical gas discharges. In case of electrical gas discharges, the energy supply is provided by electrical power. (These systems usually radiate energy in the form of heat and light.) Based on the type of the driving current, DC and radiofrequency (RF) discharges are differentiated. Among RF discharges, capacitively coupled plasma (CCP) is one of the most wide-spread setups (see an introduction below in section 1.2). In these systems, the charged particle density is typically in the range of $10^{13} - 10^{18}$ m^{-3}, the thermal electron energy is around a few eV and the thermal ion energy is in the range of 10^{-2} eV. In the current thesis, low-pressure CCPs operated in noble gases and molecular gases are studied.

CCPs are essential for various industrial technologies. Plasma etching is a key mechanism in the manufacturing of chips and integrated circuits, plasma deposition is

used for producing various semiconductors (e.g. solar cells) and plasma-based cleaning is widely used for sterilization and manufacturing biocompatible instruments (e.g. prosthetics) [2, 3]. In plasma processing applications, plasmas in reactive gases are used (e.g. oxygen, CF_4, C_2F_8). In these gases, several types of particles are created (electrons, ions, fast neutrals, radicals, metastables) some of which are able to gain high energy. The substrate, located on one of the electrodes, is exposed to bombardment by plasma particles. Consequently, surface processes are of crucial importance in a RF plasma, and industrial applications can be optimized by the efficient control of particle energies and fluxes at the electrodes. A detailed understanding of the physics of CCPs facilitates the knowledge-based optimization of plasma processing applications.

1.2 Capacitively coupled plasmas

Capacitively coupled plasmas (CCPs) are among the most studied discharges. Their investigation is motivated both by their complex physics and their wide range of applications in industry. In CCP sources, the plasma is generated between two (typically plane parallel) electrodes. One of the electrodes is driven by RF voltage and the other electrode is grounded. The driving frequency is typically between 1–100 MHz (the standard frequency being 13.56 MHz allocated for industrial, scientific and medical purposes by the International Telecommunication Union, a United Nations agency). The driving voltage waveform can be of various types, although it is usually sinusoidal (single-frequency waveform) or a superposition of sinusoidal components (dual-frequency or multifrequency voltage waveform, non-sinusoidal tailored voltage waveform). The pressure of the background gas can be set within a wide range: from ≈ 0.1 Pa to atmospheric pressure. Low-pressure and low-temperature CCPs, which are in the focus of the thesis, are typically operated at gas pressures between ≈ 0.1 Pa to a few 100 Pa, at room temperature. The gases in such CCPs are
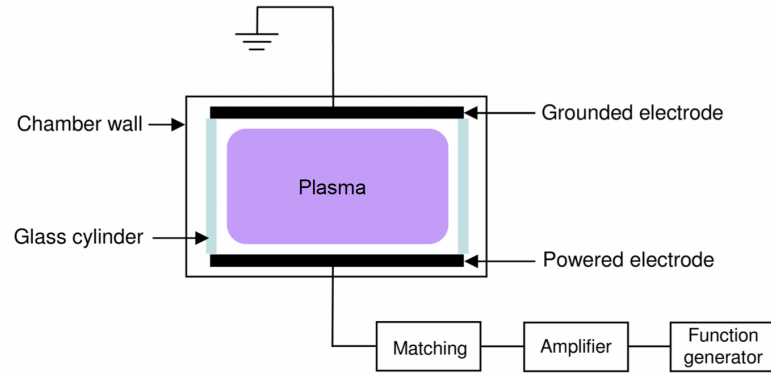
FIGURE 1.2: Sketch of a capacitively coupled RF discharge setup.

weakly ionized, i.e. the plasma density (the density of positively charged particles) is usually between $10^{14} - 10^{16}$ m^{-3}.

The simplest laboratory CCP setup has the plane-parallel geometry. In this case two planar electrodes are located within a vacuum chamber, parallel to each other, resembling to a planar capacitor. A sketch of a capacitively coupled discharge is shown in figure 1.2. The RF driving is realized by multiple electrical units: the function generator is connected to a power amplifier, and a matching box (a tunable capacitive/inductive unit) is applied to optimize the impedance of the circuit in order to maximize the power delivered to the plasma.

In this setup, the diameter of the electrodes (typically $10 - 20$ cm) is usually significantly larger than the distance between them (the electrode gap is typically $1 - 10$ cm). The discharge is geometrically symmetric, if the surface area of the powered electrode is equal to the surface area of the grounded electrode. If the electrode surface areas are different, the discharge is geometrically asymmetric. A photo of a geometrically symmetric capacitively coupled RF discharge is shown in figure 1.3.

As a significant portion of charged particles is lost at the electrodes, their density is naturally low near the electrodes. As a result, a unique density distribution of charged particles develops, characteristic of CCPs: two plasma sheaths are formed
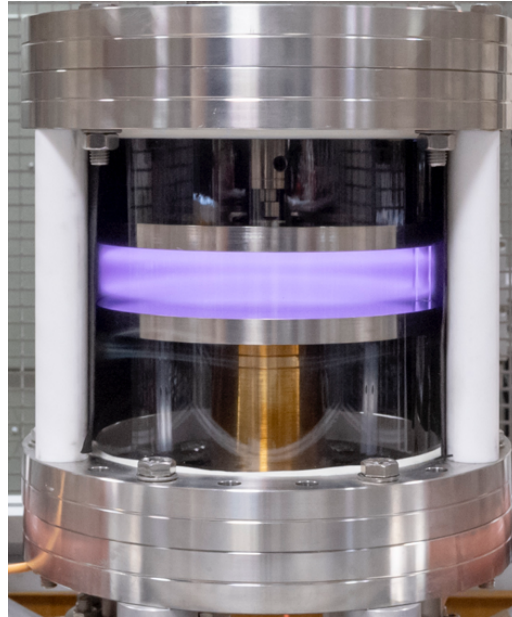
FIGURE 1.3: Photo of a geometrically symmetric capacitively coupled RF discharge, operated in argon gas. This system (the Budapest v3 cell) is set up in the laboratory of the Electrical Gas Discharges Research Group in the Wigner Research Centre for Physics.

near the electrodes with low charged particle density, which are periodically filled and depleted by electrons, making a region of positive charge on time average. A quasi-neutral plasma bulk is formed in the middle with stationary ion and electron density profiles. This is illustrated in figure 1.4 via some particle-in-cell/Monte Carlo collisions (PIC/MCC) simulation results (this computational method will be introduced later in chapter 2) for an argon CCP: the time-averaged density profiles of the electrons and the positive ions (Ar^+) are shown between the electrodes. From now on, x denotes the spatial coordinate in the axial direction (perpendicular to the electrodes) and L corresponds to the distance between the electrodes. The powered electrode is located at $x = 0$, while the grounded electrode is at $x/L = 1$. The powered electrode is connected to a driving voltage

$$\Phi_s(t) = \phi_0 \cos(2\pi f t), \tag{1.1}$$

where t is time, ϕ_0 is the voltage amplitude and f is the RF driving frequency.
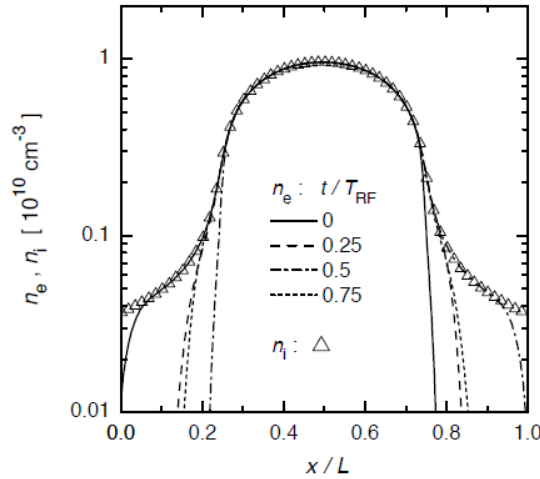
FIGURE 1.4: The density profile of electrons, n_e at different time instances during the RF period and the stationary density profile of ions, n_i in a geometrically symmetric CCP in argon. The powered electrode is located at $x/L = 0$, while the grounded electrode is at $x/L = 1$. Discharge conditions: argon gas, $p = 10$ Pa, $f = 13.56$ MHz, $\phi_0 = 300$ V, $L = 2.5$ cm, where p is the gas pressure and ϕ_0 is the driving voltage amplitude. The results are obtained from PIC/MCC simulations [1].

In case of electrons, the density profile is shown at specific t time instances within the RF period: $t/T_{RF} = \{0,\ 0.25,\ 0.5,\ 0.75\}$, where $T_{RF} = 1/f$ is the duration of the RF period. At $t/T_{RF} = 0$, the electron density is comparable to the density of ions near the powered electrode ($x/L = 0$, except a thin region directly neighbouring the electrode), while in a wider region near the opposite (grounded) electrode (between $0.77 < x/L < 1$) the electron density is completely depleted. Half RF period later (at $t/T_{RF} = 0.5$) the situation is just the opposite at the two electrodes: the electron density is depleted at the powered electrode and it is close to the ion density at the grounded electrode. At the time instances $t/T_{RF} = \{0.25, 0.75\}$ (in the middle of the half periods) a practically symmetric density profile of electrons can be observed. In other words, the sheaths have an expansion and a collapse phase within a RF period at each electrode, and the sheaths at the two electrodes are always in the opposite phase. This is caused by the periodically modulated electric field which becomes high in the sheaths periodically and accelerates the electrons away from the electrodes. This acceleration of electrons during the periodic expansion of the

sheaths is a crucial mechanism in sustaining the RF plasma, as electrons gain energy as a result of it, making a significant portion of them capable of causing ionization. (The electron power absorption of CCPs will be introduced in more detail in chapter 1.2.4.) While the electric field is periodically modulated in the sheaths, it is usually negligible in the quasineutral bulk region in the middle.

1.2.1 Physical characteristics of capacitively coupled plasmas

Debye length   In a quasineutral plasma an electrostatic shielding comes to effect, which can be characterised by the Debye-length:

$$\lambda_{\mathrm{D}} = \sqrt{\frac{\varepsilon_0 k_{\mathrm{B}}}{n_0 e^2} \left(\frac{1}{T_{\mathrm{e}}} + \frac{1}{T_{\mathrm{i}}} \right)^{-1}}, \tag{1.2}$$

where T_{e} and T_{i} are the temperatures of the electron and the ion population. The Debye-length is practically a characteristic length scale of plasmas: it determines the length on which charged particles have electrostatic interaction between each other.

Plasma frequency   In any kind of plasma, an oscillation of charged particles can be observed as particles interact with the electric field. The characteristic frequency of this oscillation is described by the plasma frequency, which is unique for every kind of particle species in the plasma. The oscillation frequency for ions is

$$\omega_i = \sqrt{\frac{n_0 e^2}{m_i \varepsilon_0}}, \tag{1.3}$$

and for electrons is

$$\omega_e = \sqrt{\frac{n_0 e^2}{m_e \varepsilon_0}}, \tag{1.4}$$

where m_i and m_e are the masses of ions and electrons, respectively, and n_0 is the density of the quasi-neutral plasma, i.e. the density of ions and electrons, which are technically equal. Since the mass of any ion is orders of magnitudes higher than the mass of an electron, the oscillation of ions is much slower compared to the electrons. In a CCP, which is driven by RF voltage, the driving frequency, ω_{RF}, is typically significantly higher than the plasma frequency of ions, while it is much lower than the plasma frequency of electrons:

$$\omega_i \ll \omega_{RF} \ll \omega_e. \tag{1.5}$$

As a result of this relation of the driving frequency and the electron/ion plasma frequencies (1.5), electrons can follow the oscillation of the RF driving voltage, while ions cannot. This results in a periodic oscillation of electrons between the electrodes, while the ion density remains stationary. Particles colliding with the electrode surface interact with it via various mechanisms (a detailed introduction on this is presented in section 1.2.3).

Length of the sheaths The positions of the sheath edges near the electrodes can be calculated either analytically or by simulations. A criterion widely used for the definition of the position of the sheath edge is proposed by *Brinkmann* [4]:

$$\int_0^{s(t)} n_e(x', t)dx' = \int_{s(t)}^{L/2} (n_i(x', t) - n_e(x', t))dx', \tag{1.6}$$

where $s(t)$ is the position of the sheath edge relative to the respective electrode, x' is the position relative to the respective electrode within the electrode gap, L is the length of the electrode gap, n_e and n_i are the electron and ion densities. The physical interpretation of this criterion is that the number of electrons within the sheath equals the surplus in the number of ions between the sheath boundary and the middle of the discharge. Typically, the average sheath length $\bar{s}$ is significantly higher than the Debye-length and significantly lower than the length of the bulk

region (L_b):

$$\lambda_{\mathrm{D}} \ll \bar{s} \ll L_b. \tag{1.7}$$

Flux balance All the mechanisms arising in a CCP are ultimately driven by a strict criteria: no DC current can flow in the plasma whenever the plasma source is connected to the RF generator via a blocking capacitor. In a plasma containing only single-charge particles, this is equivalent to the following statement regarding the plasma particle currents: the fluxes of particles with positive and negative charges (electrons and ions in the simplest case) during a RF period have to be equal at both electrodes:

$$\langle \Gamma_+ \rangle_{T_{\mathrm{RF}}} = \langle \Gamma_- \rangle_{T_{\mathrm{RF}}}. \tag{1.8}$$

This has a very important consequence: the discharge can be generated among electrodes with dielectric coating. The latter is crucial in terms of industrial applications, which are typically based on surface modification (etching, sputtering, deposition, cleaning) by energetic plasma particles [2, 3].

Electronegativity Besides electrons and positive ions, the plasmas of our interest can also include negative ions formed in electron attachment or dissociation processes. Low-pressure CCPs can be electropositive or electronegative, depending on the type of the gas, i.e. the charged particle species forming the plasma. The (global) electronegativity is defined as

$$\beta = \frac{n_{i^-}}{n_e}, \tag{1.9}$$

where n_{i^-} is the total density of negative ions (of all kind) and n_{e} is the density of electrons. The electronegativity of low-pressure CCPs ranges from 0 (plasmas without negative ions) up to a few hundreds. Plasmas with $\beta > 1$ are called electronegative, otherwise they are called electropositive.

1.2.2   Gas phase processes

As energetic charged particles are present in a plasma, various collision processes can take place with the background gas (the neutral gas atoms/molecules), and particles of different species can also interact with each other. The number and the type of reactions, as well as their relative occurrence (the cross sections of the elementary processes) depends on the type of the gas.

The universal processes, which take place even in the simplest scenario of a noble gas discharge, are elastic scattering, excitation of atomic/molecular states and ionization. In an elastic process (elastic scattering), the total kinetic energy of the colliding particles remains the same. For example, electrons are scattered on particles of the background gas, which modifies their trajectory. In inelastic processes, in contrast, a significant portion of the kinetic energy of the projectile (given by the threshold energy of the process, which is roughly in the range of 10-20 eV) is absorbed by the target atom/molecule. In an excitation process, the target is elevated to an energetically higher state, and it usually radiates this energy via spontaneous emission. This is the reason why plasma discharges usually emit optically sensible light. Another crucial inelastic process is ionization of a background gas particle. This is the main source channel of charged particles in a low-temperature plasma. Since charged particles are continuously lost with a given rate (primarily at the walls of the chamber and possibly in recombination collisions in the gas), a nonzero ionization rate is needed to sustain the plasma.

These fundamental processes can be caused by electrons and ions as well. The majority of such collisions are usually caused by electrons because they have higher mobility. A specific elastic collision process between an ion and a neutral is charge exchange. In this case, the fast ion is neutralized and the thermal neutral gets ionized. The fast neutrals created in charge exchange can also collide with thermal neutrals thereforward, by means of elastic scattering, excitation and ionization.

In addition to the above, other gas phase processes can also occur and play an important role in the discharge. For example, metastable states can be excited in several gases, and metastables can cause ionization with a high cross section. A specific case of this can take place in gas mixtures: the Penning-ionization, when a metastable species of one gas ionizes a neutral particle of the other species. In reactive molecular gases, several additional processes can take place: rotational excitation, vibrational excitation, dissociation, detachment and attachment, various types of recombination etc. Some of them will be discussed in chapter 4.

1.2.3   Surface processes

In a gas discharge, plasma particles interact with the walls of the chamber. In a plane-parallel CCP, the vast majority of such interactions takes place at the electrode surfaces. The most important plasma-surface interaction process is secondary electron emission (SEE), which can be induced by the impact of various particles (e.g. ions, fast neutrals, electrons, metastable atoms/molecules, photons) via various mechanisms: potential emission (if the recombination energy of the ion to the neutral ground state is at least two times higher than the work function, Auger neutralization and the emission of a secondary electron can occur), kinetic emission (when the kinetic energy of the fast heavy particle is absorbed at the electrode surface), field emission (when a high electric field develops in the plasma near the electrode surface, "pulling" electrons outwards the electrode material) or photoemission. The sputtering of the electrode is also an important surface process, which is especially relevant for applications. Other types of surface processes can take place in reactive molecular gases, e.g. surface quenching of metastables.
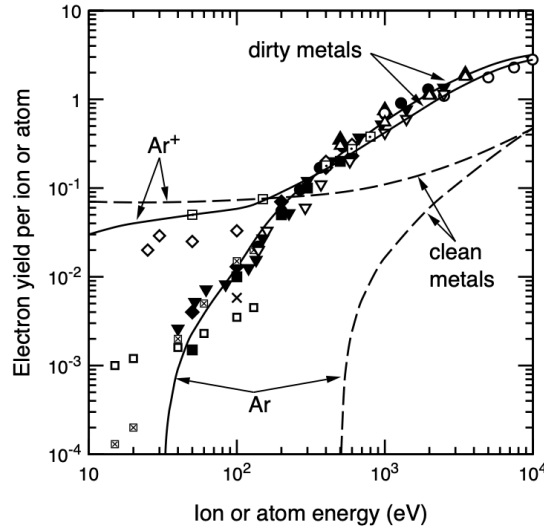
FIGURE 1.5: Electron yields for Ar^+ and Ar beams incident on various dirty (oxidized, lab conditions) metal (including Pt, Ta, Au, Cu, W, brass and CuBe) surfaces versus particle energy. The open symbols are for Ar^+ and the solid symbols are for Ar. The solid and dashed curves are analytical fits for dirty (contaminated, oxidized or having an adsorbed layer) surfaces and clean (atomically clean, sputtered) surfaces, respectively, for Ar^+ and Ar, reproduced from [5].

1.2.3.1 Heavy particle – surface interaction

One of the most important plasma-surface interaction processes is SEE induced by heavy particles, i.e. ions, fast neutrals or metastables. Heavy particles upon impact on the wall can induce the emission of secondary electrons (SEs) from the surface. The ratio of the number of SEs emitted from the surface (N_{SE}) and the number of incoming ions (N_i) is called the effective ion-induced SEE coefficient:

$$\gamma = \frac{N_{SE}}{N_i}. \tag{1.10}$$

SEs induced by heavy particles are often called γ-electrons. The γ coefficient depends on the energy of the heavy particle, and the function form is affected by the type of the particle impinging the electrode, the electrode material and the surface conditions (e.g. roughness). For a given particle type and gas, the energy-dependent γ coefficient can be determined empirically. To illustrate this, the γ coefficient for Ar^+ and Ar (fast atoms) at various surfaces are shown in figure 1.5 based on [5].

Note that heavy particle energies typically range up to a couple of hundreds of eV in the discharges studied in the thesis.
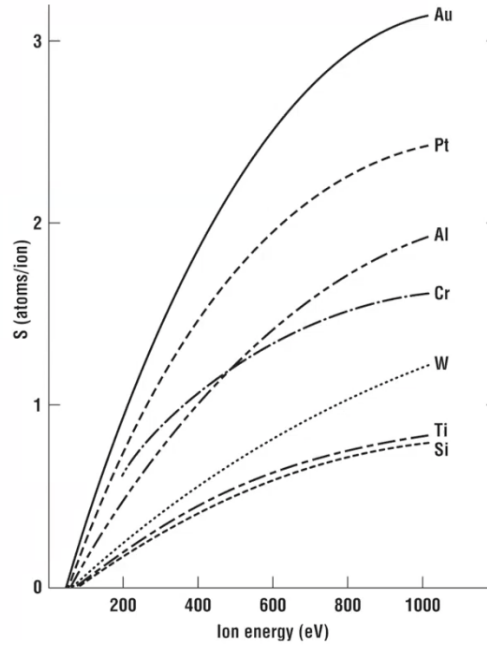
FIGURE 1.6: Sputtering yield as a function of the ion energy for normal incidence of Ar^+ ions, for a variety of materials, reproduced from [6].

Energetic heavy particles can also cause the sputtering of the electrode material, i.e. atoms can escape from the electrode upon impact of ions and fast neutrals originating from the plasma. The flux of sputtered atoms is determined by the flux and energy distributions of heavy particles bombarding the electrode. In figure 1.6 the sputtered particle yield is shown as a function of the incident ion energy, for various metals and silicon based on [6]. The sputtered atoms can interact with other species present in the discharge and can become ionized. The sputtering process plays an important role in many plasma processing applications, where the spatial distribution of sputtered species, their transport and collisions with other plasma species, as well as the optimal conditions for sputtering are key issues.

1.2.3.2 Electron – surface interaction

Electron-induced SEE is an ordinary mechanism in various systems in laboratory. It serves as the basis of the imaging of surfaces, e.g. in scanning electron microscopes [7]. The electron induced SEE is also important in stationary plasma thrusters [8–13]. Models for electron induced SEE assume that the total yield of SEs upon impingement of primary electrons (PEs) on the surface consists of three components: (i) elastically (specularly) reflected electrons having the same energy as before reaching the electrode, (ii) inelastically reflected electrons, which lose part of their energy upon impact on the electrode, their velocity having an isotropic distribution and (iii) electron induced SEs (true SEs or δ-electrons) [14–18], which escape from the electrode material. About 90 % of the emitted electrons are electron induced SEs, escaping the surface with energies from a few to a few tens of eV [16, 17]. The SE yield is measured by

$$\sigma = \frac{\Gamma_{\text{SE}}}{\Gamma_{\text{PE}}}, \tag{1.11}$$

i.e. the ratio of the outgoing SE flux to the incoming PE flux. Experimental data for σ as a function of the PE energy typically have the shape shown in figure 1.7: at low energies of the PEs σ increases rapidly, reaches a maximum value at a few hundreds of eV, then slowly decreases towards high PE energies.

While the general shape of the SEE yield as a function of the PE energy is similar for many different surface materials, the emission maxima (σ_{max}) and the PE energy corresponding to it (ε_{max}) vary over wide ranges: the emission maxima is typically below 2 for metals and it can reach values even above 10 for some oxides, while the energy of maximum emission is usually between 100 eV and 1000 eV [16, 21]. In CCPs studied in the current work, electron impact energies at the electrode surfaces can reach a few hundreds of eV. Note that the SEE curve varies according to the physical properties of the surface (e.g. surface roughness and cleanness), and the PE's angle of incidence also matters at smooth surfaces: σ_{max} and ε_{max}
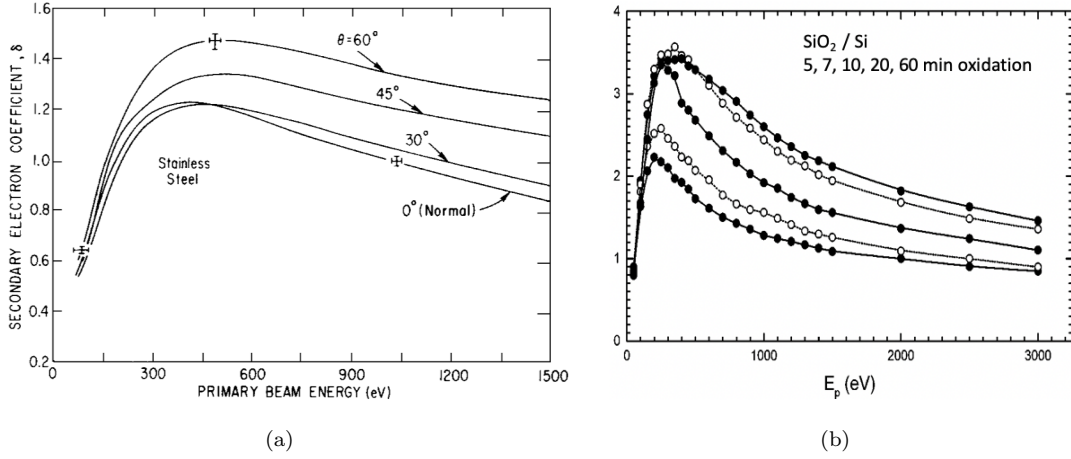
FIGURE 1.7: Electron induced SEE as a function of the PE's energy (a) for stainless steel at four different angles of incidence [19] and (b) for thin SiO_2 layers on a Si substrate for different oxidation times (from the bottom the curves correspond to 5, 7, 10, 20 and 60 minutes) [20].

are significantly increased for oblique impact [21], see figure 1.7(a). Figure 1.7(b) illustrates that oxydized surfaces tend to be more electron-emissive.

1.2.3.3 Other surface processes

In CCPs operated in different gases under various conditions, additional types of surface processes can take place besides electron emission and sputtering. Particles can be created or lost via various mechanisms at the electrode surface. In reactive molecular gases such as oxygen, the number of metastables and radicals are remarkable. The main loss channel of, e.g., $O_2(a^1\Delta_g)$ metastables is quenching at the surface. The quenching rate depends on the surface conditions, which indirectly has a crucial impact on the plasma dynamics. The main loss channel of O^- ions is associative detachment, i.e. the collision process with metastables:

$$O^- + O_2(a^1\Delta_g) \longrightarrow O_3 + e^-, \tag{1.12}$$
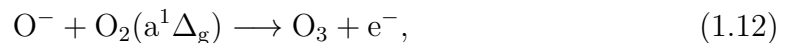
and the density of negative ions determines the electronegativity of the plasma [22].
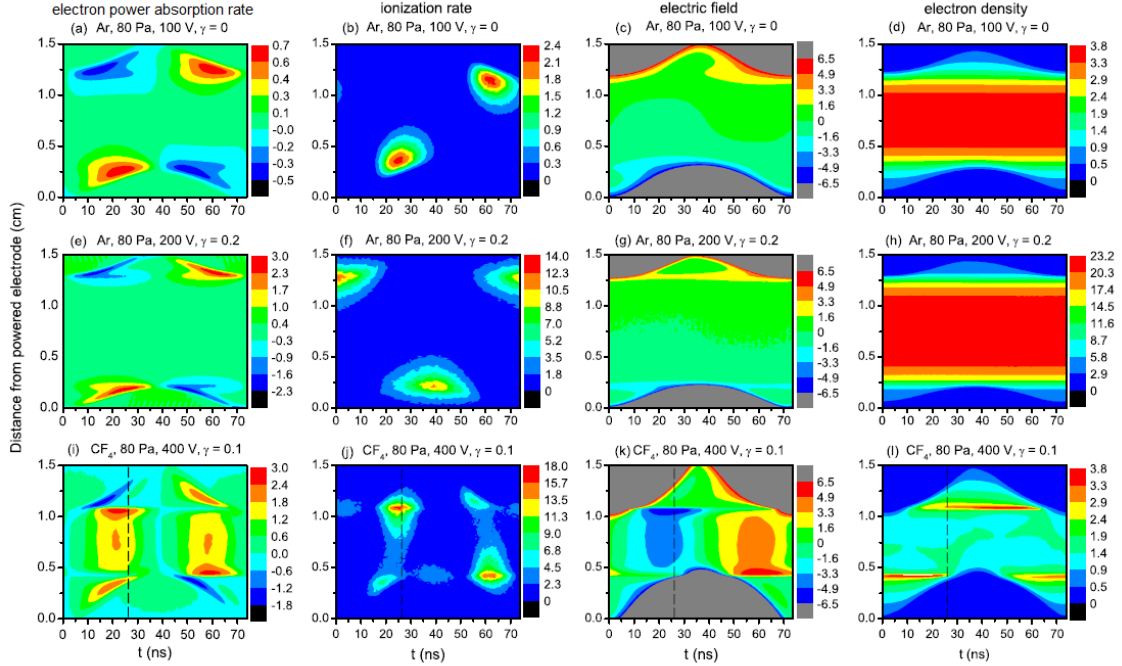
FIGURE 1.8: Spatio-temporal distributions of the electron power absorption rate $[10^5 \text{ Wm}^{-3}]$ (first column), the ionization rate $[10^{21} \text{ m}^{-3}\text{s}^{-1}]$ (second column), the electric field $[10^5 \text{ Vm}^{-1}]$ (third column) and the electron density $[10^{15} \text{ m}^{-3}]$ (fourth column), obtained from PIC/MCC simulations. The horizontal axes correspond to one RF period. The vertical axes show the distance from the powered electrode. The powered electrode is located at $x = 0$, while the grounded electrode is at $x = 1.5$ cm. Discharge conditions: $L = 1.5$ cm, $p = 80$ Pa, $f = 13.56$ MHz. First row: Ar gas, $\phi_0 = 100$ V, $\gamma = 0$. Second row: Ar gas, $\phi_0 = 200$ V, $\gamma = 0.2$. Third row: CF$_4$ gas, $\phi_0 = 400$ V, $\gamma = 0.1$. The figure was originally published in [23].

1.2.4 Electron power absorption modes

One requirement for the sustainment of a CCP is the energy absorption by charged particles, which makes them capable to ionize neutral gas atoms/molecules. As energetic charged particles are lost in collisions or at the electrode surface, the energy absorption is essential. The plasma particles gain their energy from the electric field created by the driving voltage. Since only electrons can follow the RF oscillation of the electric field, electrons are responsible for power absorption. The discharge operation is typically determined by the electron power absorption and electron-impact ionization mechanisms. Under different operating conditions, various electron power absorption mechanisms a.k.a. discharge operation modes can be identified, e.g. α-

[24–30], γ- [24, 31–35] and drift-ambipolar (DA) [23] modes. These are typically defined by the spatio-temporal distribution of the ionization, i.e. the location and the time (within the RF period) of emergent ionization maxima. Characteristic features of the α-, γ- and DA discharge operation modes are illustrated in figure 1.8 [23], in which the spatio-temporal distributions of some plasma parameters (calculated by PIC/MCC simulations, see later in chapter 2) are shown: the electron power absorption (first column), the ionization rate (second column), the electric field (third column) and the electron density (fourth column). The rows correspond to different discharge conditions. In the spatio-temporal plots, time is shown on the horizontal axis, and the vertical axis corresponds to the spatial coordinate. The spatial coordinate maps the whole gap between the electrodes, and it is measured axially (perpendicularly to the two electrodes). The time coordinate maps one RF period. The driving frequency is 13.56 MHz in all cases, resulting in a RF period of 73.74 ns.

The first two rows correspond to CCPs operated in argon, which is an electropositive gas, i.e. the plasma created in it does not contain negative ions. The pressure is 80 Pa and the driving voltage amplitude is 100 V. Under these conditions the electric field in the bulk is close to zero (see panels 1.8(c) and (g)). Meanwhile, in the sheaths, strong electric fields appear, pushing the electrons away from the electrodes. In these argon CCPs, the electrons are mainly accelerated while the sheath expands near one of the electrodes. This can be seen on the spatio-temporal plots of the electron power absorption (panels 1.8(a) and (e)): there are power absorption peaks (red patches) in the first half of the RF period at the powered electrode and in the second half of the RF period at the grounded electrode (see the bottom left and the top right corners of the respective panels). Note that, while electrons are accelerated at one electrode, they are decelerated at the opposite electrode (see the blue patches).

The results in the first row were obtained by setting γ to 0, i.e., neglecting SEE in the simulation. As ionization is typically caused by high-energy electrons in the

discharge (the threshold energy being between $10 - 25$ eV depending on the gas), this localized electron power absorption mechanism results in a localized peak in the ionization at the expanding sheath edge (see panel 1.8(b)). This means that a high number of electrons gain enough energy from the expanding sheath to be able to ionize atoms of the neutral gas. This ionization pattern is called α-mode (the ionization maxima at the expanding sheath is the α-peak), which is typical in electropositive CCPs operated at moderate pressures, moderate driving voltages and negligible SEE from the electrodes.

In the second row, the same plasma parameters as in the first row are shown under somewhat different conditions: the driving voltage is increased to 200 V and the ion-induced SEE coefficient is $\gamma = 0.2$, while all the other conditions are identical to the ones at the first row. In this case, the ionization exhibits a different pattern. Instead of the emergence of an α-peak, a peak appears within the expanded sheath (e.g. in the middle of the RF period at the powered electrode, see panel 1.8(f)). The mechanism behind this is the following: as the ion density is stationary in the sheaths, the ion fluxes reaching the electrodes are also stationary, resulting in stationary ion-induced SE fluxes escaping the electrodes. When the sheath is expanded, the high electric field (see panel 1.8(g)) strongly accelerates the newly generated SEs away from the electrode, providing them enough energy to cause ionization within the sheath. This is called γ-mode discharge operation (and the ionization maxima in the sheath is the γ-peak), emphasizing the crucial role of ion-induced SEs. The spatio-temporal distribution of the electron power absorption, though, looks similar to the one in case of the α-mode (see panel 1.8(e) vs (a)). The reason is that the electron power absorption rate shows a sum of power gain over each electron, while only fast electrons with kinetic energies above the ionization threshold (15.76 eV in case or Ar) contribute to the ionization rate. This selected electron population has a different spatio-temporal distribution compared to the population of all electrons. Namely, they are overrepresented within the sheaths, which are basically depleted by electrons, but γ-electrons are created within the sheaths. Although electron power

absorption near the edges of the expanding sheaths still occurs, the corresponding ionization peak has a significantly lower amplitude compared to that caused by γ-electrons within the sheaths.

In the third row of figure 1.8, the plasma parameters of a CCP operated in CF_4 are shown. Compared to the previous case (second row), the driving voltage amplitude is increased to 400 V, the γ is decreased to 0.1 and the gas is CF_4 instead of Ar. The difference is spectacular compared to the discharges in argon. CF_4 is an electronegative gas, meaning that negative ions (mostly CF_3^- and F^-) are formed in its plasma. Because of this, the population of electrons becomes significantly lower (approximately by an order of magnitude) compared to ions, and quasineutrality is held roughly by the balance of positive and negative ions. The discharge is strongly electronegative. On the other hand, since the plasma frequency of ions is low compared to the driving frequency (see equation 1.5), only the motion of electrons is modulated by the driving voltage, and the RF current driven by the RF voltage can only be conducted by the electrons. According to [23], the DC conductivity of electrons in the plasma (which is a relevant quantity since the relation of the frequencies mentioned above holds) can be calculated as:

$$\sigma = \frac{n_e e^2}{m_e \nu_e},\tag{1.13}$$

where ν_e is the collision frequency of electrons with atoms of the background gas. In an electronegative CCP, the low density of electrons decreases their DC conductivity. In order to conduct the RF current provided by the generator, the collision frequency of electrons has to be low, which corresponds to high velocity. This is provided by a strong electric field in the bulk, which can be seen in figure 1.8(k), and is called drift electric field. In addition to the drift electric field, sharp maxima in the electric field can be seen at the collapsing sheath edges (approximately between 20 ns $< t <$ 30 ns at the grounded electrode and 55 ns $< t <$ 65 ns at the powered electrode), caused by the ambipolar electric field. The effects of the drift and the

ambipolar electric fields can be seen on the electron power absorption rate and the ionization rate as well. In addition to the power absorption and ionization maxima at the expanding sheath edges, like in α-mode, the electrons gain energy from the drift and the ambipolar electric fields and are able to cause ionization throughout the bulk and at the collapsing sheath edge. The absolute maxima of ionization occur at the collapsing sheath edge, due to the ambipolar electric field. This kind of discharge operation dynamics is called the drift-ambipolar (DA) mode, and it is typical in electronegative CCPs.

Note that other types of discharge operation modes are also possible under different discharge conditions. For example, the Ω-mode is typical in atmospheric pressure plasmas, in which ionization in the bulk dominates [36, 37], and the striation mode can be observed in strongly electronegative plasmas, characterised by the resonance of the ion-ion plasma in the bulk region with the driving frequency [38–40].

1.2.5 Control of particle properties

In technological applications of CCPs, the control of the fluxes and energies of ions is crucial. The various applications require high particle fluxes at certain particle energies. For example, etching requires ion energies of hundreds or thousands of eV, while deposition requires tens of eV or less [2, 3, 41]. Consequently, the separate control of particle flux and energy is crucial in industrial applications of CCPs. However, these are coupled in a single-frequency CCP [42]. The ion flux (Γ_i) is proportional to the ion density, which is determined by all the discharge conditions, e. g. the driving frequency and voltage, the gas pressure, the electrode gap etc. Since the electric field is negligible within the bulk, the ion energy (ε_i) distribution depends on the sheath properties. The ratio of the mean free path of ions and the sheath width ($\lambda/\bar{s}$) is a crucial parameter, which is determined by the background gas pressure. The ratio of the particle's time of flight and the RF period (τ/T_{RF}) is also a decisive parameter [1]. This is affected by the mean free path and the driving

frequency. There are two qualitative extremes: (i) high pressure and low frequency and (ii) low pressure together with high frequency. In case (i), the mean free path is short compared to the sheath width ($\lambda/\bar{s} \ll 1$) due to the high pressure, and ions cannot gain high energy because of the frequent collisions with the atoms of the background gas. In case (ii), the mean free path is longer than the sheath width ($\lambda/\bar{s} \gg 1$), i. e. ions fly through the sheaths without collisions, resulting a time of flight significantly shorter than the RF period ($\tau/T_{\mathrm{RF}} \ll 1$). This results in high ion energies at the electrodes, which is slightly modulated by the phase the ions reach the sheath. On the other hand, the ion flux is also affected by the pressure and the frequency. In single-frequency CCPs, the separate control of ions is not possible. It can only be achieved by applying more complicated driving waveforms, which will be introduced in the next sections (1.2.5.1 and 1.2.5.2).

Note that in addition to ions, fast neutrals (atoms or molecules, depending on the gas) can also get high energies and they also play an important role in surface treatment. Fast neutrals are created in elastic charge transfer collisions of a fast ion and a thermal atom:

$$\mathrm{X}^+ + \mathrm{X} \rightarrow \mathrm{X}^{\mathrm{fast}} + \mathrm{X}^+. \tag{1.14}$$

Because their creation is related to ions, the energy distribution of fast neutrals does not differ remarkably from the one of ions.

1.2.5.1 Classical dual-frequency discharges

One method with which separate control of the particle energies and fluxes at the electrodes can be achieved with some limitations is the application of a two-component waveform, which has been widely studied during the last decades [1, 33, 43–52]. Although this approach will not be applied in this thesis, it is briefly discussed here due to its widespread use in laboratory experiments and industrial applications of CCPs.
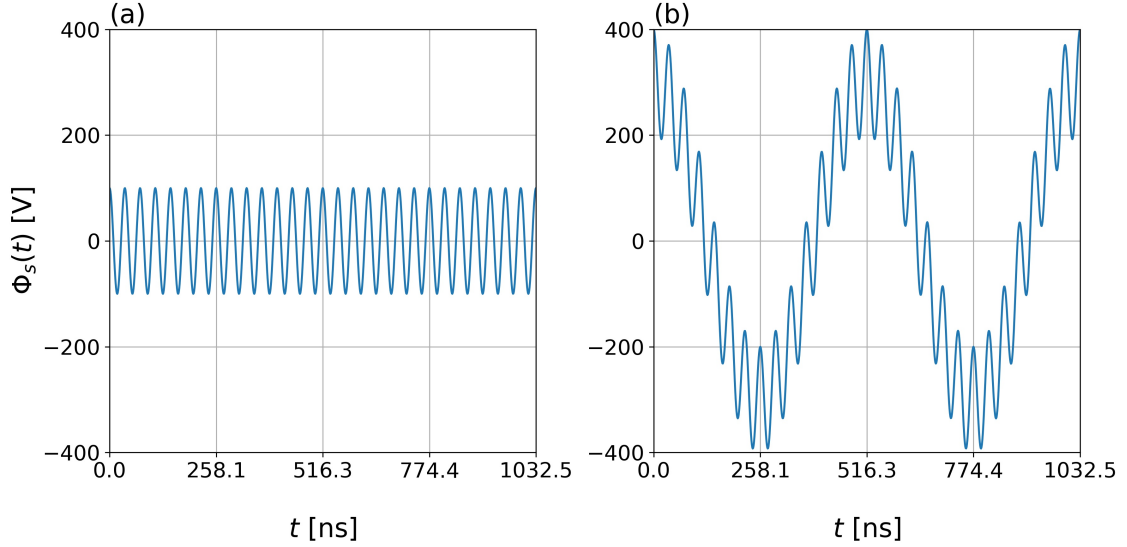
FIGURE 1.9: (a) A single-frequency waveform ($f_h = 27.12$ MHz, $\phi_h = 100$ V) and (b) the formation of a dual-frequency waveform by adding a low-frequency component ($f_l = f_h/14 = 1.937$ MHz, $\phi_l = 300$ V).

The waveform is formed by the superposition of two harmonic signals with frequencies of different orders of magnitude:

$$\Phi_s(t) = \phi_l \cos(2\pi f_l t) + \phi_h \cos(2\pi f_h t), \tag{1.15}$$

where ϕ_l, f_l and ϕ_h, f_h correspond to the voltage amplitude and frequency of the low-frequency and the high-frequency component, respectively. The low frequency usually means a few MHz, while the high frequency is tens or hundreds of MHz. The low-frequency voltage amplitude is usually higher than the high-frequency one: $\phi_l > \phi_h$. The formation of such a waveform is demonstrated in figure 1.9.

The operation mechanism of a CCP driven by a dual-frequency waveform is demonstrated in figure 1.10, showing the spatio-temporal distribution of the ionization rate. As $\phi_l > \phi_h$, the sheath properties are determined by the low-frequency voltage amplitude. This statement is justified by figure 1.10: the sheath expansion and collapse is driven by the low-frequency component. Since the ion energy is determined by the sheath voltage (as it was introduced in the previous section), ϕ_l can serve
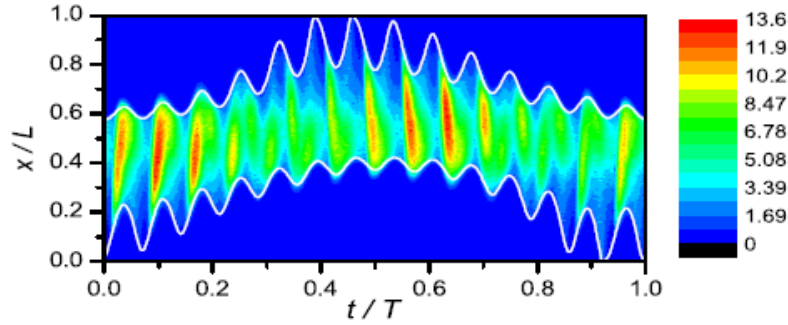
FIGURE 1.10: The spatio-temporal distribution of the ionization rate $[10^{14}$ cm^{-3} s$^{-1}]$ within one low-frequency period. Discharge conditions: argon gas, $p = 6.6$ Pa, $L = 2.5$ cm, $f_h = 27.12$ MHz, $\phi_h = 200$ V, $f_l = 1.937$ MHz, $\phi_l = 500$ V [33].

as a control parameter for the ion energy distribution. However, high-frequency structures also appear in figure 1.10. As the motion of the electrons is modulated by the high-frequency voltage component, they gain energy in each high-frequency period. Thus, the high-frequency voltage amplitude influences the electron power absorption. Electrons accelerated cause ionization efficiently, which increases the particle densities in the plasma and their fluxes at the electrodes. Consequently, ϕ_h serves as a control parameter for the heavy particle fluxes. At first assumption, we have independent control parameters for the ion energy (ε_i) and the ion flux (Γ_i): the voltage amplitudes of the low-frequency (ϕ_l) and the high-frequency (ϕ_h) components, respectively.

The key limitation of the separate control of particle properties in dual-frequency discharges is that the ion flux is not independent of the control parameter of the ion energy, i. e. ϕ_l. This can be seen in figure 1.10 as well: the high-frequency oscillation of the sheath depends on the low-frequency phase [33]. At the expanded phase of the sheath, the amplitude of the high-frequency oscillation is smaller compared to the (partially) collapsed phase due to the locally higher ion density. This decreases the electron power absorption and the ionization rate in the high-frequency expansion phase, limiting the particle fluxes at the electrodes. This mechanism is called frequency coupling [33, 42, 53–58], and it is known as the main limitation of the

separate control of particle flux and energy in dual-frequency CCPs. Another mechanism that limits the separate control is SEE from the electrode surfaces. In case the γ coefficient is high, the discharge operates in γ-mode, and the particle fluxes are no more determined solely by the high-frequency oscillations of the sheaths driven by ϕ_h. Instead, electrons are mostly accelerated within the sheaths, coupling the particle fluxes to the low-frequency voltage (ϕ_l), which is naturally the control parameter of the particle energies. The particle fluxes and energies become coupled to some extent [33, 55].

1.2.5.2 The electrical asymmetry effect in multifrequency discharges

Emergence of asymmetry in CCPs

In this section, a quantitative derivation based on [59] and [60] is presented to elucidate the asymmetry of CCPs.

As it was introduced in chapter 1.2.1, CCPs consist of a quasi-neutral bulk region and two sheath regions, the latter having a net positive charge. Assuming that (i) no voltage drops through the bulk and (ii) the sheaths completely disappear at the collapse phase at each electrode, the voltage balance in the circuit (see figure 1.2) is:

$$\Phi_s(t) + \eta = \Phi_p(t) + \Phi_g(t), \tag{1.16}$$

where Φ_s is the driving voltage, Φ_p and Φ_g are the sheath voltages at the powered and the grounded electrode, respectively, and η is the DC self bias which may appear on the matching unit.

At the extreme phases of the RF period, the sheath voltage is zero at one of the electrodes and takes its maximum at the other electrode. At the two extreme phases, equation 1.16 takes the following forms:

$$\Phi_{s,min} + \eta = \Phi_{p,max}, \tag{1.17}$$

$$\Phi_{s,max} + \eta = \Phi_{g,max}. \tag{1.18}$$

The maximum sheath voltages at the powered/grounded electrode can be calculated via integrating Poisson's equation at the extreme phases, yielding

$$\Phi_{p/g,max} = \mp\frac{1}{2e\varepsilon_0}\left(\frac{Q_{p/g,max}}{A_{p/g}}\right)^2\frac{I_{p/g}}{\bar{n}_{i,p/g}}, \tag{1.19}$$

where $Q_{p/g,max}$ is the maximum charge in the powered/grounded sheath, $A_{p/g}$ is the corresponding electrode area, $\bar{n}_{i,p/g}$ is the mean ion density in the sheath and $I_{p/g}$ is the sheath integral:

$$I_{p/g} = 2\int_0^1 p(x')x'dx', \tag{1.20}$$

with

$$x' = x/s_{max} \tag{1.21}$$

being a normalised coordinate for the spatial position within the sheath (x being the spatial coordinate between the electrodes, s_{max} being the maximum sheath width) and

$$p(x') = n_i(x')/\bar{n}_i \tag{1.22}$$

being a normalised density profile. The negative/positive sign in equation 1.19 corresponds to the sheath at the powered/grounded electrode, respectively. The ratio of the maximum sheath voltages at the two electrodes defines the asymmetry parameter:

$$\epsilon = \left|\frac{\Phi_{g,max}}{\Phi_{p,max}}\right| = \left(\frac{A_p}{A_g}\right)^2\frac{\bar{n}_{i,p}}{\bar{n}_{i,g}}\left(\frac{Q_{g,max}}{Q_{p,max}}\right)^2\frac{I_g}{I_p}. \tag{1.23}$$

In case of a symmetric discharge, when the properties of the two sheaths are equal, $\epsilon = 1$. In any other cases, the discharge is asymmetric. A clear example is the case when the areas of the two electrodes are different, e.g. $A_p \ll A_g$ results in $\epsilon \ll 1$.

With the help of equations 1.17 and 1.18, the DC self-bias can be obtained as

$$\eta = -\frac{\Phi_{s,max} + \epsilon\ \Phi_{s,min}}{1 + \epsilon}. \tag{1.24}$$

According to this expression, a DC self-bias can develop even in geometrically symmetric discharges, i. e. when $\epsilon = 1$: if $|\Phi_{s,max}| \neq |\Phi_{s,min}|$, which is the case when an asymmetric driving waveform is applied. This is called electrical asymmetry.

Voltage waveform tailoring

If the magnitudes of the minima and the maxima of the driving voltage are different ($|\Phi_{s,max}| \neq |\Phi_{s,min}|$), a DC self-bias appears, as it was shown above. Such an asymmetric driving voltage waveform can be set up via the superposition of a base frequency and its harmonics:

$$\Phi_s(t) = \sum_{k=1}^{N} \phi_k \cos(2\pi k f t + \theta_k), \tag{1.25}$$

where N is the total number of harmonics, k is the index of a certain harmonic, ϕ_k and θ_k are the amplitude and the phase shift of that harmonic, respectively. The total voltage amplitude is:

$$\phi_{tot} = \sum_{k=1}^{N} \phi_k. \tag{1.26}$$

The amplitudes of the individual harmonics can be set various ways. Throughout the thesis, the following way is applied [60]:

$$\phi_k = \phi_0 \frac{N - k + 1}{N}, \tag{1.27}$$

with

$$\phi_0 = \frac{2\phi_{tot}}{N + 1}. \tag{1.28}$$

Such driving waveforms are often called tailored voltage waveforms (TVWs). In figure 1.11 multifrequency waveforms are shown for 1, 2, 3 and 4 harmonics. In this example and throughout the thesis, the phase shifts are set to 0 for the odd harmonics, while the phase shifts of the even harmonics are varied, with θ_2 and θ_4 having the same value. At some phase angles the initial sinusoidal (i.e., $N = 1$)
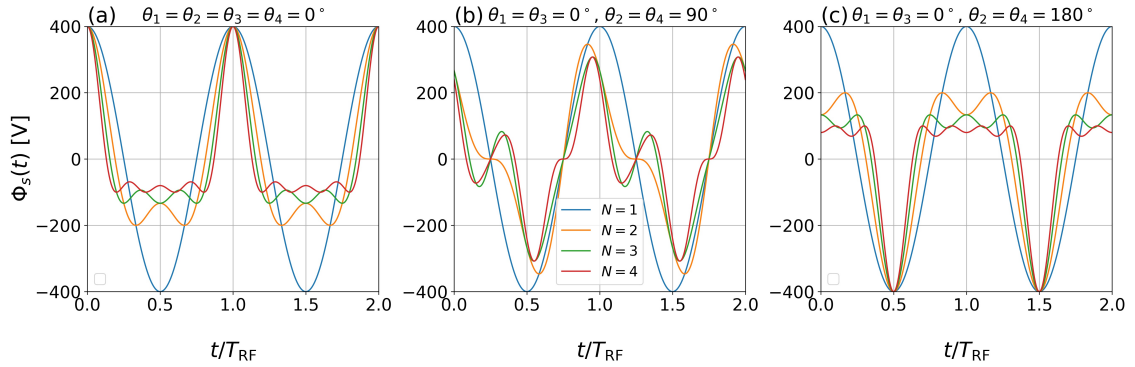
FIGURE 1.11: Multi-frequency waveforms set up via the superposition of a base frequency and its harmonics, according to equation 1.25. $f = 13.56$ MHz, $N = 1 \ldots 4$, $\phi_{tot} = 400$ V. The phase shifts of the odd harmonics are zero, while the phase shifts of the even harmonics are (a) 0°, (b) 90° and (c) 180°.

waveform changes to peaks-like and valleys-like waveforms, which approximate the conditions of pulsed excitation of the plasma.

The application of such multifrequency waveforms to control the particle distribution functions in CCPs have been studied extensively [22, 50, 59–72]. When a CCP is driven by such a multifrequency waveform, a DC self-bias develops due to the electrical asymmetry. This bias depends on the ratio of the time-average of the positive and the negative portions of the driving voltage over one RF period. This ratio can be tuned by changing either the amplitudes or the phase shifts of the individual harmonics [61]. In case the amplitude is modified, the root of the mean square (RMS) of the driving voltage also changes accordingly. On the other hand, when only the phases of the harmonics are varied, the RMS remains the same [61]. This means that the DC self-bias can be adjusted while the plasma parameters are weakly influenced. However, the energy of the heavy particles is directly connected to the DC self-bias: the bias contributes to the time-average electric field within the sheaths, which determines the energy distribution of heavy particles at the electrodes. According to models validated by experiments and simulations [22, 61, 64], the self-bias and the mean ion energy are almost linear functions of the θ_2 phase angle of the second harmonic in a two-component waveform. Generally, the phases of the individual harmonics contributing to the multifrequency waveform serve as
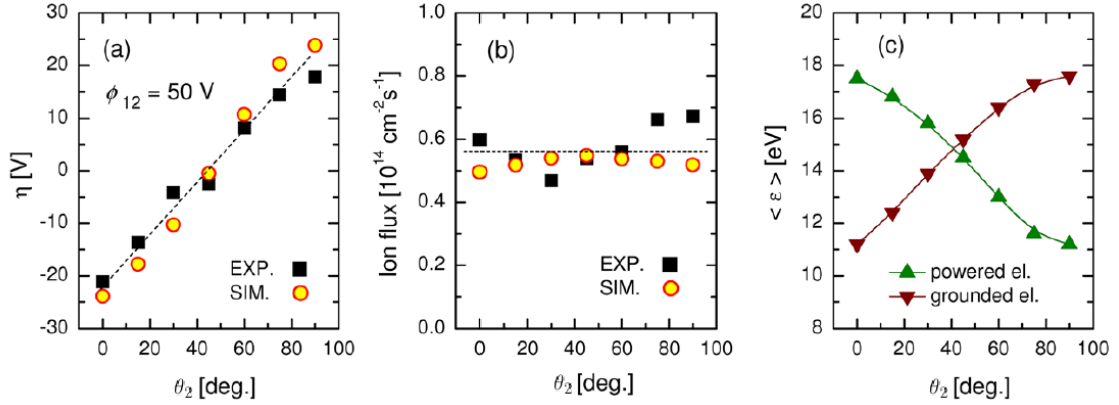
FIGURE 1.12: The DC self-bias, the ion flux at the grounded electrode and the mean ion energy at the two electrodes as functions of the phase angle θ_2. Discharge conditions: $p = 13.3$ Pa, $f = 13.56$ MHz, $N = 2$, $\theta_1 = 0$, $\phi_0 = 50$ V [22].

control parameters of the energy distribution of heavy particles. Meanwhile the flux of heavy particles is hardly affected by θ_k: according to an analytic calculation presented by Schüngel *et al.* [64], the electron power absorption is technically constant as a function of θ_k, as well as the heavy particle densities and their fluxes at the electrodes.

In figure 1.12 the DC self-bias, the ion flux and the mean ion energy are shown at the electrodes as functions of the θ_2 phase shift between the base frequency and its second harmonic in a CCP driven by a two-component driving waveform. Both simulations and experiments confirm that the self-bias can be tuned linearly as a function of the phase shift, and the mean ion energy at the electrodes is nearly linear function of the phase shift as well [22]. While the mean energy at the powered electrode decreases from a maximum to a minimum value as the phase shift is varied between 0 and 180°, it changes the reversed way at the grounded electrode. By shifting the phase with 180°, the mean ion energies at the two electrodes can be reversed. The ion flux is, however, almost constant as a function of θ_2. These findings demonstrate that the separate control of particle fluxes and energies can be achieved in multifrequency discharges (with a generally better performance compared to that of classical dual-frequency discharges described in the previous subsection). The

control parameter for the heavy particle energy at the electrodes is the phase shift between the harmonics.

1.3   Goals and organization of the thesis

The thesis aims at the fundamental understanding of low-pressure RF plasmas operated under various conditions. This allows a scientific approach to the optimization of plasma processing applications. The electron power absorption and ionization dynamics and the role of surface processes in CCPs are addressed in the chapters of the thesis. In order to reach the goals of the current work, modelling and simulation of RF plasmas combined with experiments are performed. The simulations need realistic numerical models for plasma processes, which are developed in the frame of this work. The main topics investigated are the following.

1. In chapter 3, the electron power absorption and ionization dynamics are examined in low-pressure electropositive neon CCPs. A realistic γ coefficient is aimed to be determined for PIC/MCC simulations of CCPs operated in neon, with stainless steel electrodes. At the same time, the applicability of phase-resolved optical emission spectroscopy (PROES) to probe the discharge operation mode will be studied.

2. In chapter 4, low-pressure electronegative oxygen CCPs are investigated. The electrode is made of SiO_2. The effects of surface processes, especially electron-induced SEs and ion-induced SEs on several plasma properties, primarily the plasma density, the electronegativity and the ionization dynamics are studied. Realistic models will be implemented for the interaction of electrons and ions with the electrode surfaces.

3. In chapter 5, the control of particle energies and fluxes at the surfaces in low-pressure multi-frequency argon CCPs is examined. While the previous

chapters present investigations of single-frequency CCPs, this chapter contains studies of RF discharges driven by TVWs. In addition to the realistic modelling of ion-induced and electron-induced SEE, the sputtering of copper electrodes is also considered, by an energy-dependent model. This way the possibility to control the sputtering yield will be examined.

The organization of the thesis is the following: in chapter 2, the computational and experimental techniques used in the thesis will be introduced. In chapters 3-5, the studies announced in the list above will be presented. Finally, the scientific findings will be summarized and synthesized in chapter 6.

Chapter 2

Methods

2.1 Particle-in-cell/Monte Carlo collisions simulation

The particle-in-cell/Monte Carlo collisions (PIC/MCC) simulation is a kinetic many-body simulation method, with which capacitively coupled plasmas (CCPs) can be studied efficiently [42, 73–76]. In such plasmas, the total number of charged particles typically ranges from $\approx 10^8$ to 10^{14}. Due to the high number of particles it is impossible to trace all of them individually and to account for the pairwise interactions between all of them. Therefore, some simplifications are needed to describe the system, while preserving the kinetic approach. The key simplifications applied in the PIC approach are: (i) In order to decrease the number of particles in the simulation, superparticles are defined. These superparticles typically represent $\approx 10^3 - 10^6$ real particles. (ii) Instead of considering pairwise interactions between the particles in the simulation space via a pair-potential (like in molecular dynamics), the electrostatic forces acting on particles are calculated via a meanfield type approximation by using a discrete grid for the calculations. These two ideas are demonstrated in figure 2.1. The PIC approach is complemented with a Monte Carlo method applied
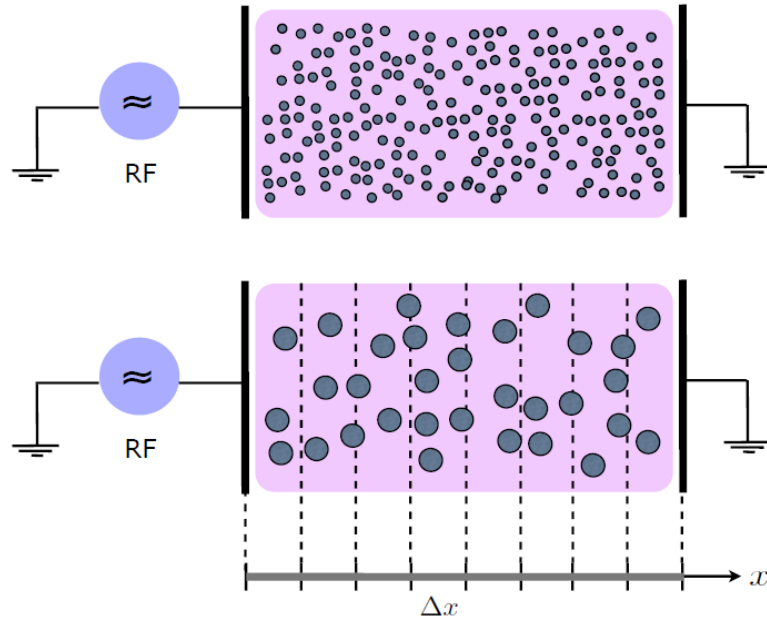
FIGURE 2.1: Demonstration of the idea of using superparticles and an equidistant grid for the calculations in the PIC approach.

for the modelling of collisions in the gas phase. The details of these concepts will be introduced later via the overview of a PIC/MCC simulation cycle. The simulations performed in the frame of this work are one dimensional in space and three dimensional in velocity space (1d3v). As the plasma reactor has a cylindrical geometry and the distance between the electrode plates is much smaller than the electrode radii, using only an axial coordinate in the simulation is sufficient. However, collisions in the plasma occur in the three dimensional space, which requires three coordinates to trace the velocity of the particles. Physically this corresponds to a system with plane and parallel electrodes with infinite area and a discharge cell with infinite radius, which is a reasonable assumption for the CCP reactors studied in this work.

In the simulations, the space between the electrodes is divided into "cells" by equidistant grid points. In the following, the scenario of a PIC/MCC simulation cycle is presented, which is executed at every Δt timestep (this should not be confused with the RF cycle/period, which generally comprises thousands of PIC/MCC cycles). The main steps of the PIC/MCC simulation cycle are shown in figure 2.2.
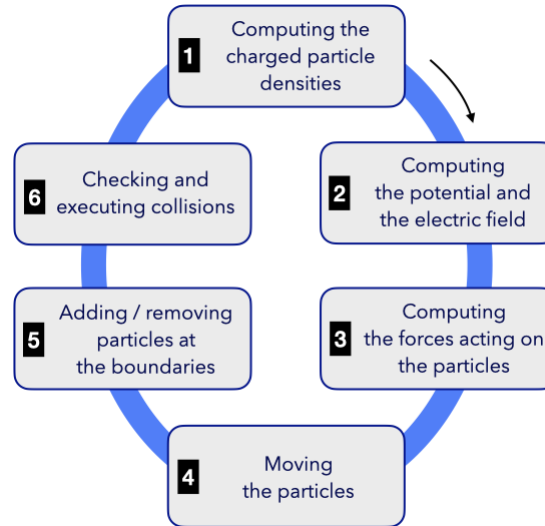
FIGURE 2.2: Chart of a PIC/MCC simulation cycle. Originally published in [76].

1. At the first step of a cycle, the electric charges of the particles (singly charged ions and electrons in the simplest case) are distributed between two neighbouring grid points, resulting in an electric charge density localized in the grid points.

2. At the next step, Poisson's equation is solved on the 1D grid, and the electric field is calculated at the grid points.

3. This is followed by the calculation of the electric field in the positions of the particles, which is achieved by simple interpolation. This way a certain plasma particle interacts with a mean electric field created by all particles (hence the name meanfield approximation). The calculation of forces acting on particles is straightforward.

4. As the forces are known, the particles are moved via the numerical integration of their equations of motion. For the integration, the leapfrog method is used.

5. After the movement, the particles reaching the boundaries, i.e. the electrodes need special care. They are treated according to the surface model implemented (a wide variety of models describing surface processes can be applied

ranging from simple to complex/realistic approaches). In case the interaction of a certain type of particle and the electrode is neglected, the particle is simply removed from the simulation. Otherwise a physical process is modeled, e.g. reflection, secondary electron emission, sputtering etc., potentially resulting in the ejection of new particles from the electrode surface into the discharge space.

6. As the particles move, they can collide with the neutral atoms/molecules of the background gas or with each other. These collisions (gas phase processes) are the key mechanisms in sustaining the plasma. The collision routine is a Monte Carlo method: based on energy-dependent cross sections of several possible elementary collisions, one reaction is chosen by drawing a sample from a random uniform distribution. The reactions are weighted according to their probabilities. In some types of collisions, the new velocities of the colliding particles and the possible new particles (e.g. ion and/or electron) are also generated with a Monte Carlo scheme. A key point is drawing random samples from a Maxwell-Boltzmann distribution corresponding to the temperature of the particle ensemble.

With the help of the PIC/MCC simulation, several global and local physical quantities of CCPs can be calculated. As it was presented in chapter 1, the charged particle densities, the electric field, the electron power absorption rate and the ionization rate can be obtained with spatial and temporal resolution. Practically, any other relevant spatio-temporal distributions can be calculated, e.g. the electrostatic potential, the electron/ion current, the electron/ion energy. From the spatio-temporal distributions, temporal or spatial averages can be obtained. The energy distribution of particles of a given species is often examined based on simulation data, and the heavy particle fluxes and energies at the electrodes are also typical parameters obtained by PIC/MCC simulations. In order to get valuable simulation results, one has to wait until the convergence of the particle numbers is reached in the simulations. This

corresponds to a physically stable discharge, which operates in dynamic equilibrium. From that point, results has to be collected via several RF cycles, in order to get a statistical average with reasonably low error. More details on the implementation of a PIC/MCC code and a demonstration of possible physical quantities calculated by PIC/MCC simulations can be found in [76].

During the past few decades, the PIC/MCC simulation method has been applied for various kinds of CCPs, and simulation codes with various complexity have been developed. Today, gas mixtures with up to $40 - 50$ reactions [77] can be modelled and atmospheric pressure plasmas with very short mean free path and very frequent collisions are studied [36, 37]. Complex surface models have started to be used [71, 78–82], even with structured geometry of the electrodes [83]. Including an external homogeneous magnetic field is also possible [84]. In case of complicated systems, two-dimensional simulations are needed, for which parallelization and the use of GPUs are essential.

2.2 Phase resolved optical emission spectroscopy

Optical spectroscopy is an efficient diagnostic tool for the investigation of gas discharges. It is applicable not only for chemical (compositional) analysis of the plasma, but it can also provide invaluable information on the dynamics of high-energy plasma particles. A time-dependent measurement of the optical emission of a CCP with a temporal resolution which resolves the RF period of the discharge (typically a resolution of few nanoseconds) provides a powerful technique for the observation of the spatio-temporal distribution of the excitation rate of a given atomic state: the phase-resolved optical emission spectroscopy (PROES) [85–87]. In the following, the theoretical basis of this experimental method will be introduced based on the work of Schulze *et al.* [87]. The key statement is that the spatio-temporal excitation rate, $E_{0,k}(x,t)$, i.e. the frequency of electron impact excitation from the ground

state into an observed atomic level k per unit volume, can be calculated from the measured spatio-temporal optical emission. For the population density of this state, n_k, the following rate equation applies:

$$\frac{dn_k(x,t)}{dt} = n_0 E_{0,k}(x,t) + \sum_m n_m E_{m,k}(x,t) + \sum_c W_{ck} n_c(x,t) - \lambda_k n_k(x,t). \quad (2.1)$$

The first term on the right hand side represents excitation from the ground state to level k, with n_0 meaning the population density of the ground state. The term $\sum_m n_m E_{m,k}(x,t)$ considers excitation from metastable levels with population densities n_m, while $\sum_c W_{ck} n_c(x,t)$ represents cascades from higher levels c with population densities n_c to state k with transition probabilities W_{ck}. The last term considers the decay of state k, where λ_k is an effective decay rate:

$$\lambda_k = \sum_j W_{kj} g_{kj} + \sum_q C_q n_q. \quad (2.2)$$

Here two kinds of decays are taken into account: $\sum_j W_{kj} g_{kj}$ represents transitions to other states via photon emission without reabsorption of the photon (W_{kj} being the transition probability and g_{kj} being the probability that the emitted photon is not absorbed), and $\sum_q C_q n_q$ represents quenching, i.e. collisional de-excitation without radiation, where n_q is the density of collision partner of type q, and C_q is the corresponding quenching coefficient (probability per unit time). The rate equation above (2.1) belongs to a system of coupled differential equations together with the rate equations for all metastable and cascade levels containing several unknown quantities, e.g. quenching coefficients, making the $E_{0,k}(x,t)$ excitation rate from the ground state to a certain level k difficult to calculate. However, a proper choice of the excited level to be observed makes several simplifications possible. In an ideal case, the effect of cascades, metastables and quenching can be neglected, and the excitation rate of the given state can be calculated as

$$E_{0,k}(x,t) = \frac{1}{W_{kj} n_0} \left(\frac{dn'_k(x,t)}{dt} + \lambda_k n'_k(x,t) \right), \quad (2.3)$$

with

$$n'_k(x, t) = W_{kj} n_k(x, t), \tag{2.4}$$

where W_{kj} is the transition probability from level k to the final state of the transition of which the optical emission is measured, and $n'_k(x, t)$ represents the emitted number of photons per unit volume and time resulting from that type of transition. In a PROES measurement, these photons emitted via de-excitation of the selected excited state are detected by each pixel of the camera in a time-dependent way. In each time window t_i, the 2D spatial emission is measured, which is then integrated in the spatial direction parallel to the electrodes, resulting in a 1D emission profile proportional to the value of the spatio-temporal emission, $n'_k(x, t_i)$, where the x is measured in the axial direction. Using equation (2.3), a quantity proportional to the $E_{0,k}(x, t)$ spatio-temporal excitation rate can be obtained based on the PROES measurement. In other words, the spatio-temporal distribution of the excitation rate from the ground state to the selected excited state can be calculated from the measured emission data in relative units.

In accordance with the simplifications above, several conditions need to be satisfied in order to perform a valuable PROES measurement on a CCP [87]:

1. Knowledge of the optical transition rates in the gas is needed (see equations (2.2)–(2.4), in which the transition probabilities are variables).

2. The contribution of cascades, excitation from metastable levels and quenching to the population of the measured excited state need to be negligibly low.

3. The intensity of the emitted light at the measured spectral line has to be high enough.

4. No superposition with other optical lines is tolerated within the spectral resolution of the measurement.

5. The lifetime of the observed excited state has to be short enough to temporally resolve the RF period (the shortest period being 74 ns here).

One energy level that reasonably satisfies these criteria in neon gas is Ne 2p$_1$, with a lifetime of 16.26 ns and a relatively high threshold energy for electron impact excitation from the ground state of 18.965 eV [88]. The excitation by metastables and the cascades from higher energy levels to the population of this level is particularly low [89], while quenching is negligible at the low-pressure regime studied here.
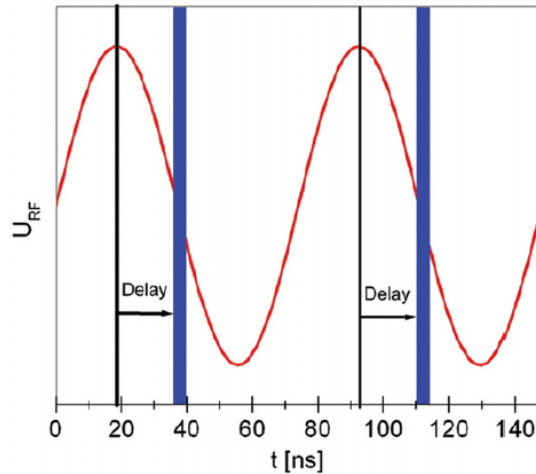
FIGURE 2.3: Sketch of the realization of a PROES measurement [87]. The black lines represent the trigger signals and the blue lanes show the time windows (gate width) under which photons are collected. The driving frequency is 13.56 MHz and the gate width is 4 ns in the current setup.

In figure 2.3 the technical realization of a PROES measurement is demonstrated. The measurements are based on a ICCD (intensified charge-coupled device) camera, which is synchronized with the RF generator via a trigger signal. The whole cycle is divided into time windows corresponding to the gate width of the camera, which is typically set between 1-10 ns (demonstrated by the blue lanes in figure 2.3). Depending on which phase of the RF cycle is scanned during a time slot, the collection of photons starts after a certain triggering time with respect to the beginning of the RF cycle. Each time window of the cycle is scanned several times (typically $10^4 - 10^6$, depending on the emission intensity of the plasma). The time required for one measurement is determined by the repetition rate of the camera, i.e. the number of short scans manageable per unit time, which is approximately 200 kHz, typically requiring a couple of minutes to perform one PROES measurement. In

figure 2.4, a picture of the experimental setup for PROES is shown, which was used for the experimental studies of neon CCPs presented in the 3$^{\text{rd}}$ chapter of the thesis. The orange color glow of the discharge corresponds to the 585 nm Ne transition on which the PROES experiments are conducted.
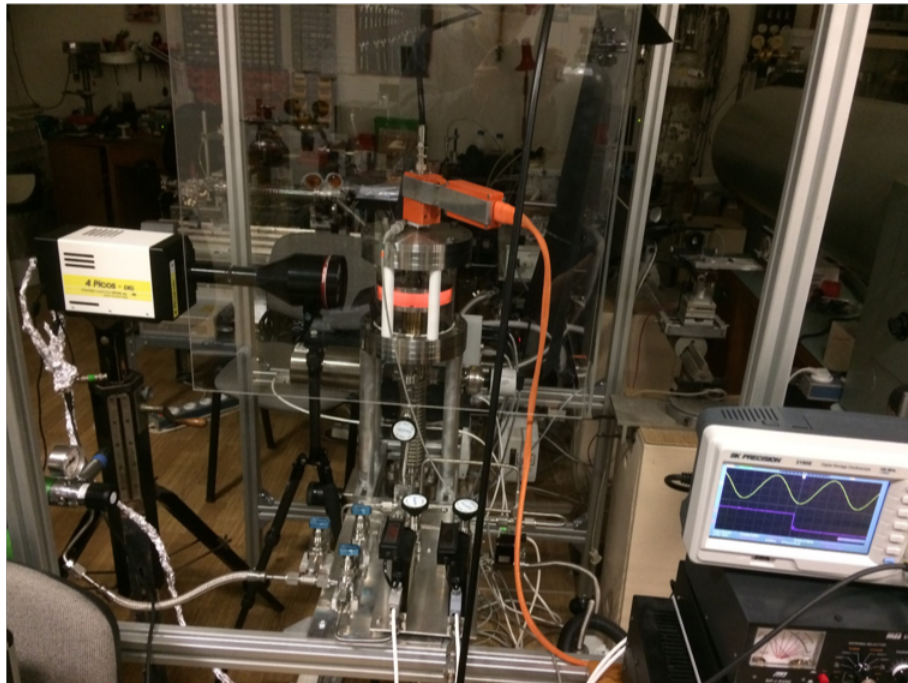
FIGURE 2.4: Photo of the Budapest v.3 plasma reactor and diagnostics, including the camera for PROES measurements (in the laboratory of the Electrical Gas Discharges Research Group in the Wigner Research Centre for Physics).

Chapter 3

Simulation and experimental study of capacitively coupled plasmas

3.1 Background

As it was introduced in chapter 1.2.3, heavy particle induced secondary electron emission is an important surface process in capacitively coupled plasmas (CCPs). However, in particle-in-cell/Monte Carlo collisions (PIC/MCC) simulations, it is often treated in a simple way: only ion-induced secondary electron emisson is taken into account, and usually a constant γ coefficient is used in the simulation, which means that each ion can induce the emission of a secondary electron with a probability equal to γ, irrespectively of its energy and angle of incidence. (Note that the value of γ can be higher than 1 under some conditions: in such cases multiple electrons are emitted in a probabilistic manner.) Earlier computational studies of CCPs have shown that the value of the ion-induced secondary electron emission (SEE) coefficient affected the electron power absorption and ionization dynamics. Increasing the value of the γ-coefficient was found to result in a transition of the discharge operation mode from the α-mode [24–30] to the γ-mode [24, 31–35] (see the introduction to these operation modes in chapter 1.2.4). Varying the γ-coefficient

had an impact on all the calculated discharge characteristics and the control of ion properties at the electrodes as well [33, 34, 71, 90–92]. Due to these effects the importance of the realistic description of the SEE in PIC/MCC simulations of CCPs has already been emphasized [78–80, 82].

While it would be important to use accurate, measured γ coefficients in the simulations, such data are generally not available in the literature for various gases and surfaces. In order to determine unknown γ coefficients and use these in particle-based simulations of CCPs, a computationally assisted spectroscopic technique named γ-CAST[1] has recently been proposed by Daksha *et al.* [93]. This method is based on the fact that the excitation and the ionization rates have different spatio-temporal distributions in CCPs operating in α-mode and γ-mode. Electrons take part in collisions with high threshold energies (excitation and ionization) at locations in space and at times of power absorption maxima, resulting in the α-peak at the bulk side of the expanding sheath edge and the γ-peak within the sheath, near the electrode. As it was introduced in chapter 1.2.4, the α-peak is caused by sheath expansion heating, and the γ-peak is caused by heavy particle induced secondary electrons accelerated efficiently by the electric field within the sheath. In fact, these two mechanisms often come into effect in parallel, resulting in a hybrid $\alpha - \gamma$ mode and the appearance of both peaks. The intensity ratio of these two peaks changes while the transition of the discharge operation mode occurs. Since ion-induced secondary electrons play a central role in the γ-mode, the discharge operation mode and the intensity ratio of the two peaks is sensitive to the value of the γ coefficient [93]. The concept of γ-CAST is the following: the spatio-temporal distribution of the ionization rate is calculated by several runs of PIC/MCC simulations with the same physical parameters but assuming different values for γ. These computed ionization rates are compared to the spatio-temporal distribution of the excitation rate measured by phase-resolved optical emission spectroscropy (PROES). The basis of comparison is the intensity ratio of the two peaks, I_γ/I_α, where I_α and I_γ correspond to the α-peak

---

[1]CAST: Computationally Assisted Spectroscopic Technique

and the γ-peak, respectively. The γ value providing the best agreement between the simulation and the experiment is accepted as the accurate effective SEE coefficient for the system [93]. The term effective refers to the facts that (i) secondary electrons can also be induced by particles other than ions (e.g. metastables, fast atoms, VUV photons) [5] and (ii) secondary electron emission depends on the incident particle energy and the properties of the surface. These effects are all masked by, yet they all contribute to the ion-induced SEE coefficient obtained by γ-CAST. All in all, γ-CAST is a powerful technique to determine the effective SEE coefficient of a system, which can be applied in CCPs operating at the hybrid $\alpha - \gamma$ regime, i.e. under discharge conditions where both the α-peak and the γ-peak are present in the spatio-temporal distribution of the excitation/ionization rates.

The method described above was applied in [93] for argon CCPs operated between stainless steel electrodes at pressures between 75 Pa and 175 Pa and voltage amplitudes between 200 V and 300 V. In order to manage PROES measurements on the Ne $2p_1$ line, 10% neon admixture was added to the argon gas. The discharge dynamics was found to be unaffected by the neon admixture, while it provided a good signal to noise ratio for the PROES measurement. Under these conditions, the accurate γ value was found to be 0.066 [93].

The original γ-CAST method has an inherent deficiency: the calculated ionization rates, based on which the discharge operation modes are defined, are compared to the measured excitation rate. These are different quantities, and the only connection between them is that high-energy electrons cause both processes. In fact, the spatio-temporal distributions of the process rates depend on the energy-distribution of electrons in the discharge, the shapes (i.e. the energy dependence) of the cross sections of all individual processes and their threshold energies. In some cases, these conditions result in practically identical spatio-temporal distributions for the excitation and the ionization rate, however, this is not guaranteed. In this chapter, this issue will be addressed in detail, and an improved version of γ-CAST will be presented.
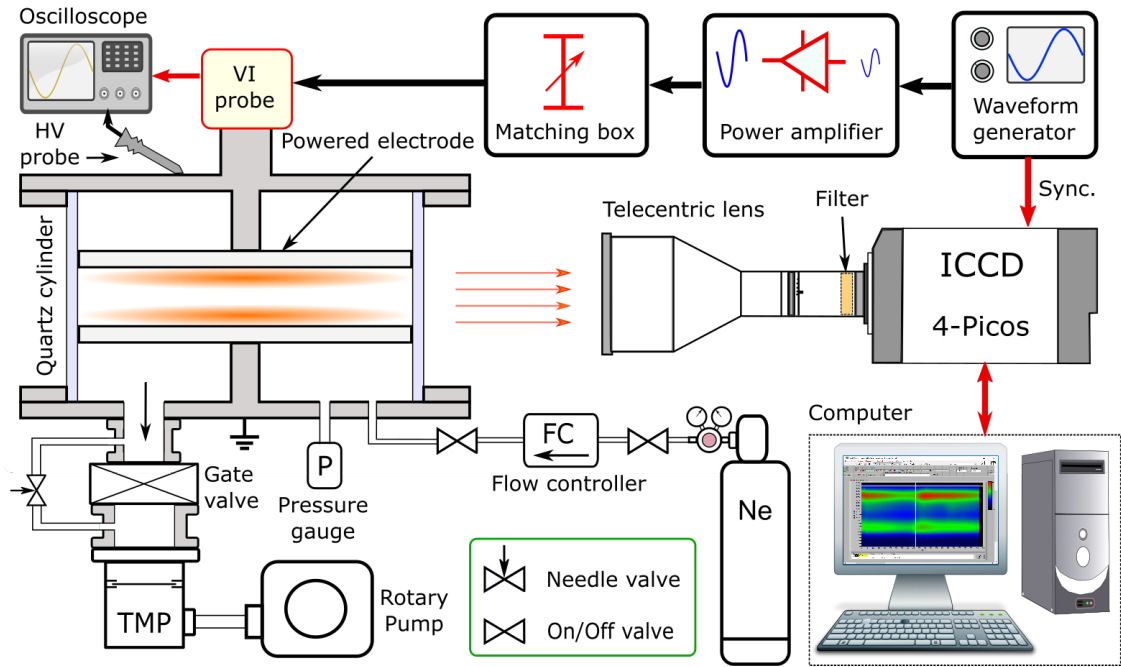
FIGURE 3.1: Sketch of the experimental setup [94].

Although PROES measurement and PIC/MCC simulation are common tools to examine the excitation and ionization dynamics of CCPs, a systematic comparison of their results focusing on the relation of the spatio-temporal distributions of the excitation and the ionization rate has not been performed previously. In the current chapter, such a comparison will be presented for neon CCPs. The dependence of the electron power absorption and the ionization dynamics on the driving frequency and the pressure of the gas is also revealed. Moreover, the applicability of PROES to probe the ionization dynamics is studied in a wide parameter regime.

3.2   Setup and discharge conditions

3.2.1   Experimental setup

The PROES measurements are implemented in the Budapest v.3 cell, a geometrically symmetric CCP source. The scheme of the setup is shown in figure 3.1. The quartz chamber can be evacuated via the gate valve, by a turbomolecular and a rotary pump. The base pressure of the system is approximately 10^{-5} Pa. The experiments are performed in a gas flow of $\sim$3 sccm. A needle valve is installed to enable fine control of the gas pressure in the cell. The electrodes are made of stainless steel, their geometry being plane-parallel and orbicular with identical diameters of 14.2 cm. The gap between them is 2.5 cm. The upper electrode is driven by RF waveform provided by a function generator (Juntek JDS-2900), a linear power amplifier (RM BLA-300) and an impedance matching box (MFJ-949E), i.e. a tunable capacitive/inductive unit which can be adjusted for different driving frequencies, in order to maximize the power delivered to the plasma. The lower electrode is grounded. The voltage between the electrodes is monitored by a high voltage probe (HP 10076A, 100:1), and the pressure can be measured by a capacitive gauge (MKS 631A11MDEH, Type 631).

The actual diagnostic tool of the setup is an ICCD camera (4 Picos, Stanford Computer Optics), by which the emission from the Ne $2p_1$ state at a wavelength of 585.25 nm is measured. The camera is equipped with an interference filter with a central wavelength of 585 nm and a spectral full width at half maximum (FWHM) of 10 nm. The gatewidth of the camera is set between 2 ns to 4 ns, while the length of the RF period is varied between 73.7 ns (13.56 MHz) and 295.0 ns (3.39 MHz). The spatial resolution is approximately 150 μm. The camera has a telecentric lens (Thorlabs MVTC23013 0.128x bi-telecentric lens), which allows taking two-dimensional pictures of the emission intensity. Due to the lateral uniformity of the plasma, the

TABLE 3.1: List of collision processes for neon CCPs.

#	Reaction	Process	References
1	$e^- + Ne \longrightarrow e^- + Ne$	Elastic scattering	[95]
2	$e^- + Ne \longrightarrow e^- + Ne^*$	$1s_5$ excitation	[95]
3	$e^- + Ne \longrightarrow e^- + Ne^*$	$1s_4$ excitation	[95]
4	$e^- + Ne \longrightarrow e^- + Ne^*$	$1s_3$ excitation	[95]
5	$e^- + Ne \longrightarrow e^- + Ne^*$	$1s_2$ excitation	[95]
6	$e^- + Ne \longrightarrow e^- + Ne^*$	$\sum 2p_{10-2}$ excitation	[95]
7	$e^- + Ne \longrightarrow e^- + Ne^*$	$\sum 2s$ excitation	[95]
8	$e^- + Ne \longrightarrow e^- + Ne^*$	3d+3s excitation	[95]
9	$e^- + Ne \longrightarrow e^- + Ne^*$	3p excitation	[95]
10	$e^- + Ne \longrightarrow e^- + Ne^*$	$2p_1$ excitation	[95]
11	$e^- + Ne \longrightarrow 2e^- + Ne^+$	Ionization	[95]
12	$Ne^+ + Ne \longrightarrow Ne^+ + Ne$	Isotropic scattering	[96]
13	$Ne^+ + Ne \longrightarrow Ne^+ + Ne$	Backscattering	[96]

data are averaged in the direction perpendicular to the discharge axis, which reduces the noise significantly.

3.2.2   Simulation setup

In the PIC/MCC simulations of RF discharges in neon, Ne^+ ions and electrons are traced. The cross sections of the collision processes are listed in table 3.1 and shown in figure 3.2. The electron-atom processes considered are elastic scattering, excitation and ionization, and their cross sections are taken from the Biagi-v7.1 dataset [95]. Among the nine atomic excitation processes taken into account (represented by the solid lines in figure 3.2) one is the Ne $2p_1$ excitation from the ground state (see the thick continuous line), the process of which the population dynamics is measured by PROES. As for Ne^+ ions, isotropic and backward elastic scattering is considered for their interaction with Ne atoms [96].

The surface processes implemented in the current simulations are electron reflection and secondary electron emission induced by ions. Both are treated in a simplified way, namely by constant surface coefficients. In case of electrons a constant $\eta_e = 0.2$ is assumed for elastic reflection [97]. The interaction of Ne^+ ions with the electrodes
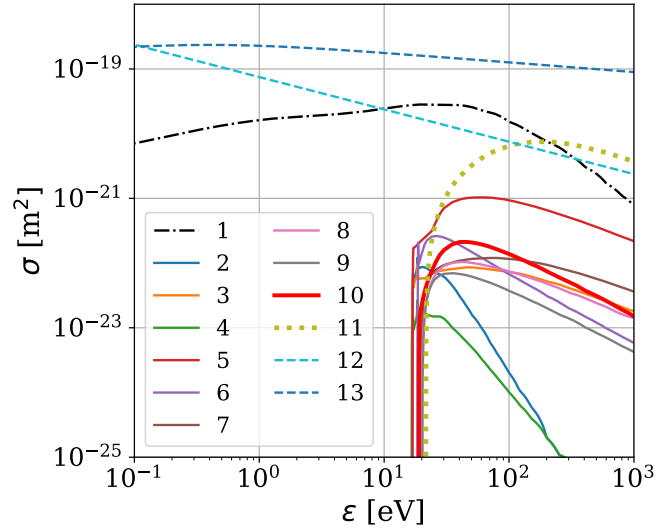
FIGURE 3.2: The cross section set used in the PIC/MCC simulations of neon CCPs, listed in table 3.1 (processes 1–13). ε is the kinetic energy of the projectile, which is measured in the center-of-mass frame in case of ions. The thick solid red line represents the Ne $2p_1$ electron-impact excitation from the ground state, which is often measured by PROES (process 10), and the thick dotted green line corresponds to electron-impact ionization (process 11). [94].

is considered by constant γ coefficient. The choice of the accurate γ is in focus of the current chapter.

3.2.3   Discharge conditions

The neon discharges were driven by a single-frequency harmonic waveform, the value of the frequency ranging from 3.39 MHz to 13.56 MHz, and the pressure was set between 60 Pa and 500 Pa. The voltage amplitude was kept constant at 165 V.

3.3   Measurement of the ion induced secondary electron emission coefficient with a computationally assisted spectroscopic technique

In figure 3.3, PIC/MCC simulation results on the Ne $2p_1$ excitation rate and the ionization rate obtained for three different values of the γ coefficient are presented ($\gamma = 0.2$, 0.29, 0.35, row by row) and compared to PROES measurement on the Ne $2p_1$ excitation rate (panel (d)) for a driving frequency of 6.78 MHz, a voltage amplitude of 165 V and a pressure of 500 Pa. This way the effect of varying the γ-coefficient on the excitation and the ionization rates is demonstrated. The excitation rate is shown in the left column. For the lowest γ of 0.2, the most intense excitation can be observed near the sheath edges (figure 3.3(a)), i.e. a strong α-peak appears. For a higher SEE coefficient of 0.29, a notable excitation pattern appears within the sheaths, while the spatio-temporal distribution of the excitation rate is still dominated by patterns at the sheath edges (figure 3.3(b)). The average intensity of the α-peak is higher than the one of the γ-peak under these conditions. In case of $\gamma = 0.35$, the excitation is dominated by the γ-peak within the sheath, and it is negligible at the expanding sheath edges (figure 3.3(c)). According to the PROES measurement (figure 3.3(d)), the excitation rate is high both at the sheath edges and within the sheaths, the α-peak being stronger. Regarding the ionization rate, a transition of the discharge operation mode can be observed by increasing the value of the SEE coefficient (see the right column, panels 3.3(e-g)): at $\gamma = 0.2$, the spatio-temporal distribution of the ionization rate exhibits a hybrid α-γ-mode (figure 3.3(e)), while a pure γ-mode is found for the largest value of $\gamma = 0.35$ (figure 3.3(g)). These results show that the value of γ is absolutely critical in terms of the discharge operation mode. It is also important that the spatio-temporal distributions of the ionization and the excitation rates significantly differ for all values of γ under these conditions.
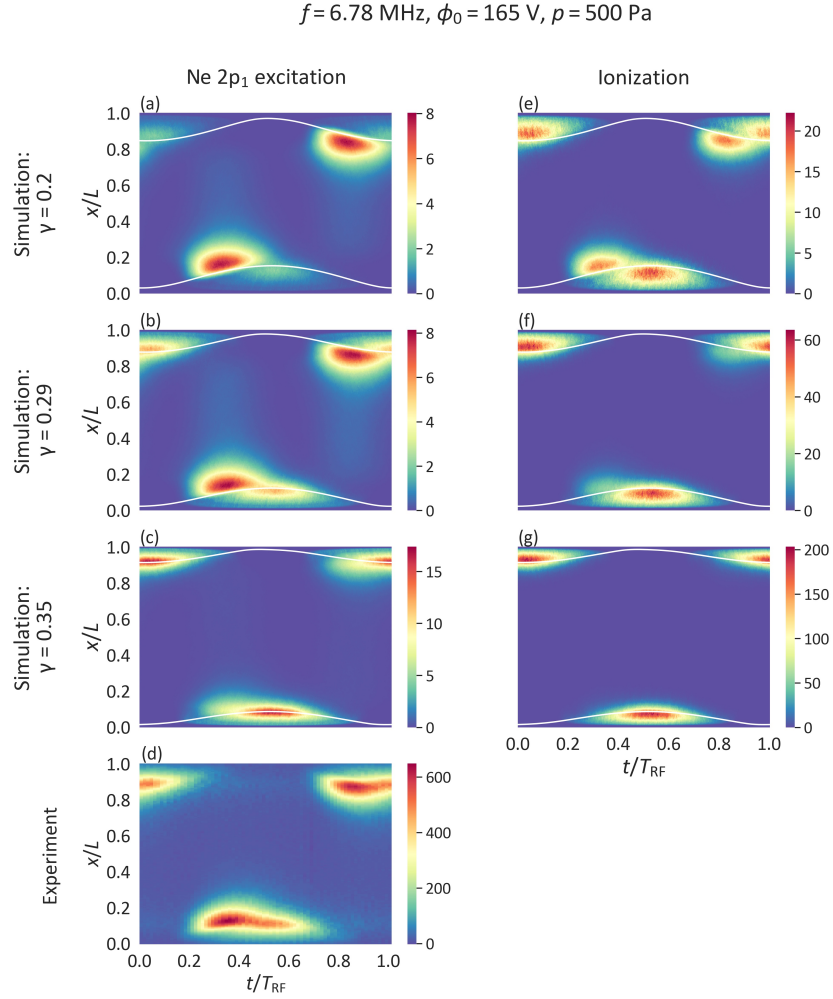
FIGURE 3.3: Spatio-temporal plots of the electron-impact excitation rate from the ground state into the Ne $2p_1$ state obtained from PIC/MCC simulations $[10^{20} \text{ m}^{-3}\text{s}^{-1}]$ (a-c) and measured by PROES [a.u.] (d), and the ionization rate obtained from PIC/MCC simulations $[10^{21} \text{ m}^{-3}\text{s}^{-1}]$ (e-g). In the simulations, different coefficients for the ion-induced SEE are considered: $\gamma = 0.2$ (1st row), 0.29 (2nd row) and 0.35 (3rd row). The sheath edges obtained from the simulations are shown as white lines. The powered electrode is located at $x/L = 0$, while the grounded electrode is at $x/L = 1$. Discharge conditions: $f = 6.78$ MHz, $L = 2.5$ cm, $\phi_0 = 165$ V, $p = 500$ Pa. $T_{RF} = 1/f$ [94].

Since both the α- and γ-peak appear under these conditions and their intensity changes as a function of γ, the γ-CAST method is applicable for the determination of the accurate SEE coefficient for this system. Given that the excitation and the ionization rate exhibited different spatio-temporal distributions, I applied the γ-CAST method in a different way compared to the original method published in

[93]: instead of comparing the ionization rates calculated by PIC/MCC simulations with various values of γ, I compared the computed Ne $2p_1$ excitation rates to the corresponding excitation rate measured by PROES. These are exactly the same quantities obtained by simulation and experiment. The γ-CAST was carried out for a pressure of 500 Pa, driving voltage amplitude of 165 V, and frequencies of 3.39 MHz and 6.78 MHz, assuming various values for the γ-coefficient between 0.2 and 0.35 (results for some selected values of γ are shown in figure 3.3 for 6.78 MHz).
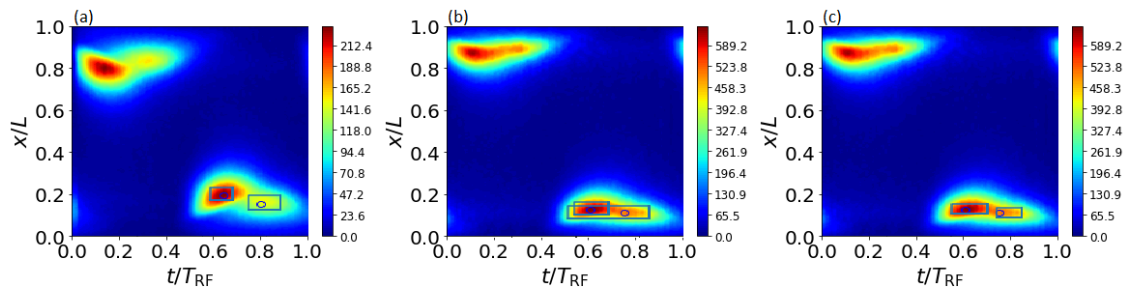
FIGURE 3.4: Defining the ROIs in the γ-CAST. The circles represent the local intensity maxima and the rectangles correspond to the ROIs around them. The spatio-temporal distributions of the Ne $2p_1$ excitation rate are obtained from PROES measurements. Discharge conditions: $L = 2.5$ cm, $\phi_0 = 165$ V, $p = 500$ Pa. At $f = 3.39$ MHz, (a) the boundaries of the region are clear. At $f = 6.78$ MHz, (b) the left boundary of the γ-peak is uncertain, since the ROI of the γ-peak according to the definition contains the α-peak. This problem is solved by (c) an arbitrary definition of the left boundary of the γ-peak.

The key point of γ-CAST is the determination of the average intensities of the α-peak, I_α and the γ-peak, I_γ on the spatio-temporal Ne $2p_1$ excitation plots obtained from PROES measurement and PIC/MCC simulations. For a certain intensity peak, the intensity is averaged over a region of interest (ROI) defined as a rectangle in which the intensity is higher than 80% of the local maxima [93]. More precisely, the boundaries of the rectangle are fit to the points where the intensity decreases below 80% of the local maxima on the horizontal/vertical line transversing the point of the local maxima. This is illustrated in figure 3.4. In panel (a), the ROIs for both the α-peak and the γ-peak are clear according to the definition. However, the definition has to be treated carefully. For example, in panel (b) the left boundary of the γ-peak is uncertain, since the ROI defined according to the definition contains the α-peak.

The intensity left from the γ-peak does not decrease below 80% of the local maxima before reaching the stronger α-peak. The two peaks overlap. This issue is solved by defining an arbitrary boundary for the ROI of the γ-peak at the left side (see panel (c)). The uncertainty of γ resulting from this remains below 0.005.
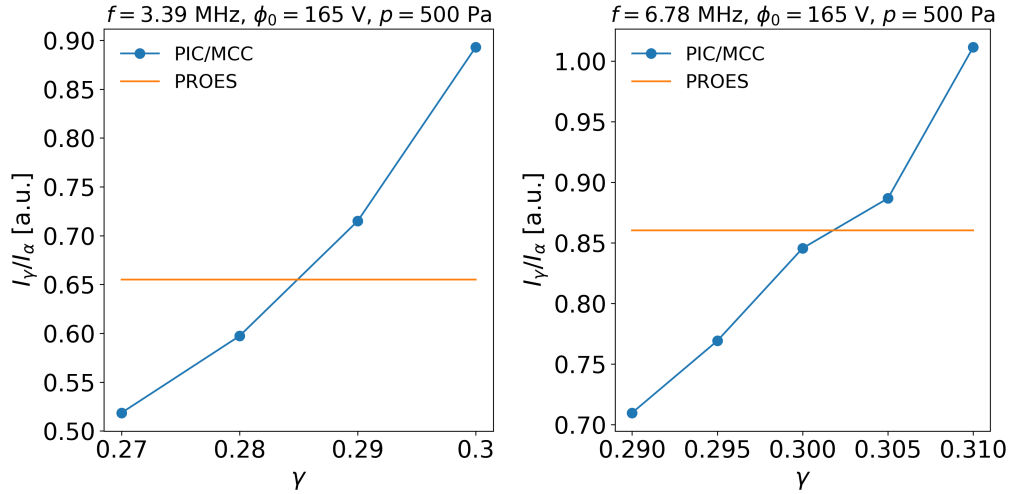
FIGURE 3.5: Evaluation of the γ-CAST results for (a) $f = 3.39$ MHz and (b) $f = 6.78$ MHz driving frequencies. The I_γ/I_α intensity ratios are shown for the PIC/MCC simulation as a function of γ, while the intensity ratios obtained from PROES are shown as a constant lines. Discharge conditions: $L = 2.5$ cm, $\phi_0 = 165$ V, $p = 500$ Pa.

After defining the ROIs for both peaks, the I_γ/I_α ratios are compared for the PROES measurement and the PIC/MCC simulations with various γ. This is shown in figure 3.5. Under the conditions of 3.39 MHz, 500 Pa and 165 V, the best agreement was found for $0.280 < \gamma < 0.290$, while for a higher frequency of 6.78 MHz, the best agreement was obtained for $0.295 < \gamma < 0.300$ (see figure 3.5).

Based on the results of γ-CAST, $\gamma = 0.29$ was chosen to be used in the simulations for other discharge conditions as well (presented in the next section, 3.4). However, the actual value of the γ coefficient depends on all the discharge conditions (e.g. driving voltage shape and amplitude, driving frequency, gas pressure, electrode gap distance), given that secondary electron emission induced by ions (and SEE by other species that are all included in the effective γ coefficient) depends on the incident particle energy [5]. The energy distributions of particles arriving at the electrode

surfaces are affected by all these discharge conditions. Still, the choice of $\gamma = 0.29$ for other discharge conditions remains accurate, as the difference between the γ values obtained for different driving frequencies is minor (between 3% and 4% for 3.39 MHz and 6.78 MHz, see figure 3.5), and secondary electrons (SEs) have less impact on the discharge operation mode at lower values of the gas pressure, when the γ-electrons emitted from the electrode are not multiplied that efficiently due to their energy gain in the electric field within the sheaths.

3.4   Limitations of phase resolved optical emission spectroscopy in detecting the ionization dynamics

In the following, the excitation and the ionization dynamics is examined while the pressure is varied at different driving frequencies, and the applicability of PROES to probe the ionization dynamics is studied. In figures 3.6-3.7, a comparison of the PROES and PIC/MCC simulation results for the spatio-temporal distribution of the Ne $2p_1$ excitation rate is presented. The ionization rates obtained from the simulations for the same conditions are also included in the figures (third columns).

Figure 3.6 contains results for 13.56 MHz. The driving voltage amplitude is fixed at 165 V, while the pressure is varied from 60 Pa to 500 Pa. The rows of the figure from top to bottom correspond to different values of the gas pressure in increasing order. The columns from left to right correspond to the measured and computed excitation rate and the computed ionization rate, respectively. Under these conditions, fairly good agreement is obtained between the PROES measurements (first column) and PIC/MCC simulations (second column) for the spatio-temporal distributions of the Ne $2p_1$ excitation rate, for the whole range of the pressure. The sheath widths obtained by PIC/MCC simulations also agree to the ones observed

FIGURE 3.6: Spatio-temporal plots of the electron-impact excitation rate from the ground state into the Ne $2p_1$ state measured by PROES [a.u.] (a-d) and obtained from PIC/MCC simulations [10^{20} m^{-3}s^{-1}] (e-h), and the ionization rate obtained from PIC/MCC simulations [10^{21} m^{-3}s^{-1}] (i-l) at various neutral gas pressures. The sheath edges obtained from the simulations are shown as white lines in panels (e-l). The powered electrode is located at $x/L = 0$, while the grounded electrode is at $x/L = 1$. Discharge conditions: $f = 13.56$ MHz, $L = 2.5$ cm, $\phi_0 = 165$ V, the pressure is varied between 60 Pa and 500 Pa. $T_{\text{RF}} = 1/f$. $\gamma = 0.29$ is used in the simulations [94].

experimentally (in case of the PROES measurements, the sheath lengths are only visually estimated based on the excitation plot). On the other hand, the ionization rates have different spatio-temporal distributions than the excitation rates (see the third column compared to the first two): the excitation is localized at the expanding sheath edge within the whole pressure range, which suggests α-mode discharge

operation. However, ionization can also be observed within the sheaths at higher pressures, at the phase when they are expanded. At the lowest pressure of 60 Pa, the ionization rate exhibits dominant α-mode, which changes to pure γ-mode as the pressure is increased to 500 Pa (see figures 3.6(i-l)). This transition is completely unobservable by PROES measurement, with which the spatio-temporal distribution of the Ne $2p_1$ excitation rate can be obtained. When the pressure is higher, the excitation rate does not probe the ionization dynamics. This means that PROES cannot tell us how the discharge actually works under these conditions.

At the low frequency of 3.39 MHz, the pressure is varied between 120 Pa and 500 Pa. The corresponding spatio-temporal plots are shown in figure 3.7, which has the same layout as the previous one (figure 3.6). The Ne $2p_1$ excitation rates are again in a good agreement between the PROES measurements (first column) and the PIC/MCC simulations (second column). For all values of the pressure the excitation within the sheaths is slightly stronger according to the simulations compared to the PROES results. A possible reason is that γ may depend on the driving frequency due to e.g. frequency dependent changes of heavy particle energies at the electrodes, and the γ value of 0.29 can be a slight overestimation of SEE at all values of the pressure for the present conditions. Both the simulations and the experiments exhibit strong α-peaks in the excitation plots at the expanding sheath edges, and γ-peaks also appear within the sheaths at the times of maximal sheath expansion. These γ-peaks get more intense as the pressure is increased from 120 Pa to 500 Pa. At high pressures, the measured and the calculated excitation rates (see figure 3.7(c, g, d, h)) suggest discharge operation in the hybrid α-γ-mode, the α-peak being stronger. The ionization rates for 3.39 MHz are shown in the third column of figure 3.7. The PIC/MCC simulation shows dominant γ-mode for all pressures. There are also minor ionization patterns at the edges of the sheaths, which weaken as the pressure increases (3.7(i-l)). At this low frequency, PROES is clearly unable to show the ionization dynamics properly: the Ne $2p_1$ excitation (obtained by PROES measurement and PIC/MCC simulation as well) and the ionization ("observable"
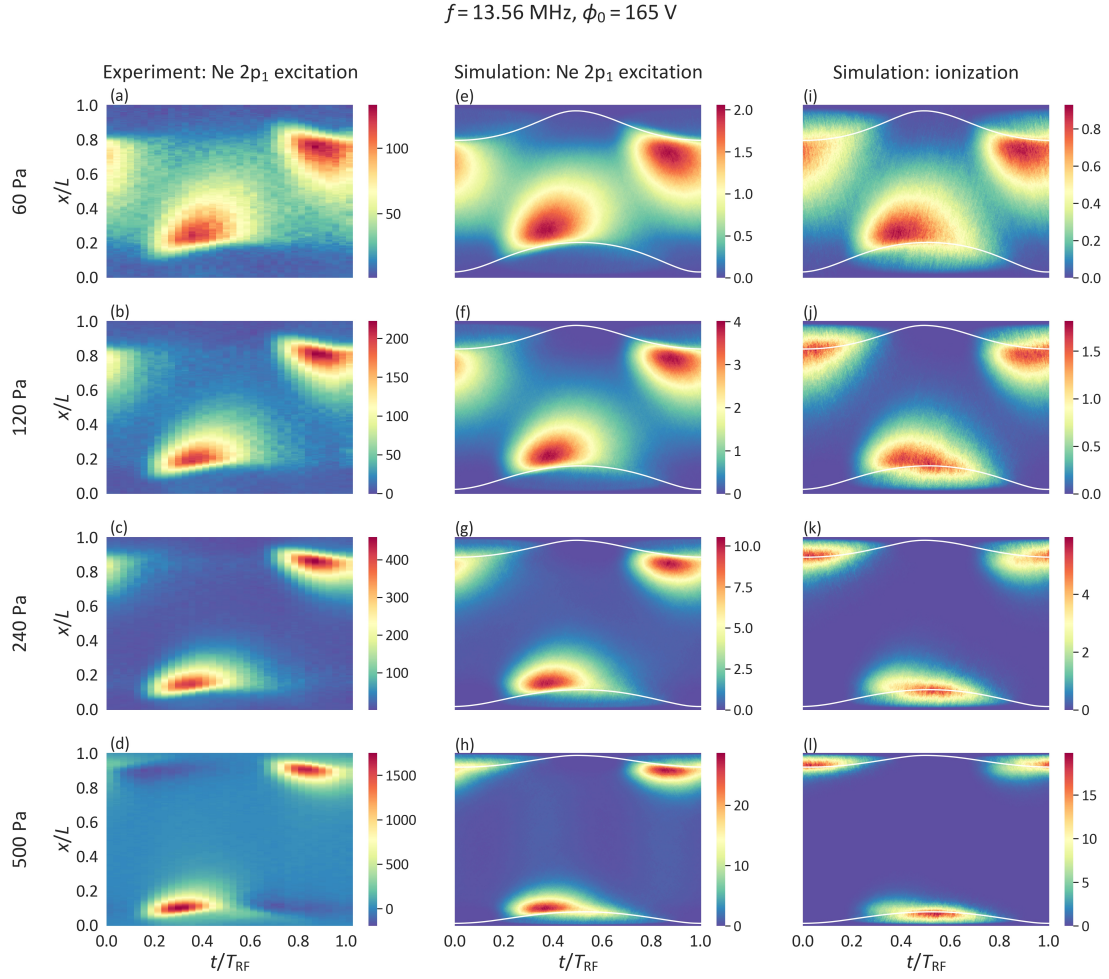
f = 3.39 MHz, ϕ_0 = 165 V
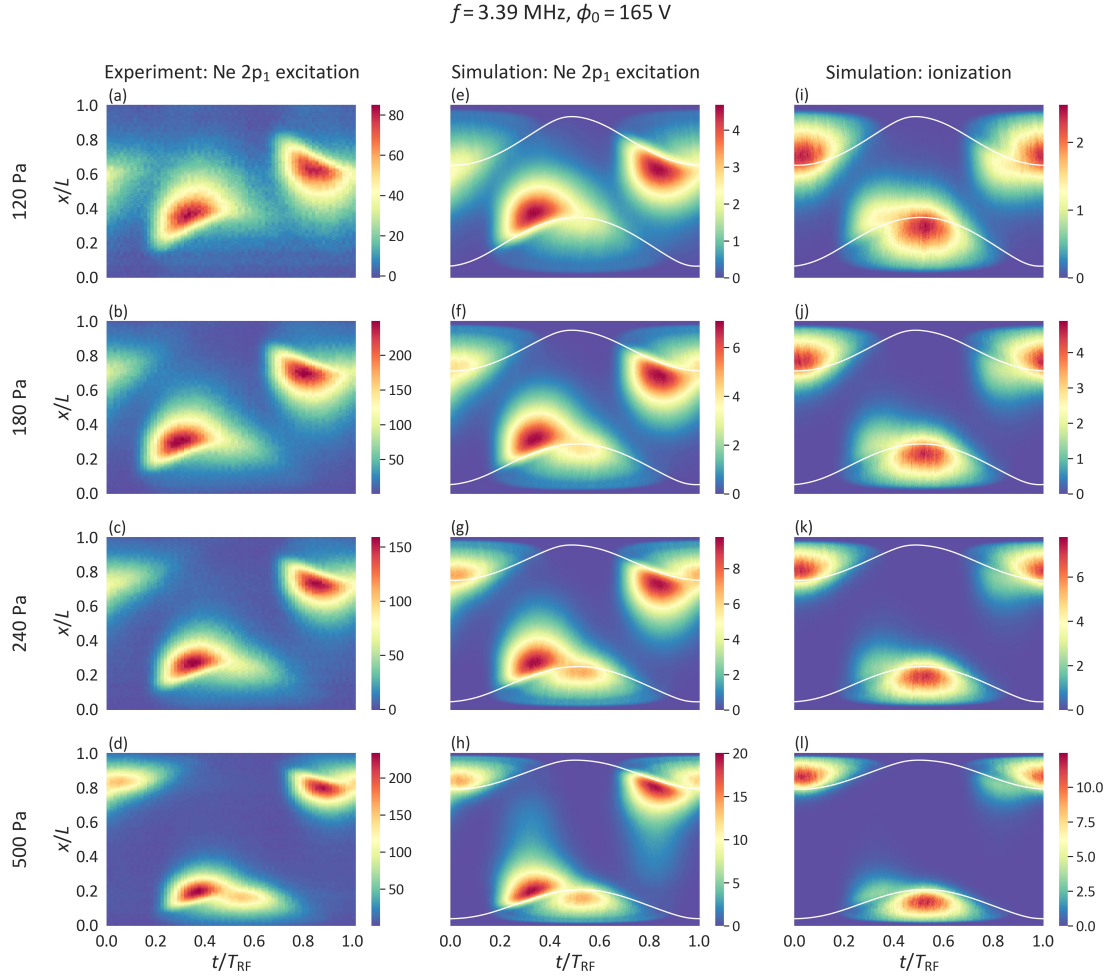
FIGURE 3.7: Spatio-temporal plots of the electron-impact excitation rate from the ground state into the Ne $2p_1$ state measured by PROES [a.u.] (a-d) and obtained from PIC/MCC simulations [10^{19} m^{-3}s^{-1}] (e-h), and the ionization rate obtained from PIC/MCC simulations [10^{20} m^{-3}s^{-1}] (i-l) at various neutral gas pressures. The sheath edges obtained from the simulations are shown as white lines in panels (e-l). The powered electrode is located at $x/L = 0$, while the grounded electrode is at $x/L = 1$. Discharge conditions: $f = 3.39$ MHz, $L = 2.5$ cm, $\phi_0 = 165$ V, the pressure varied between 120 Pa and 500 Pa. $T_{RF} = 1/f$. $\gamma = 0.29$ is used in the simulations [94].

by PIC/MCC simulation) have completely different spatio-temporal distributions.

To understand why this happens, the energy-resolved ionization and Ne $2p_1$ excitation rates are examined. These are the numbers of ionization and excitation events caused by electrons with a certain energy in the expanded sheath. Figure 3.8 shows these rates for 500 Pa. I counted the events in a "rectangular" area between
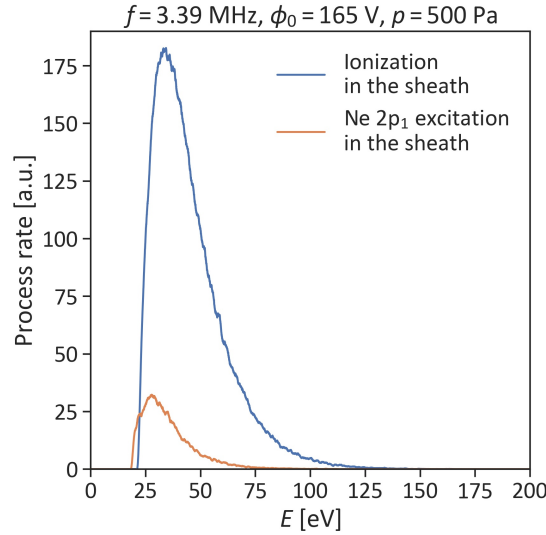
FIGURE 3.8: PIC/MCC simulation result: the energy-resolved ionization and Ne 2p$_1$ excitation rates caused by the electrons within a region inside the sheaths (see text). Discharge conditions: $f = 3.39$ MHz, $\phi_0 = 165$ V, $p = 500$ Pa, $L = 2.5$ cm, $\gamma = 0.29$ [94].

$0.4 < t/T_{\mathrm{RF}} < 0.6$ and $0 < x/L < s_{\mathrm{max}}$, where s_{max} is the sheath width at the powered electrode. We can see that the electrons which cause ionization have a wider range of energies. The number of excitations becomes negligible above ~ 50 eV, but the number of ionizations stays high until ~ 100 eV in this case. The reason behind this is the relation of the cross sections of the two processes as a function of the electron energy (see the thick solid and dotted lines in figure 3.2). Although their thresholds are close to each other (19 eV for the excitation and 22 eV for the ionization), they have different shapes within the energy range up to hundreds of eV, i.e. the energy regime of electrons in the discharge. Although the cross section of excitation decreases above ~ 40 eV, the one of ionization continuously increases up to ~ 300 eV. This relation of the two cross sections causes the ionization dynamics to be more sensitive to high-energy electrons, which means that significantly more ionization processes are caused by energetic γ-electrons accelerated within the expanded sheaths than Ne 2p$_1$ excitation.

3.5   Summary

In this chapter, I reported the determination of the effective ion-induced SEE co-efficient (γ) for neon CCPs operated between electrodes made of stainless steel. In order to achieve that, I applied a revised version of the γ-CAST method, a computationally assisted spectroscopic technique, which is a quantitative implementation of searching for the best match between the Ne $2p_1$ spatio-temporal excitation rate obtained by PROES and the corresponding excitation rates obtained by PIC/MCC simulations executed with various values of the SEE coefficient, γ. The value of the γ coefficient was found to have a fundamental impact on the excitation and ionization rates obtained by PIC/MCC simulations. With the help of γ-CAST, the accurate effective γ value for the current system was found to be 0.29.

By PIC/MCC simulations using the γ value determined by γ-CAST, I reproduced the spatio-temporal distributions of the Ne $2p_1$ excitation rate obtained by PROES, for a wide parameter regime. The pressure was varied between 60 Pa and 500 Pa, frequencies between 3.39 MHz and 13.56 MHz were studied while the driving voltage amplitude was kept constant at 165 V. The computational and the experimental results had a persuasive agreement, which is a strong verification for the PIC/MCC simulation and the method of the determination of the γ-coefficient. Both experiments and simulations confirmed a partial transition of the discharge operation mode from the α-mode towards the γ-mode by increasing the pressure at a fixed frequency and voltage amplitude. However, while the excitation rates were dominated by the α-peak under all conditions, the ionization rates showed different spatio-temporal distributions. By increasing the pressure, a complete discharge operation mode transition from the α-mode to the pure γ-mode was observed based on the ionization rates calculated by PIC/MCC simulations. Under the current conditions, PROES did not probe the ionization dynamics accurately. In fact, PROES is limited to the observation of the dynamics of the electron-impact excitation from the ground state

into the chosen excited state. The key statement of this chapter is that this excitation dynamics can significantly differ from the ionization dynamics. Because of this, one should generally be careful with predicting the operation mode of the discharge based on PROES data. The reason behind the difference of the spatio-temporal distributions of the Ne $2p_1$ excitation rate and the ionization rate was identified: energetic γ-electrons in neon caused ionization more likely than excitation because of the difference in the shape of the respective cross sections as a function of the electron energy. Although the threshold for the two processes are relatively close (19 eV for the excitation and 22 eV for the ionization), the cross section of Ne $2p_1$ excitation decreases above ~ 40 eV, while the cross section of ionization continuously increases up to ~ 300 eV.

Chapter 4

Secondary electron emission in electronegative plasmas

4.1 Background

As it was demonstrated in the previous chapter (chapter 3), the value of the γ coefficient is critical regarding the particle-in-cell/Monte Carlo collisions (PIC/MCC) simulation results. Recently, secondary electron emission (SEE) induced by heavy particles (ions and fast neutrals) have been studied in PIC/MCC simulations, by realistic models respective of the particle impact energy and the electrode material [71, 78–80, 98–103].

The description of the electron-surface interactions in such simulations, though, have gained attention during the last decade only. Originally, several simplifications have been applied for the interaction of electrons with the electrode surface. Even perfect absorber surfaces have been assumed, and the assumption of a constant elastic reflection coefficient for the electrons was also widespread. Such a constant coefficient is irrespective of the discharge conditions (which determine the energy distribution

of electrons in a certain discharge) and the properties of the electrode surface. Furthermore, other electron-surface processes are neglected, like electron-induced SEE. During the last years, the realistic implementation of the electron-surface interaction has become more common. In PIC/MCC simulations of Gopinath *et. al.* [17], a realistic electron-induced SEE model was implemented. In this model, the SEE coefficient for electrons was assumed to depend on the energy and the angle of incidence of the incoming electron. In a previous work, I studied the electron-electrode interaction in capacitively coupled plasmas (CCPs) operated in argon at a low pressure of 0.5 Pa by PIC/MCC simulations [81]. The electrode material was SiO_2. The electron-electrode interaction was described by a realistic model considering elastic and inelastic reflection of the electrons and the emission of secondary electrons (true secondary electrons (SEs), also called δ-electrons) upon electron impact. For all these processes surface coefficients depending on the energy and the angle of incidence of the electrons, being specific for the surface properties, were defined. In this earlier study [81] I found that the electron induced SEE played a special role in the electron dynamics and shaping the plasma characteristics at low pressures and high voltage amplitudes. Under the studied conditions (0.5 Pa, 6.7 cm electrode gap, 13.56 MHz driving frequency, voltage amplitude around 1000 V), two energetic electron beams within a single RF period were observed at each electrode to propagate towards the bulk, during the sheath expansion and the collapse phase as well. In parallel, the plasma density was significantly higher and the ionization dynamics was different compared to simulation results based on a simple model for the interaction of electrons with the surface. This realistic model for the electron-surface interaction has recently been used in a number of PIC/MCC simulation studies of argon CCPs with SiO_2 [41, 51, 103–107], Si [51, 106] and Cu [103] electrodes.

Electronegative oxygen CCPs have been extensively studied by the PIC/MCC method. These simulations often use simplified models for the surface processes [22, 108–114]. Realistic models for SEE due to heavy particles are rarely applied, except for some

studies [79, 82, 100, 101, 115]. However, the surface coefficients applied in simulations of CCPs can have a significant influence on the discharge properties under certain conditions. For instance, Proto *et al.* [116] investigated the effect of changing the surface quenching coefficient of $O_2(a^1\Delta_g)$ metastable molecules on the discharge operation mode: at 25 mTorr, a hybrid DA/α mode was obtained for a high quenching coefficient of 0.1, while a pure α-mode was achieved when the coefficient was less than 0.001. Derzsi *et al.* [110] compared the spatio-temporal distribution of the dissociative excitation rate from PIC/MCC simulations and experiments using phase-resolved optical emission spectroscopy. They reported that the measured patterns were well reproduced by the simulations for a surface quenching coefficient of 6×10^{-3}. They also examined the effects of using different values of this coefficient between 6×10^{-4} and 6×10^{-2} in the simulations at 200 mTorr for different harmonics. They observed that lower values increased the α-mode electron power absorption, while higher values increased the DA-mode electron power absorption [110]. Wang *et al.* [40] reported that increasing the γ coefficient in the simulations caused the striations to vanish and the γ-mode to emerge in oxygen CCPs. Hannesdottir *et al.* [79] and Proto *et al.* [101] detected that including realistic heavy particle induced SEE in the PIC/MCC simulation model led to higher plasma density, lower electronegativity and a high-energy tail in the electron energy probability function.

This chapter examines the effects of electron induced SEs on the characteristics of single-frequency oxygen CCPs at low pressures (below 1 Pa). This pressure regime is relevant for applications, e.g. for the etching of graphene [117] and polycyclohexene carbonate [118], as well as highly oriented pyrolytic graphite [119] and polydimethyl siloxane films [120], for resist stripping and multilayer lithography [121]. In order to optimize these applications, fundamental understanding of the plasma processes is needed. In the current chapter, I apply the method previously used for single-frequency electropositive argon CCPs to clarify the role of electron-induced SEs in such discharges [81]. I focus on similar discharge conditions to that study. Two

different approaches are used to model the interaction of electrons with the electrode material. The first approach is a simple, conventional one that considers only elastic reflection of electrons at the boundary surfaces with a constant probability. The second approach is more realistic and complex [9, 81], taking into account elastic and inelastic reflection of electrons as well as electron-induced SEE (emission of δ-electrons). The surface coefficients in this approach are functions of the energy and angle of incidence of the electrons and depend on the surface properties. I also consider simple/realistic approaches for describing the SEE induced by ions (emission of γ-electrons) at the electrodes. In the simple approach, a constant SEE coefficient for the O_2^+ ions is applied. In the more realistic approach, though, the SE yield due to O_2^+ ions depends on the energy of the ions [79]. I consider three different combinations of simple and realistic approaches to describe the interaction of ions and electrons with the electrodes in discharge models. The simulation results obtained based on the different models are compared in order to understand the effects of SEE on the characteristics of oxygen CCPs, including charged particle and metastable densities, electronegativity, electron power absorption and ionization dynamics.

4.2   Simulation model and discharge conditions

The current chapter focuses on a computational study of oxygen CCPs. For that purpose, I use the PIC/MCC method adapted to oxygen plasmas. The original version of the discharge model for oxygen CCPs has been introduced in [22]. The simulation code has been validated multiple times by experiments under various conditions [22, 110, 122, 123]. In the frame of this work, I implemented the realistic treatment of the interactions of electrons and ions with the electrode surface as additional functionalities to the simulation code.

TABLE 4.1: List of collision processes for oxygen CCPs.

#	Reaction	Process	References
1	$e^- + O_2 \longrightarrow O_2 + e^-$	Elastic scattering	[124]
2	$e^- + O_2(r=0) \longrightarrow e^- + O_2(r>0)$	Rotational excitation	[125]
3	$e^- + O_2(v=0) \longrightarrow e^- + O_2(v=1)$	Vibrational excitation	[125]
4	$e^- + O_2(v=0) \longrightarrow e^- + O_2(v=2)$	Vibrational excitation	[125]
5	$e^- + O_2(v=0) \longrightarrow e^- + O_2(v=3)$	Vibrational excitation	[125]
6	$e^- + O_2(v=0) \longrightarrow e^- + O_2(v=4)$	Vibrational excitation	[125]
7	$e^- + O_2 \longrightarrow e^- + O_2(a^1\Delta_g)$	Metastable excitation (0.98 eV)	[125]
8	$e^- + O_2 \longrightarrow e^- + O_2(b^1\Sigma_g)$	Metastable excitation (1.63 eV)	[125]
9	$e^- + O_2 \longrightarrow O + O^-$	Dissociative attachment	[125]
10	$e^- + O_2 \longrightarrow e^- + O_2^*$	Excitation (4.5 eV)	[125]
11	$e^- + O_2 \longrightarrow O(^3P) + O(^3P) + e^-$	Dissociation (6.0 eV)	[125]
12	$e^- + O_2 \longrightarrow O(^3P) + O(^1D) + e^-$	Dissociation (8.4 eV)	[125]
13	$e^- + O_2 \longrightarrow O(^1D) + O(^1D) + e^-$	Dissociation (9.97 eV)	[125]
14	$e^- + O_2 \longrightarrow O_2^+ + e^- + e^-$	Ionization	[126]
15	$e^- + O_2 \longrightarrow e^- + O + O(3p\ ^3P)$	Dissociative excitation (14.7 eV)	[125]
16	$e^- + O^- \longrightarrow e^- + e^- + O$	Electron impact detachment	[126]
17	$e^- + O_2^+ \longrightarrow O(^3P) + O(^1D)$	Dissociative recombination	[126]
18	$O_2^+ + O_2 \longrightarrow O_2 + O_2^+$	Elastic scattering: charge exchange	[126]
19	$O_2^+ + O_2 \longrightarrow O_2 + O_2^+$	Elastic scattering: isotropic part	[126]
20	$O^- + O_2 \longrightarrow O^- + O_2$	Elastic scattering	[126]
21	$O^- + O_2 \longrightarrow O + O_2 + e^-$	Detachment	[126]
22	$O^- + O_2^+ \longrightarrow O + O_2$	Mutual neutralization	[126]
23	$O^- + O_2(a^1\Delta_g) \longrightarrow O_3 + e^-$	Associative detachment	[108]

4.2.1 Gas phase processes

The particle species traced in the simulations are electrons, O_2^+ and O^- ions. 23 elementary collision processes are considered in the discharge model, see the list of processes in table 4.1 and plots of the cross sections in figure 4.1. The cross sections are taken from [108, 124–126]. Between electrons and O_2 molecules, the processes considered are elastic scattering, rotational, vibrational and electronic excitation, ionization, dissociative excitation and dissociative attachment. Electron-impact detachment of O^- ions and dissociative recombination of O_2^+ ions are also included. Regarding O_2^+ ions, elastic collisions with the background gas are considered, namely isotropic scattering and charge exchange. The O^- ions interact with the background gas by means of elastic scattering and detachment. Upon collision of O^- and O_2^+ ions, mutual neutralization is taken into account. Finally, associative detachment is considered upon collisions of O^- ions and $O_2(a^1\Delta_g)$ singlet delta oxygen molecules.

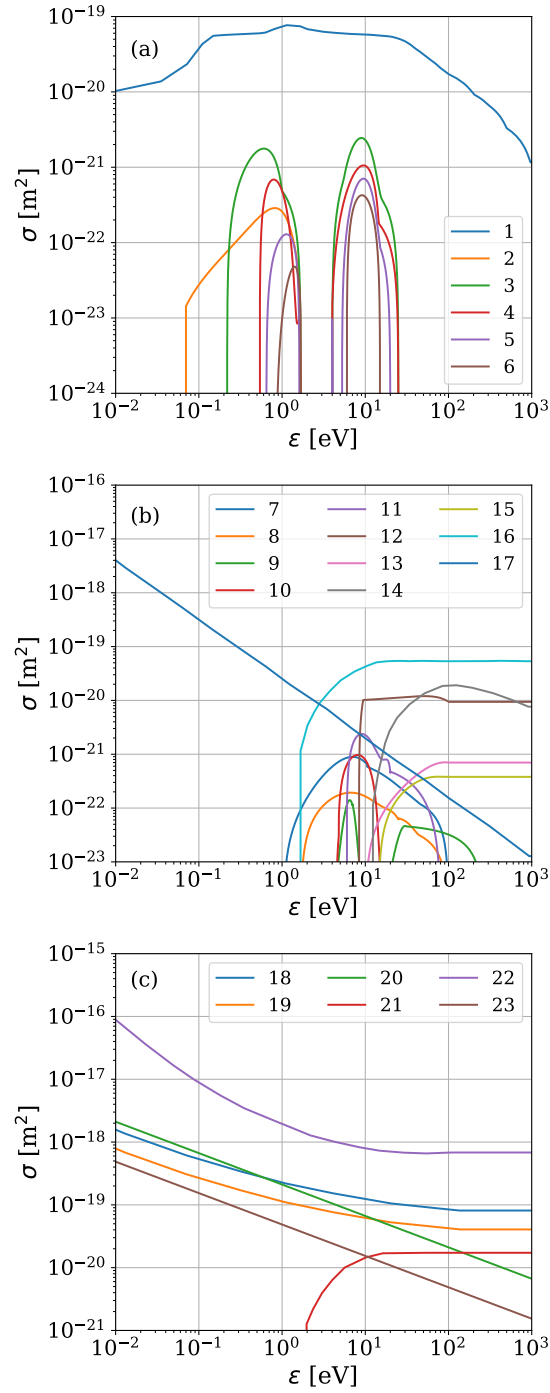FIGURE 4.1: Cross sections of the collision processes in oxygen, listed in table 4.1 (processes 1–23) as a function of the kinetic energy of the projectile. For ions, ε is the kinetic energy in the center-of-mass frame.

Although the coordinates of the metastable $O_2(a^1\Delta_g)$ molecules are not traced in the simulation, their density is calculated from a balance equation (see details in

[22]): the $O_2(a^1\Delta_g)$ creation term is the electron-impact metastable excitation rate (process 7 in table 4.1), which is directly calculated in the simulation, and the loss term is quenching at the electrode surfaces. Although $O_2(a^1\Delta_g)$ metastables can also be lost in associative detachment (the collision of O^- with a $O_2(a^1\Delta_g)$, process 23 in table 4.1), this channel is negligible in comparison with the surface loss, as it will be proved later in this chapter. The surface loss is considered by a constant α quenching coefficient in the simulation. The value of this parameter varies in a wide range according to the literature [69, 127, 128]. However, its value is critical, since it strongly affects the negative ion densities and the electronegativity of the discharge [110, 116, 127], because the main loss channel of O^- ions is associative detachment. In this study, $\alpha = 6 \cdot 10^{-3}$ is chosen. This value has been experimentally validated in previous studies of oxygen CCPs [22, 110, 122, 123].

4.2.2   Surface processes

Regarding the interaction of plasma particles with the electrode surface, various models are applied and compared.

4.2.2.1   Modelling of electrons

For the electrons, I use two different models: (i) A simple approach in which the electrode surfaces reflect the primary electrons (PEs) with a fixed probability of $\eta_e = 0.2$, regardless of their energy and angle of incidence [97]. (ii) The second approach is more realistic, differentiating three possible processes by means of the electron-surface interaction: elastic reflection, inelastic reflection and true secondary electron emission. All of them are considered by coefficients depending on the energy (ε) and the angle of incidence (θ) of the PE [9, 81]:

$$\sigma(\varepsilon, \theta) = \eta_e(\varepsilon, \theta) + \eta_i(\varepsilon, \theta) + \delta(\varepsilon, \theta), \tag{4.1}$$
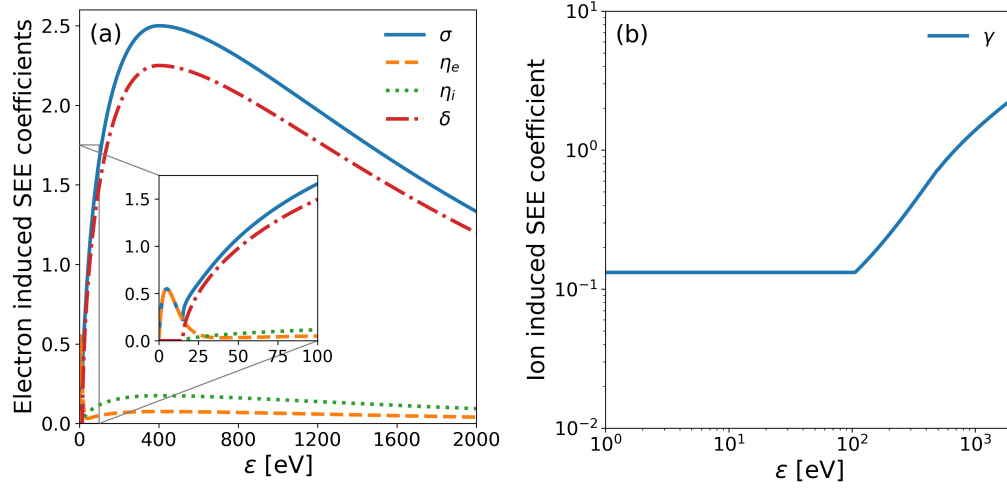
FIGURE 4.2: (a) SEE coefficient for SiO_2 surface: the total electron induced SEE coefficient (σ) and the partial emission coefficients of elastic reflection (η_e), inelastic reflection (η_i), and electron induced SEE (δ) as a function of the incident electron energy, for normal incidence. (b) SE yield on oxidized metal surfaces due to O_2^+ ions as a function of the incident ion energy [129].

where σ is the total SE yield, η_e is the elastic reflection yield, η_i is the inelastic reflection yield and δ is the electron induced SE yield (δ-electron yield, yield of true SEs). These yields are specific for the surface properties, which can be tuned via 10 parameters. In the current study, the electrodes are assumed to be made of SiO_2, for which the parameter values are shown in table 4.2. This parametrization of the model corresponds to earlier PIC/MCC simulation studies of CCPs with SiO_2 electrodes [41, 51, 81, 103–107]. In figure 4.2(a), the total SE yield σ and the partial yields η_e, η_i and δ are shown as a function of the PE energy, for normal incidence.

TABLE 4.2: Parameters for the realistic model of SEE from SiO_2 electrode.

#	Parameter	Description	Value	References
1	ε_0	threshold energy for electron induced SEE	15 eV	[17]
2	$\varepsilon_{\mathrm{max},0}$	energy of PE at the maximum emission	400 eV	[17]
3	$\sigma_{\mathrm{max},0}$	maximum emission at normal incidence	2.5	[17]
4	k_s	smoothness factor of the surface	1	[21]
5	$\varepsilon_{e,0}$	threshold energy for elastic reflection	0 eV	
6	$\varepsilon_{e,\mathrm{max}}$	energy of PE at the maximum elastic reflection	5 eV	[18]
7	$\eta_{e,\mathrm{max}}$	maximum of the elastic reflection	0.5	[18]
8	Δ_e	control parameter for the decay of η_e	5 eV	
9	r_e	portion of elastically reflected electrons	0.03	[17]
10	r_i	portion of inelastically reflected electrons	0.07	[17]

4.2.2.2 Modelling of heavy particles

In case of the interaction of heavy particles with the electrodes, two different approaches are applied: (i) In the simple one, a constant $\gamma = 0.4$ is assumed for the O_2^+ ions. This choice of γ has already been applied for dielectric surfaces in CCP simulations [32, 81]. (ii) In the realistic model, an energy-dependent SE yield is applied for the O_2^+ ions, according to the formula given in [79] for O_2^+ ions hitting untreated (oxidized) metal surfaces. Figure 4.2(b) shows this γ as a function of the ion energy. Below ≈ 100, when the potential ejection mechanism is operational, the SE yield due to O_2^+ ions is 0.13, at higher energies it exhibits an increase because of the onset of the kinetic ejection process. The interaction between O^- ions and the electrodes is ignored, as their density is very low outside the plasma bulk region.

4.2.2.3 Setup of various surface models

TABLE 4.3: Overview of the surface coefficients used in the discharge models A, B and C. For electrons and O_2^+ ions, simple (constant surface coefficients) and realistic approaches (energy-dependent surface coefficients) are combined in the different models [129].

Species	Surface coefficients	Model A	Model B	Model C
e⁻	$\eta_e = 0.2$	X		
	$\eta_e(\varepsilon),\ \eta_i(\varepsilon),\ \delta(\varepsilon)$		X	X
O_2^+	$\gamma = 0.4$	X	X	
	$\gamma(\varepsilon)$			X

From the combination of the simple/realistic approaches for the electrons and the ions, three different surface models are implemented, referred to as model A, B, and C, see table 4.3. In model A, both electrons and ions are treated in the simple way, by constant coefficients. In model B, γ is still constant, while the realistic approach is used for the electron-surface interaction. In model C, realistic methods for both the electron-surface and ion-surface interactions are used.

4.2.3 Discharge conditions

In the simulations, the electrode gap is 6.7 cm, the pressure is 0.7 Pa, the driving voltage is sinusoidal with a frequency of 13.56 MHz and the voltage amplitudes are between 500 V and 1200 V. The temperature of the background gas is assumed to be 400 K.

4.3 Results

In the following, the effect of varying the driving voltage amplitude from 500 V to 1200 V on the discharge characteristics will be discussed at a constant pressure of 0.7 Pa, by PIC/MCC simulations using the surface models A, B and C. Figure 4.3 compares the densities of charged particles (O_2^+ ions, electrons and O^- ions) at the discharge center and the ratio of the densities of $O_2(a^1\Delta_g)$ metastable molecules to O_2 molecules based on the three different models. In case of model A, which assumes constant surface coefficients of $\eta_e = 0.2$ and $\gamma = 0.4$, the central densities of charged particles increase slightly as the driving voltage amplitude is increased. The O_2^+ ion density raises by a factor of 1.5 approximately (see figure 4.3(a)), while the electron density increases 1.8 times (figure 4.3(b)). At the same time, the O^- ion density increases 1.5 times (figure 4.3(c)), while the $O_2(a^1\Delta_g)$ metastable molecule density increases by a factor of 1.4 times (figure 4.3(d)). However, the $O_2(a^1\Delta_g)$ density is less than 1% of the ground state density for all voltage amplitudes. The electron density is low (less than 2.3×10^{14} m^{-3}) compared to the O_2^+ ion and O^- ion densities within the whole range of the voltage amplitude. The O^- ion density is similar to the O_2^+ ion density (between 4.5×10^{15} m^{-3} and 6.9×10^{15} m^{-3}, with less than 4% difference between the two species for all ϕ_0). The O^- ion density is much higher than the electron density at the discharge center: 36 times higher at $\phi_0 = 500$ V and 29 times higher at $\phi_0 = 1200$ V.
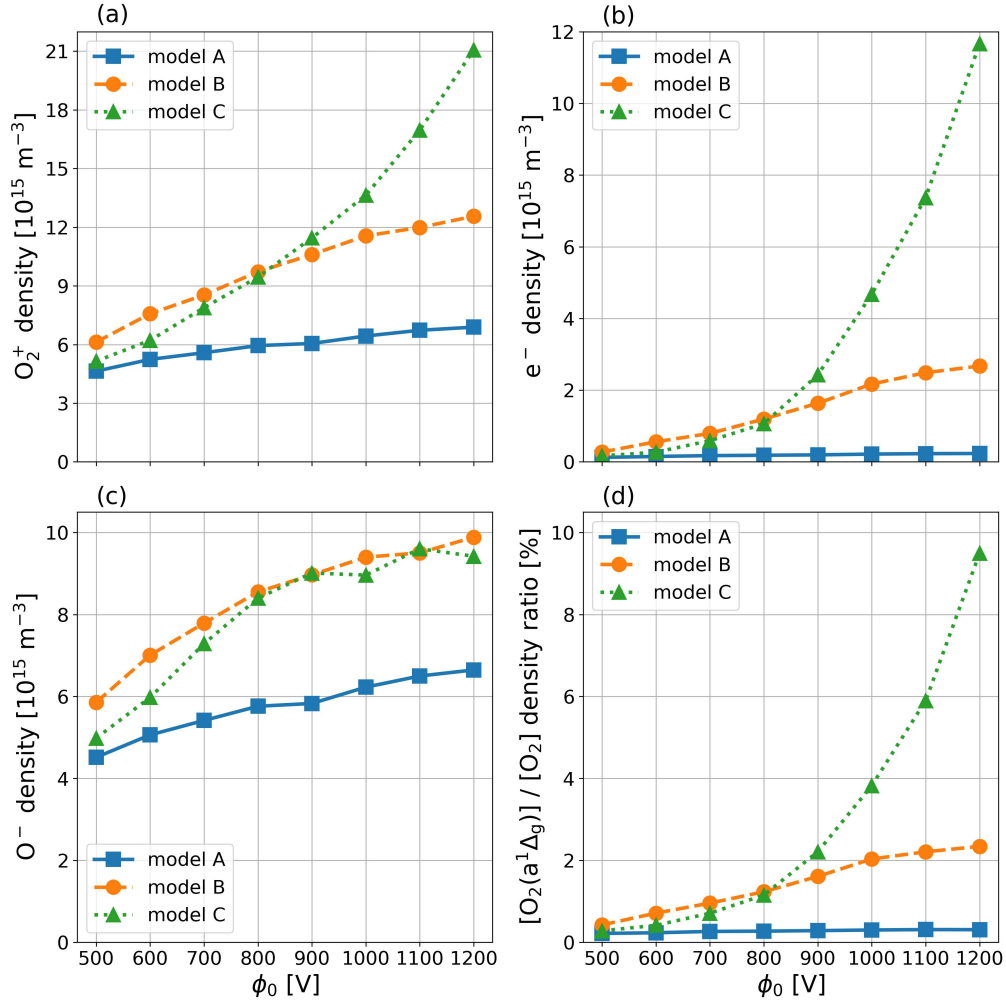
FIGURE 4.3: Densities of (a) O_2^+ ions, (b) electrons and (c) O^- ions at the center of the discharge and (d) the $[O_2(a^1\Delta_g)]/[O_2]$ density ratio as a function of the driving voltage amplitude, ϕ_0, based on the different models A, B, and C. Discharge conditions: O_2 gas, SiO_2 electrodes, $L = 6.7$ cm, $p = 0.7$ Pa, $f = 13.56$ MHz [129].

Figure 4.4 shows the time-averaged charged particle density distributions based on the different models (models A, B and C in rows from top to bottom) at three different voltage amplitudes (500 V, 1000 V and 1200 V in columns from left to right). (Note that the scales of the vertical axis are different within a row, but they are the same within each column.) Results based on model A (first row) show that the electron density is depleted in the bulk region for all ϕ_0. The negative charges in the discharge are dominantly carried by O^- ions in this region, their density being

approximately equal to that of O_2^+ ions. Consequently, the global electronegativity of the discharge under these conditions is higher than 1, as shown in figure 4.5, in which the global electronegativity is shown as a function of the voltage amplitude at 0.7 Pa, based on the different models. Model A yields a global electronegativity of 21 at $\phi_0 = 500$ V and it decreases as the voltage amplitude is increased, reaching a value of 13.5 at $\phi_0 = 1200$ V.
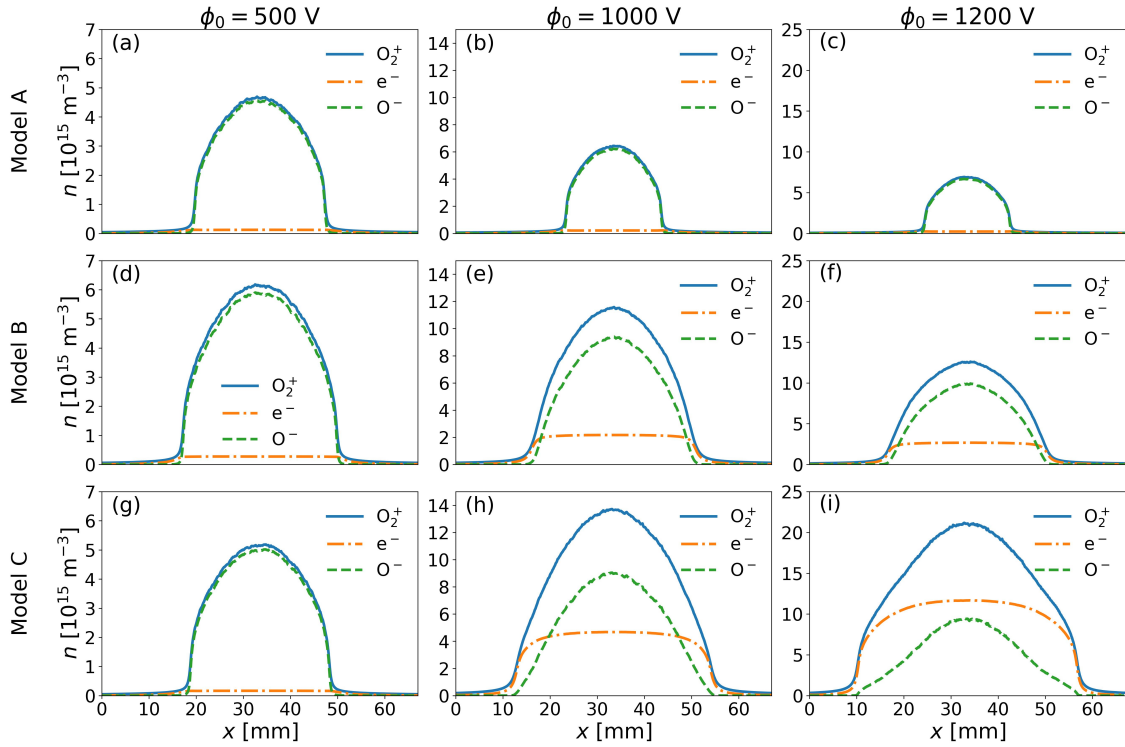
FIGURE 4.4: Time averaged charged particle density profiles based on model A (first row), model B (second row) and model C (third row), for various voltage amplitudes: $\phi_0 = 500$ V (first column), $\phi_0 = 1000$ V (second column) and $\phi_0 = 1200$ V (third column). Discharge conditions: O_2 gas, SiO_2 electrodes, $L = 6.7$ cm, $p = 0.7$ Pa, $f = 13.56$ MHz [129].

In model B, the realistic description of the electron-surface interaction considering electron-induced SEE is included, while a constant $\gamma = 0.4$ is used for the positive ions. This model shows a significant increase of the plasma density when the voltage amplitude is increased. The O_2^+ density raises by a factor of 2 (from 6.1×10^{15} m^{-3} to 1.3×10^{16} m^{-3}), while the electron density increases by 10 times (from 2.7×10^{14} m^{-3} to 2.7×10^{15} m^{-3}) as we change ϕ_0 from 500 V to 1200 V (figure 4.3(a) and (b)).

The O^- density increases by 1.7 times (from 5.9×10^{15} m^{-3} to 9.9×10^{15} m^{-3}) at the same time (figure 4.3(c)). In comparison with model A, model B gives 1.8 times higher O_2^+ density at the highest voltage amplitude of 1200 V, and 1.3 times higher at $\phi_0 = 500$ V. For the electrons, model B gives 11.5 times higher density than model A at $\phi_0 = 1200$ V, and 2.2 times higher density at $\phi_0 = 500$ V. For the O^- density, model B gives 1.3 and 1.5 times higher density than model A at the lowest and the highest voltage amplitude, respectively. These results show that the electron-surface interaction has a more significant effect on the calculated charged particle densities at high voltage amplitudes (similarly to the case of electropositive argon CCPs for similar discharge conditions [81]). This is also visible in figure 4.4 by comparing the plots in the first row (model A) to the ones in the second row (model B). The electron density is remarkably higher in the bulk region based on model B when we increase the voltage amplitude. For all ϕ_0, the discharge has lower global electronegativity based on model B than model A (see figure 4.5). Model B gives a global electronegativity of 13.8 at $\phi_0 = 500$ V and it drops below 2.5 at high voltage amplitudes.

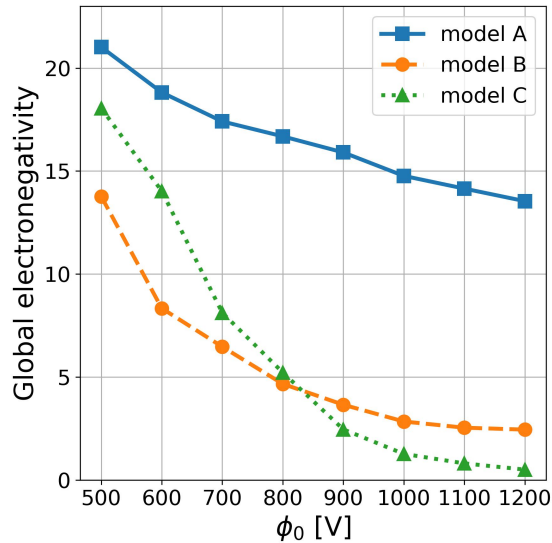FIGURE 4.5: Global electronegativity of the discharge as a function of the driving voltage amplitude, ϕ_0, based on the three different models. Discharge conditions: O_2 gas, SiO_2 electrodes, $L = 6.7$ cm, $p = 0.7$ Pa, $f = 13.56$ MHz [129].

In parallel with the increase of the electron density as a result of treating electron-surface interactions realistically (model B), the particle balance of other species and the electronegativity is affected as well. As it is shown in figure figure 4.3(b), the density of $O_2(a^1\Delta_g)$ molecules is increased according to a similar trend as the electron density. The metastable density ratio raises by a factor of 5.5 when the voltage is increased from 500 V to 1200 V. The reason behind this is that the source channel of metastables is electron-impact excitation (process 7 in table 4.1). Note that the rate of $O_2(a^1\Delta_g)$ loss by gas phase collisions, i.e. associative detachment with O^- ions (process 23) is orders of magnitude lower than the metastable excitation rate under the conditions investigated here. The dominant loss channel for the $O_2(a^1\Delta_g)$ particles is surface quenching, with a rate proportional to their density. This way an increased number of electrons results in an increased number of metastables. At the highest driving voltage amplitude of 1200 V, the $O_2(a^1\Delta_g)$ density ratio is ≈ 2.3 % of the background ground state gas based on model B (figure 4.3(d)). The increase of the electron density also has an effect of decreasing the electronegativity, as it has already been mentioned in connection with figure 4.5. In addition to the direct and obvious way (see equation 1.9), an indirect mechanism comes into play: as the $O_2(a^1\Delta_g)$ metastable concentration increases, the associative detachment rate (process 23 in table 4.1, in which a $O_2(a^1\Delta_g)$ metastable collides with a O^- ion, leading to the destruction of both particles, resulting in a neutral ozone molecule and an electron) increases remarkably (approximately by an order of magnitude according to results of model B, as the driving voltage is increased from 500 V to 1200 V). At the same time, the detachment and the mutual neutralization rates (processes 21 and 22) increase moderately. This way associative detachment becomes the primary loss channel of negative ions when the metastable density is enhanced. Practically, O^- ions are "killed" by metastables. Note that the source rate of O^- ions also raises as the electron density increases, as it is also an electron-impact process, the dissociative attachment (process 9 in table 4.1). However, this source rate increases moderately compared to the loss rate (approximately by a factor of 4.8 according to model B as the driving voltage changes from 500 V to 1200 V, while

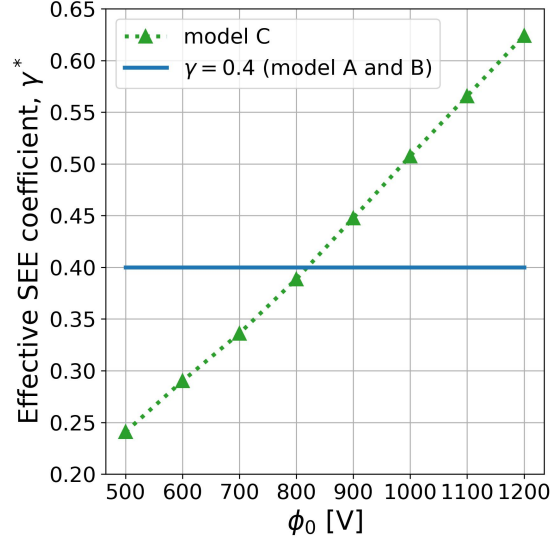the associative detachment rate increases by a factor of 9 at the same time).

FIGURE 4.6: The γ^* self-consistently calculated effective ion induced SEE coefficient, as a function of the driving voltage amplitude, ϕ_0, obtained from model C. The continuous blue line indicates the constant $\gamma = 0.4$ SEE coefficient used in models A and B. Discharge conditions: O_2 gas, SiO_2 electrodes, $L = 6.7$ cm, $p = 0.7$ Pa, $f = 13.56$ MHz [129].

Model C incorporates the realistic, energy-dependent approaches for both the electrons and the O_2^+ ions colliding with the electrode surface. According to this model, an exponential increase of the O_2^+ ion and electron densities is obtained as a function of ϕ_0 (see figure 4.3(a) and (b)). Between 500 V and 1200 V, the O_2^+ ion density increases by a factor of 4 (from 5.1×10^{15} m^{-3} to 2.1×10^{16} m^{-3}), while the electron density increases 70 times (from 1.7×10^{14} m^{-3} to 1.2×10^{16} m^{-3}). The density of $O_2(a^1\Delta_g)$ metastable molecules follows a similar trend and raises by a factor of 34, reaching about 10% at the highest voltage amplitude (figure 4.3(d)). The density of negative ions increases by a factor of 1.9 (from 5.0×10^{15} m^{-3} to 9.4×10^{15} m^{-3}) as ϕ_0 is increased to 1200 V from 500 V (figure 4.3(c)). In the simulations applying model C, an average (effective) ion induced SEE coefficient γ^* is calculated self-consistently as

$$\gamma^* = \sum_{k=1}^{N_i} \gamma(\varepsilon_k)/N_i, \tag{4.2}$$

where N_i is the total number of O_2^+ ions arriving at a given electrode during a RF period, ε_k is the energy of the kth O_2^+ ion upon arrival at the electrode, and $\gamma(\varepsilon_k)$ is the energy-dependent SE yield due to this ion. When the voltage is higher, the average energy of O_2^+ ions is higher, leading to a higher γ^* average SE yield. Under the conditions studied here, the upper limit of the energy distribution of O_2^+ ions is about 540 eV. The SE yield at this energy is 0.77 (see figure 4.2(b)). In figure 4.6, the γ^* effective SEE coefficient is shown as a function of ϕ_0. Within the interval of the driving voltage investigated here, the γ^* coefficient increases linearly, from $\sim$0.25 at 500 V to $\sim$0.65 at 1200 V. Above 800 V, γ^* exceeds 0.4 (the value of the constant γ coefficient used in models A and B). As a result, model C exhibits lower electron and positive ion densities below 800 V and higher densities above 800 V than model B (see figure 4.3(a) and (b)). This is also evident by figure 4.4, comparing the second row (model B) and the third row (model C). In comparison with model B, model C results in higher plasma densities and narrower sheaths at high voltages, and the ratio of negative charges in the bulk region is also different. At 1200 V, the electron density exceeds the O^- ion density (figure 4.4(i)), resulting in a low discharge electronegativity value of 0.5 at $\phi_0 = 1200$ V (figure 4.5). Based on model C, the electronegativity is 18 at $\phi_0 = 500$ V, and drops below 1 above 1000 V. Compared to model B, the electronegativity is higher at low voltages (the maximum difference being 5.7) and lower at high voltages (the maximum difference being 1.94) according to model C, see figure 4.5. Compared to model A (assuming constant surface coefficients), both model B (treating electrons realistically at the surface) and model C (treating both electrons and ions realistically) yields significantly lower electronegativity.

Figure 4.7 shows more details about how electron induced SEs affect the discharge characteristics. It displays the spatio-temporal plots of the electron density (first row), the electric field (second row), the electron power absorption (third row) and the ionization rate (forth row) at $\phi_0 = 1200$ V, which is the highest voltage amplitude used in this work. The columns correspond to results based on models A, B and
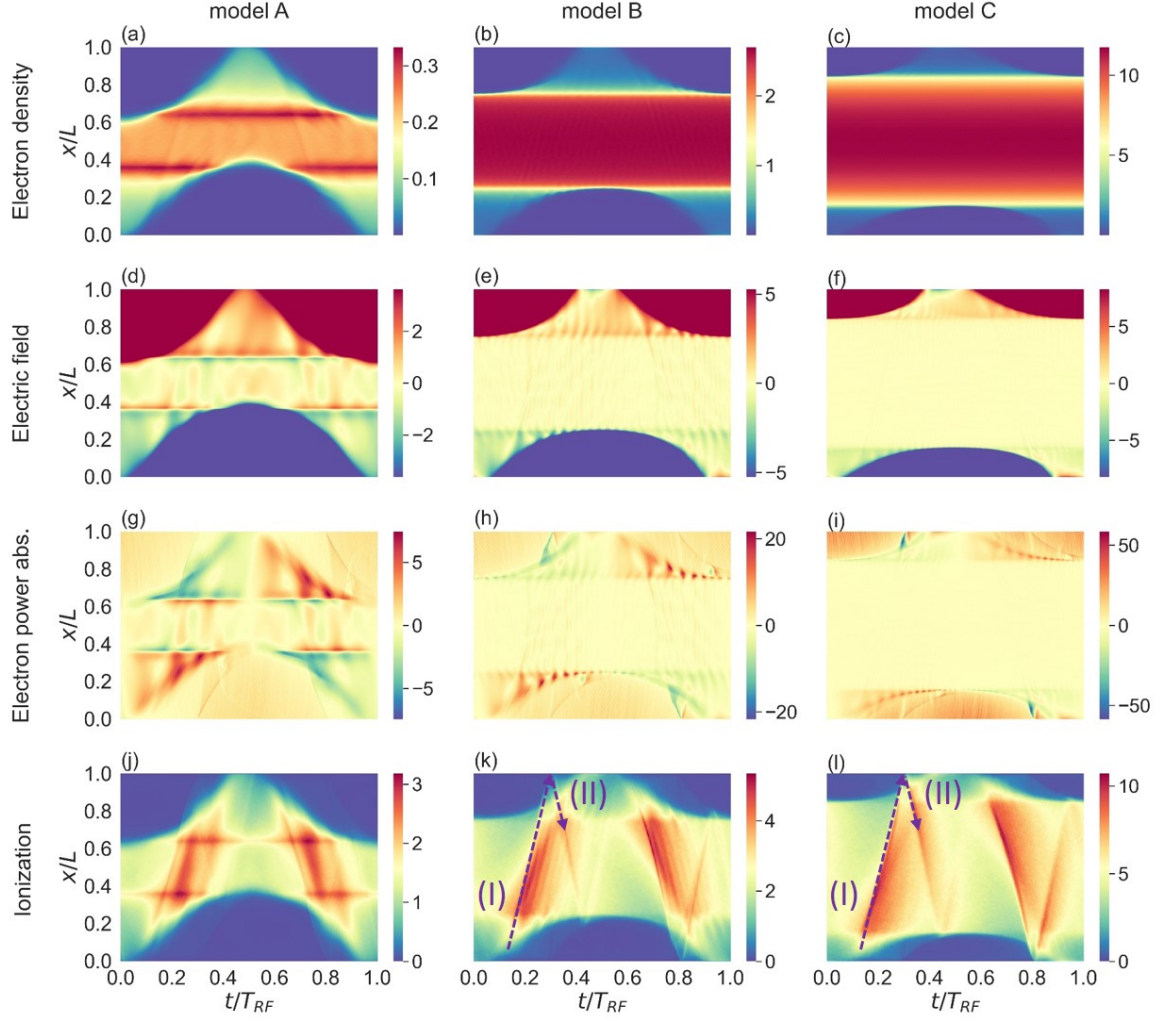
FIGURE 4.7: Spatio-temporal distributions of the electron density $[10^{15} \text{ m}^{-3}]$ (first row, (a)-(c)), the electric field $[10^3 \text{ Vm}^{-1}]$ (second row, (d)-(f)), the electron power absorption $[10^4 \text{ Wm}^{-3}]$ (third row, (g)-(i)) and the total ionization rate $[10^{20} \text{ m}^{-3}\text{s}^{-1}]$ (fourth row, (j)-(l)), for model A (left column), model B (center column) and model C (right column). The horizontal axes correspond to one RF period. The vertical axes show the distance from the powered electrode. The powered electrode is located at $x/L = 0$, while the grounded electrode is at $x/L = 1$. $T_{\text{RF}} = 1/f$. The dashed lines in panels (k) and (l) indicate the strong ionizing beams related to SEs. Discharge conditions: O_2 gas, SiO_2 electrodes, $L = 6.7$ cm, $p = 0.7$ Pa, $\phi_0 = 1200$ V, $f = 13.56$ MHz [129].

C (from left to right). Based on model A (applying constant $\eta_e = 0.2$ and $\gamma = 0.4$ parameters), a temporal modulation of the electron density, the electric field and the electron power absorption can be observed within the plasma bulk. This model results in a low electron density (see figure 4.3(b) and figure 4.4(c)) and a global

electronegativity of 13.5 (figure 4.5). The electron density has local maxima at the edges of the bulk region called electropositive edge (figure 4.7(a)). This feature, along with the nonzero electric field (figure 4.7(d)) and the corresponding electron power absorption (figure 4.7(g)) within the bulk region indicates DA discharge operation mode. In the spatio-temporal distribution of the ionization rate (figure 4.7(j)), typical features of the DA-mode can be seen as well. Namely, ionization in the center of the discharge caused by the drift electric field and ionization at the collapsing sheath edges caused by the ambipolar field at the sheath edges caused by the local peaks of the electron density in the electropositive edge region of the discharge. In addition, intense power absorption at the edges of the expanding sheaths and the generation of multiple ionizing electron beams is also detected, resulting in a complex ionization pattern (figure 4.7(j)).

In contrast to the results of model A, the spatio-temporal distributions based on model B (considering the interaction of electrons with the surface realistically, taking electron-induced SEs into account) are significantly different (see the second vs the first column in figure 4.7). The electropositive edge disappears and the bulk becomes stationary (figure 4.7(b)). The electron density maxima is an order of magnitude higher than in case of model A (2.7×10^{15} m^{-3} versus 2.4×10^{14} m^{-3} at the center of the discharge, see figure 4.3(b) for $\phi_0 = 1200$ V), and the sheaths are thinner (see also figures 4.4(c) and (f)). The electric field is negligible in the bulk (figure 4.7(e)), and the electron power absorption is localized in the expanding sheath regions (figure 4.7(h)). The ionization rate also exhibits maxima at the edges of the expanding sheaths (figure 4.7(k)), which is characteristic of α-mode. These features are characteristic of an electropositive CCP. Indeed, the electronegativity has a low value of 2.5 under these conditions (see figure 4.5). Furthermore, the time-modulated fine structures in the electric field, the electron power absorption and the ionization dynamics have higher frequency in model B compared to model A. The reason is that the higher density causes a higher electron plasma frequency.
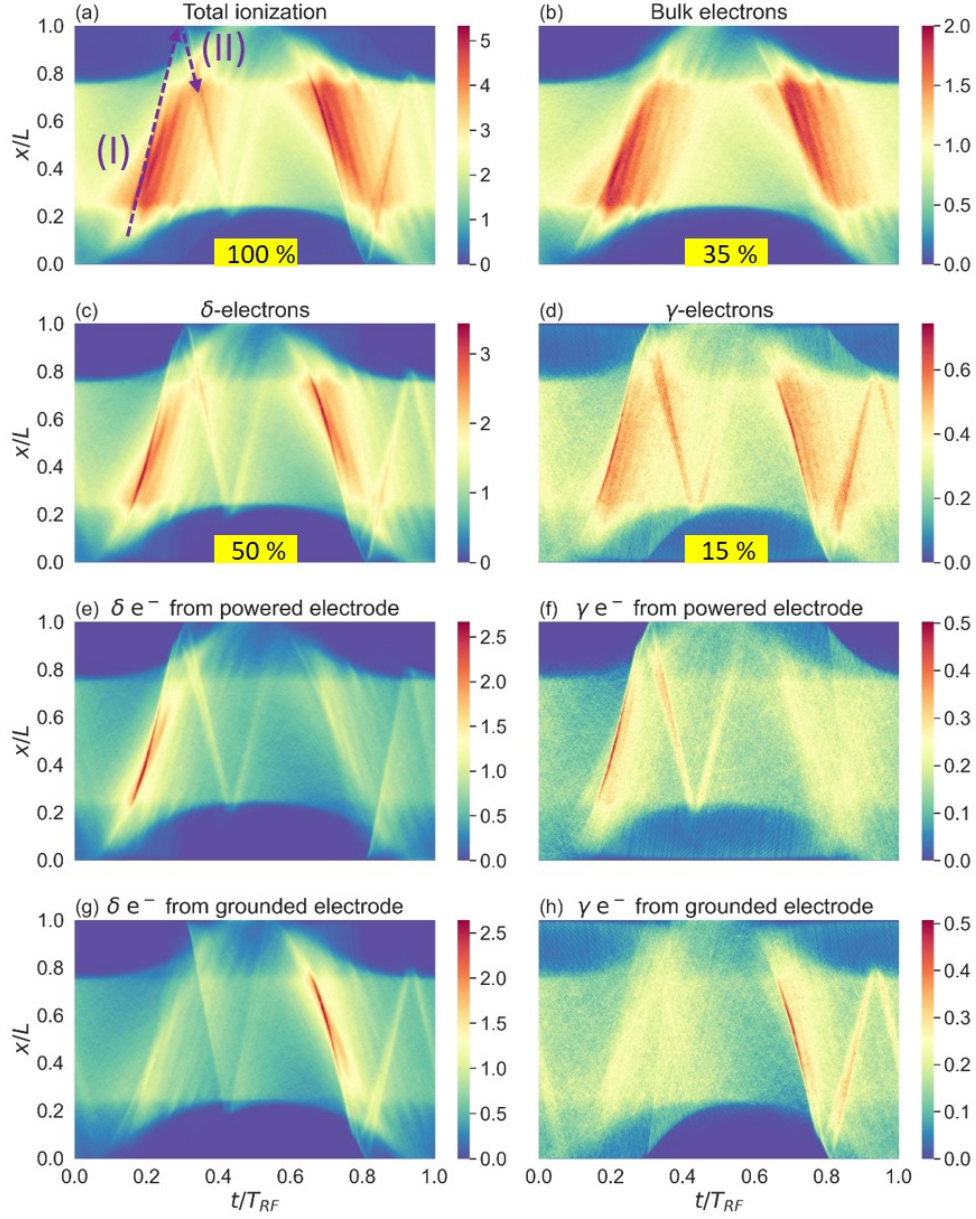
FIGURE 4.8: Spatio-temporal plots of the (a) total ionization rate and the ionization caused by (b) bulk electrons, (c) δ-electrons and (d) γ-electrons at $\phi_0 = 1200$ V, according to model B. The ionization due to δ-/γ-electrons originated at the powered/grounded electrode are shown in panels (e)-(h). Panel (a) is identical to figure 4.7(k). The color scales are in units of $[10^{20}$ m^{-3}s$^{-1}]$. The powered electrode is located at $x/L = 0$, while the grounded electrode is at $x/L = 1$. $T_{\mathrm{RF}} = 1/f$. The numeric ratios of the contributions of the various "types" of electrons to the ionization is shown in the yellow rectangles in panels (a)-(d). Discharge conditions: O_2 gas, SiO_2 electrodes, $L = 6.7$ cm, $p = 0.7$ Pa, $\phi_0 = 1200$ V, $f = 13.56$ MHz [129].

The ionization rate obtained from model B exhibits some interesting additional patterns. At the phase of sheath expansion, multiple electron beams are generated. In addition, an ionizing electron beam (beam II in panel (k)) also starts from the grounded electrode when a strong ionizing beam from the powered electrode (beam I in panel (k)) arrives. The same ionization patterns can be seen half an RF period later at the opposite electrode. This phenomenon was seen before in electropositive argon CCPs [81]: beam II at the grounded electrode is the direct consequence of the incidence of beam I. This second beam consists of electrons reflected from the sheath edge and electron-induced SEs (δ-electrons) emitted from this electrode surface by the impact of beam I. More details on the ionization dynamics are shown in figure 4.8, introducing the spatio-temporal distribution of the total ionization rate and the ionization rates by different "types" of electrons at $\phi_0 = 1200$ V. In panel (a), the total ionization rate is shown, which is identical with panel (k) in figure 4.7. Panel (b) shows the contribution of bulk electrons (electrons created in ionizing collisions) to the total ionization rate. Panel (c) shows the contribution of δ-electrons (electron-induced SEs) and the contribution of γ-electrons (ion-induced SEs) is shown in panel (d). In panels (e)-(h), the ionization rates caused by these two SE species are decomposed according to which electrode they were created at (the powered or the grounded electrode). Based on figure 4.8, it is clear that beam II consists of secondary electrons generated at the electrodes (δ- and γ-electrons), and no bulk electrons have a contribution to it. It is also notable that δ-electrons are responsible for the highest portion of the ionization: about 50% is directly caused by them, while 15% is caused by γ-electrons and bulk electrons cause the remaining 35% of the ionization. Additionally, figure 4.8 shows multiple reflections of the high-energy electron beams of γ- and δ-electrons.

The discharge model C includes energy-dependent coefficients for ion-induced SEE, electron-induced SEE and electron reflection (elastic and inelastic as well), i.e. it is complemented with a realistic approach of ion-induced SEE compared to model B. Under the same discharge conditions, this model results in even more electropositive

plasmas than model B. The spatio-temporal plots corresponding to model C are shown in the third column of figure 4.7. Compared to model B (see the second column), the time-modulated structures in the bulk region disappear, and a clear α-mode can be observed. Beam II, the ionizing electron beam caused by SEs is significantly stronger than the one obtained by model B (figure 4.7(l) vs 4.8(k)). The stronger ionization and the higher particle densities in model C are caused by the higher number of SEs induced by O_2^+ ions. The self-consistently calculated effective SEE coefficient is $\gamma^* = 0.62$ for $\phi_0 = 1200$ V. The higher number of γ-electrons generated compared to model B (where $\gamma = 0.4$) enhance the ionization directly and indirectly, i.e. through the effect of γ-electrons on the creation of δ-electrons. In model C, at $\phi_0 = 1200$ V, γ-electrons cause 20% of the ionization directly; δ-electrons cause 45% directly and bulk electrons cause 35%. Note that γ-electrons and δ-electrons also affect the ionization by bulk electrons indirectly, since many bulk electrons are created by ionization caused by γ-electrons and δ-electrons.

As δ-electrons are responsible for the highest portion of the ionization when the surface processes are treated realistically, and beam II was found to be composed by secondary electrons, the emission dynamics of δ-electrons will be discussed in more detail below. Figure 4.9 shows the outgoing δ-electron fluxes at the electrodes at $\phi_0 = 1200$ V, based on models B and C. The fluxes of emitted δ-electrons are split by the primary electron type and the electrode where the PEs originate from. At the grounded electrode, the emission of δ-electrons happens when the sheath is collapsed, between $0.3 < t/T_{RF} < 0.8$. Around $t/T_{RF} = 0.3$, there is a sharp peak of emitted δ-electrons induced by δ-electrons originating from the opposite (powered) electrode. The mechanism behind this is that δ-electrons being accelerated heavily during sheath expansion at the powered electrode and contributing to beam I reach the opposite electrode after overcoming the local residual sheath potential around $t/T_{RF} = 0.3$. Upon impact on the electrode, they can induce new δ-electrons. These electrons are instantly accelerated backwards by the residual sheath potential, contributing to beam II. At the phase of total sheath collapse (around $t/T_{RF} = 0.5$),
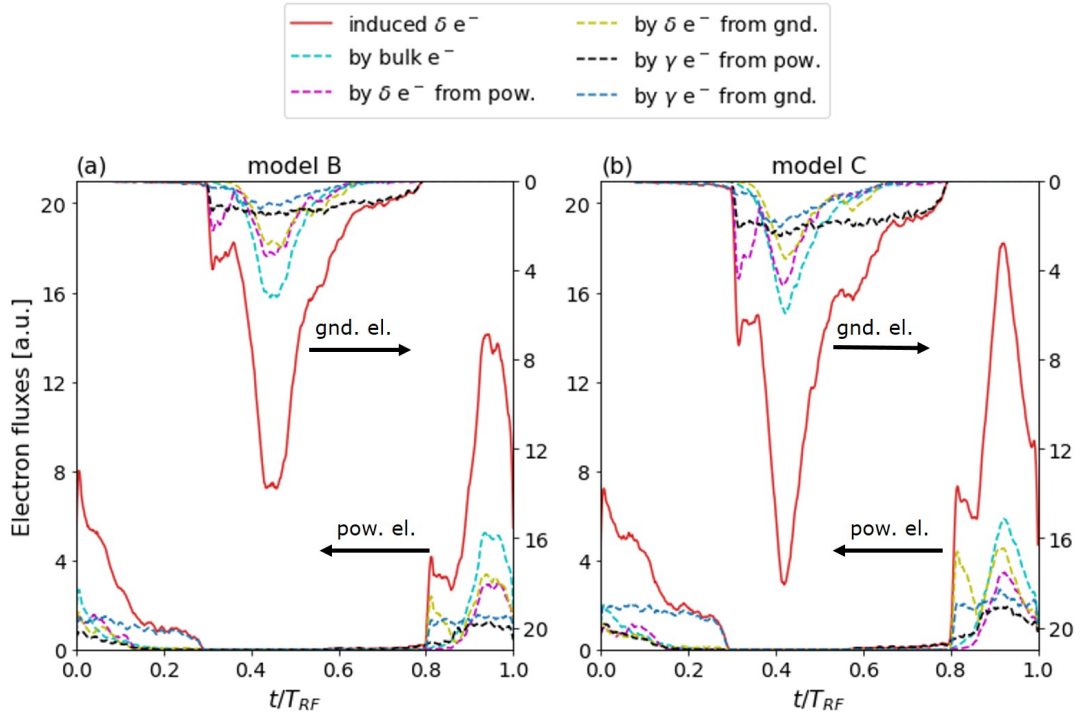
FIGURE 4.9: Time-resolved fluxes of the emitted δ-electrons with the contributions of the various "types" of electrons to their emission at the powered (bottom and left axes) and grounded (top and right axes) electrodes, obtained from (a) model B and (b) model C. Discharge conditions: O_2 gas, SiO_2 electrodes, $L = 6.7$ cm, $p = 0.7$ Pa, $\phi_0 = 1200$ V, $f = 13.56$ MHz [129].

another peak of δ-electrons induced by δ-electrons born at the opposite electrode is observed at the grounded electrode. At the same time, bulk electrons also cause the emission of δ-electrons. These δ- and bulk electrons inducing δ-electrons during the totally collapsed phase of the sheath have less energy and they can only reach the electrode when the sheath is fully collapsed. δ-electrons emitted this way are not pushed away instantly from the electrode of origin, due to the lack of the sheath potential. Instead, these δ-electrons stay near the electrode, and they are only accelerated away at the next sheath expansion phase (around $t/T_{\rm RF} = 0.7$), contributing to beam I.

Figure 4.9 implies that γ-electrons also play an essential role in the SEE dynamics. A significant portion of outgoing δ-electrons are generated by γ-electrons. At the grounded electrode, γ-electrons originating from the opposite electrode cause the

emission of δ-electrons through half of the RF period, between $0.3 < t/T_{\mathrm{RF}} < 0.8$ (see the black curves in figure 4.9). γ-electrons from the same (grounded) electrode also result in a peak of emitted δ-electrons, limited to the phase of total sheath collapse, like bulk electrons and some δ-electrons.

Regarding the comparison of model B and C, the electron emission dynamics are similar in case of the two models (see the left and right panels of figure 4.9). The main effect of applying model C instead of model B is that the flux of δ-electrons emitted by γ-electrons is higher, since the self-consistently calculated effective γ^* SEE coefficient is higher than the constant value used in model B (0.62 vs 0.4). As an indirect effect, the emitted flux of δ-electrons created by δ-electrons from the opposite electrode at the phase of partial sheath collapse (around $t/T_{\mathrm{RF}} = 0.3$ at the grounded electrode) also increases in comparison with model B, which increases the ionization rate further.

4.4 Summary

After emphasizing the critical role of the SEE coefficient regarding PIC/MCC simulations of electropositive discharges in the previous chapter, the interaction of ions and electrons with the electrode surface was studied in the current chapter, combining simple/realistic approaches in the PIC/MCC simulations of oxygen CCPs. This study was preceded by a numerical study on electron-induced secondary electrons in argon CCPs under similar conditions [81]. That earlier study used two models in PIC/MCC simulations for the interaction of electrons with the electrode surface: a simple model with only elastic reflection of electrons with a fixed probability of 0.2 (model A), and a realistic model for SiO_2 electrodes, with electron-induced SEE and energy-dependent reflection coefficients (model B). On the other hand, the ion-induced SEE was treated by a constant γ coefficient of 0.4. In the current work, I implemented the realistic model for the electron–surface interaction to the

PIC/MCC simulation of oxygen CCPs. In addition, I extended the simulation study by including SEE by O_2^+ ions with energy-dependent secondary electron yields.

Similarly to the case of argon, treating the interaction of electrons with the surface realistically instead of assuming only a constant elastic reflection coefficient caused a significant increase of the particle densities in oxygen, and a complex electron emission and ionization dynamics dominated by δ-electrons and γ-electrons was observed. In addition, specific effects of secondary electrons were found in oxygen: the $O_2(a^1\Delta_g)$ metastable density increased with the electron density, which lowered the electronegativity in an indirect way: the associative detachment rate increased, which was found to be the primary loss channel of O^- ions. In accordance with the decrease of the electronegativity, the drift-ambipolar mode became less important for the ionization dynamics, and an α-mode appeared together with another ionizing electron beam at partial sheath collapse. Generally, the effect of secondary electrons on the discharge was found to be more significant at higher voltages.

By implementing an energy-dependent model for the ion-induced SEE in addition to the realistic model for electron–surface interactions, the effects of SEs on the discharge properties became more pronounced at high voltages. Above 800 V, the effective γ^* ion-induced SEE coefficient reached a value higher than 0.4, up to 0.62 at 1200 V. The electron density at 1200 V was 10 times higher for model B than model A, but 50 times higher for model C than model A. Also, the oxygen discharge became electropositive above 1000 V for model C.

In summary, SEE by both electrons and O_2^+ ions are important surface processes at low pressure and high voltage oxygen CCPs, which can alter the discharge properties significantly. In order to get accurate results under these conditions, PIC/MCC simulations of oxygen CCPs need to describe these processes realistically, as it was done in our most sophisticated Model C.

Chapter 5

Control of particle properties in capacitively coupled plasmas

5.1 Background

In the previous chapters, a fundamental investigation of single-frequency capacitively coupled plasmas (CCPs) was presented, with special attention on the effects of surface processes on the discharge properties and particle dynamics. In order to understand the role of various particle-surface interactions in CCPs, the complexity of the surface models used in the particle-in-cell/Monte Carlo collisions (PIC/MCC) simulations was increased step by step. In this chapter, the realistic treatment of the interactions of ions and electrons with the surface will be complemented with the energy-dependent modelling of sputtering of the electrode surface by heavy particle bombardment. In addition, fast atoms will be traced by the simulation, together with energy-dependent modelling of secondary electron emission (SEE) induced by them. By choosing copper as the electrode material in argon gas, and including the sputtering of electrodes into the surface model, CCPs relevant for applications can be investigated, with focus on the control of the sputtering yield based on the control of the energies and fluxes of heavy particles impinging the electrodes. Such

discharges relevant for industrial applications are typically driven by multifrequency waveforms, and they are operated at low pressures and high voltage amplitudes. Therefore, CCPs driven by tailored voltage waveforms (TVWs) at low pressure and high voltage will be studied in this chapter.

5.2 Simulation model and discharge conditions

In this chapter, a 1d3v PIC/MCC code for argon CCPs is applied. The electrode material assumed in the simulations is copper. In the frame of this work, the modelling of the sputtering of the electrodes by energetic plasma particles was added to the code as a new functionality.

5.2.1 Gas phase processes

TABLE 5.1: List of collision processes for CCPs in Ar with Cu electrodes.

#	Reaction	Process	References
1	$e^- + Ar \longrightarrow e^- + Ar$	Elastic scattering	[5]
2	$e^- + Ar \longrightarrow e^- + Ar^*$	Excitation	[5]
3	$e^- + Ar \longrightarrow 2e^- + Ar^+$	Ionization	[5]
4	$Ar^+ + Ar \longrightarrow Ar^+ + Ar$	Isotropic elastic scattering	[130]
5	$Ar^+ + Ar \longrightarrow Ar^+ + Ar$	Backward elastic scattering	[130]
6	$Ar^+ + Ar \longrightarrow e^- + 2Ar^+$	Ionization	[131]
7	$Ar^+ + Ar \longrightarrow Ar^+ + Ar^*$	Excitation	[131]
8	$Ar^f + Ar \longrightarrow Ar^f + Ar$	Elastic scattering	[130]
9	$Ar^f + Ar \longrightarrow e^- + Ar^f + Ar^+$	Ionization	[131]
10	$Ar^f + Ar \longrightarrow Ar^f + Ar^*$	Excitation	[131]
11	$Cu + Ar \longrightarrow Cu + Ar$	Elastic scattering	[132]

In the simulations, four types of particles are considered: electrons, Ar^+ ions, fast Ar neutrals (Ar^f), and sputtered Cu atoms. They interact with the background Ar gas atoms through various collision processes, which are shown in table 5.1 and their cross sections are plotted in figure 5.1. Electrons can be scattered elastically and are able to excite or ionize the gas atoms. Ar^+ ions and Ar^f fast neutrals can also be scattered elastically (isotropically in case of both species and backwards in case of
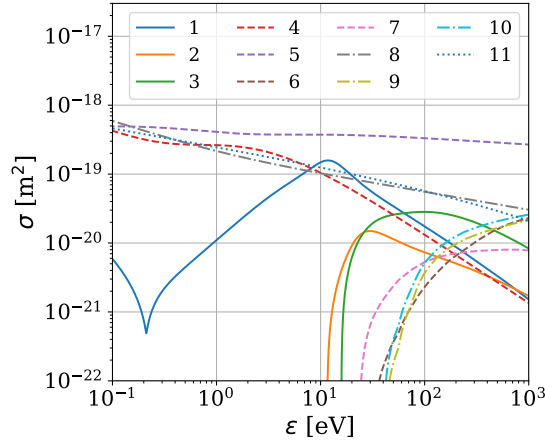
FIGURE 5.1: Cross sections of the collision processes included in the simulation of argon CCPs with copper electrodes, listed in table 5.1 (processes 1–11), as a function of the kinetic energy.

ions), and cause the excitation or ionization of the gas atoms as well. Cu atoms can also be scattered elastically with the gas atoms, but they do not cause excitation or ionization. The cross sections for these elementary collisions used in the simulation are taken from [5, 130–132].

An Ar atom after an elastic ion-atom collision is treated as fast atom and its motion is traced in case its energy is above 23 eV which is the threshold energy for electronic excitation in a collision between two Ar atoms. After losing its energy surplus above this threshold due to elastic collisions or reaching an electrode, the fast atom is lost. Cu atoms are created by the sputtering of the copper electrodes upon impact of energetic heavy particles. Cu atoms are tracked in the discharge gap until hitting one of the electrodes. The density of Cu atoms remains three orders of magnitude lower than the background argon density, so the latter is considered to remain unchanged in the simulations.

5.2.2 Surface processes

In the PIC/MCC simulations, the interactions of plasma particles with the electrodes are treated by realistic models, which are presented below.

5.2.2.1 Electron – surface interactions

Regarding the electrons hitting the electrodes, the surface model introduced in [81] and used already in the previous chapter is applied, considering the total secondary electron (SE) yield as the sum of the elastic reflection yield, the inelastic backscattering yield and the electron-induced SE (δ-electrons, true SE) yield, where all these processes have coefficients depending on the electron energy and angle of incidence, see equation 4.1. The surface properties of the copper electrode are considered in the model by tuning its 10 input parameters based on empirical data from literature [16, 19, 21, 133–135]. We use the same parameters as Sun *et al.* [103] for Cu surfaces. These parameters are given in table 5.2. Figure 5.2(a) shows the total SEE coefficient σ and the partial emission coefficients η_e, η_i and δ, for Cu surfaces as a function of the electron energy, at normal incidence.

TABLE 5.2: Parameters of the realistic model of electron induced SEE for Cu surfaces.

#	Parameter	Description	Value	References
1	ε_0	threshold energy for electron induced SEE	15 eV	[17]
2	$\varepsilon_{\mathrm{max},0}$	energy of PE at the maximum emission	400 eV	[17]
3	$\sigma_{\mathrm{max},0}$	maximum emission at normal incidence	1.2	[17]
4	k_{s}	smoothness factor of the surface	1	[21]
5	$\varepsilon_{\mathrm{e},0}$	threshold energy for elastic reflection	0 eV	
6	$\varepsilon_{\mathrm{e},\mathrm{max}}$	energy of PE at the maximum elastic reflection	10 eV	[18]
7	$\eta_{\mathrm{e},\mathrm{max}}$	maximum of the elastic reflection	0.1	[18]
8	Δ_{e}	control parameter for the decay of η_{e}	5 eV	
9	r_{e}	portion of elastically reflected electrons	0.03	[17]
10	r_{i}	portion of inelastically reflected electrons	0.07	[17]

5.2.2.2 Heavy particle – surface interactions

Secondary electron emission

In case of Ar^+ ions and Ar^f fast neutrals, SEE is considered by energy-dependent coefficients proposed by Phelps *et al.* in [5]. This was an experimental work in which SE yields for different metal surfaces bombarded by Ar^+ ions and Ar^f fast neutrals
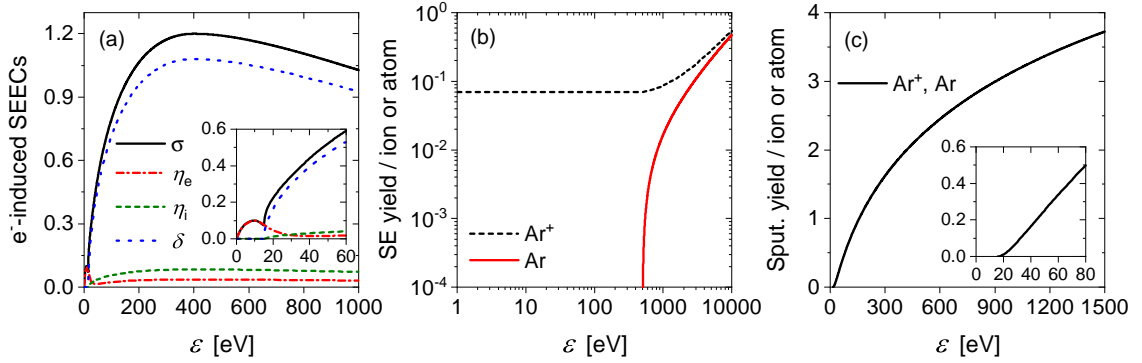
FIGURE 5.2: (a) SEE coefficient for copper surface: the total electron induced
SEE coefficient (σ) and the partial emission coefficients of elastic reflection (η_{e}),
inelastic reflection (η_{i}), and electron induced SEE (δ) as a function of the incident
electron energy, for normal incidence. (b) SE yields on clean metal surfaces due to
Ar^+ ions and Ar neutrals, as a function of the incident particle energy, calculated
according to [5]. (c) The sputtering yield for Ar^+ ions and Ar atoms on Cu
surfaces as a function of the particle energy, calculated according to [136]. Figure
reused from [72].

were measured and analytical formulas were proposed to calculate them as func-
tions of the particle energy. (This model was already mentioned in the introductory
chapter, see section 1.2.3.1 and figure 1.5.) In case of both species, two different
yields were proposed corresponding to the surface conditions: dirty and clean sur-
faces. In this context, dirty means typical laboratory conditions (e.g. chemically
and/or mechanically cleaned, gas-covered or oxidized surfaces), while clean refers to
atomically clean conditions (e.g. heavily sputtered surfaces in ultra high vacuum
environment). In the current study, the electrodes are assumed to be atomically
clean, since the discharges are operated at low pressure (0.5 Pa) and high voltage
amplitude (1000 V), i.e. under conditions when significant sputtering of the elec-
trodes is caused by the bombardment of plasma particles. The SEE coefficients for
Ar^+ (γ_{i}) and Ar^{f} (γ_{a}) in case of clean surface are shown in figure 5.2(b), as functions
of the particle energy. In the simulation, the effective SEE coefficient is calculated
as [98, 137]

$$\gamma^* = \frac{\sum_{k=1}^{N_{\mathrm{i}}} \gamma_{\mathrm{i}}(\varepsilon_k) + \sum_{k=1}^{N_{\mathrm{a}}} \gamma_{\mathrm{a}}(\varepsilon_k)}{N_{\mathrm{i}}}, \tag{5.1}$$

where N_i and N_a are the total number of Ar^+ ions and Ar^f (fast) atoms that hit a given electrode in one RF period, and ε_k is the energy of the k-th ion or fast atom when it reaches the electrode.

Sputtering

In addition to the realistic models of the interaction of electrons and heavy particles with the electrode surface, the sputtering of the electrode material by energetic heavy particles is also modelled, which produces Cu atoms. The sputtering yields for the different heavy particle species (Ar^+ and Ar^f) depend on the energy of incidence (ε). I use the empirical formula of Matsunami *et al.* [136] to calculate the sputtering yields. The resulting sputtering coefficient as a function of the heavy particle energy is shown in figure 5.2(c).

5.2.3   Discharge conditions

In the current study, the discharges are operated at a low pressure of 0.5 Pa and a high RF voltage amplitude of 1000 V. The gap between the electrodes is 6.7 cm, and the temperature of the background gas is assumed to be 400 K, as a result of gas heating. These conditions are close to the ones applied in the previous chapter for oxygen, being relevant for plasma processing applications. The driving voltage waveform is composed of N harmonics of the fundamental frequency, which is $f = 13.56$ MHz. The composition of this kind of waveforms follows the concept introduced in the introductory chapter, section 1.2.5.2: see the mathematical form of multifrequency waveforms in equation 1.25 and the illustration of such waveforms in figure 1.11. In this study, a maximum of four harmonics is applied ($1 \leq N \leq 4$) to drive the discharge, the value of the total voltage amplitude, ϕ_{tot} is 1000 V. The phase shifts of the odd harmonics are zero ($\theta_1 = \theta_3 = 0°$), while the phase shifts of the even harmonics are varied, always being equal ($0° < \theta = \theta_2 = \theta_4 < 180°$).
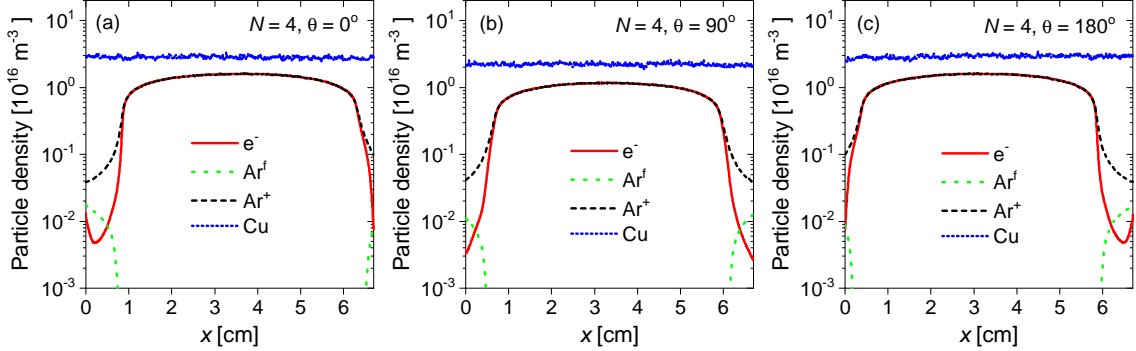
5.3 Results

FIGURE 5.3: Time-averaged density profiles of electrons, heavy particles and copper atoms in the discharge gap in case of $N = 4$ harmonics, for different values of θ: (a) $\theta = 0°$, (b) $\theta = 90°$ and (c) $\theta = 180°$. Discharge conditions: $p = 0.5$ Pa, $L = 6.7$ cm, $f = 13.56$ MHz, $N = 4$, $\phi_{\text{tot}} = 1000$ V [72].

In figure 5.3, the time-averaged density profiles of the plasma species are shown for various values of θ in case of $N = 4$ harmonics. The density of Cu atoms sputtered from the electrodes is also shown. In the case when $\theta = 90°$, all particle species have symmetric density distribution, as the waveform is symmetric (its time-average is zero). The electrons and the Ar^+ ions have distributions characteristic of electropositive CCPs. The Ar^f neutrals appear in the sheaths as they are created in charge exchange (elastic backscattering) collisions. The Cu atoms are evenly distributed in the gap due to the low pressure and the equal net sources at the electrodes. At $\theta = 0°$ and $\theta = 180°$, the density distributions of all particles become asymmetric. The sheath becomes very narrow at the grounded electrode. The sputtered atom density is slightly higher at one electrode than the other: at $\theta = 0°$, in the vicinity of the powered electrode we find about 10% higher Cu density than near the grounded electrode, while the opposite is true at $\theta = 180°$. This is a consequence of the net sources of Cu atoms being different at the two electrodes, caused by the asymmetry of the driving waveform.

If more than one harmonic is applied in the driving waveform of a CCP, a DC self-bias can develop as it was explained in section 1.2.5.2. Figure 5.4 shows the
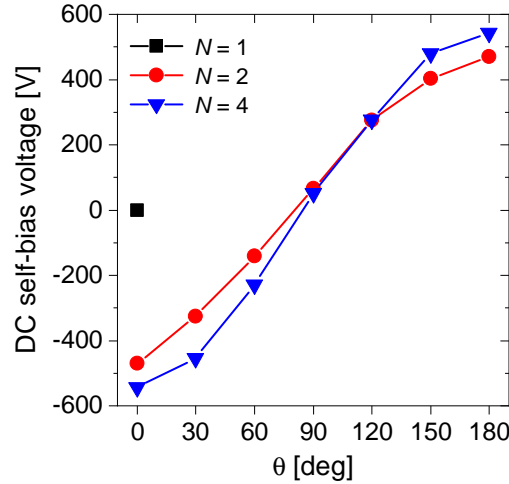
FIGURE 5.4: The DC self-bias voltage as a function of the phase angle(s) of the even harmonics (θ), for different numbers of harmonics applied (N). Discharge conditions: $p = 0.5$ Pa, $L = 6.7$ cm, $f = 13.56$ MHz, $\phi_{\text{tot}} = 1000$ V [72].

dependence of the DC self-bias voltage on the (identical) phase angles of the even harmonics, θ, for different numbers of applied harmonics. The self-bias can be adjusted by changing θ: at $N = 2$, it ranges from -470 V to 470 V as θ is varied from 0° to 180°, and at $N = 4$, it ranges from -540 V to 540 V.

The first column of figure 5.5 shows the mean energies of Ar^+ ions and Ar^f atoms at the two electrodes as a function of θ, for different numbers of applied harmonics. By changing θ, the mean energies of heavy particles at the electrodes can be tuned efficiently. In case of $N = 4$ consecutive harmonics, the mean energy of Ar^+ ions (figure 5.5(a)) increases by a factor of about 7 at the grounded electrode (from about 80 eV to about 560 eV) and decreases in the same range at the powered electrode, as θ is varied from 0° to 180°. At $N = 2$, the ion energy changes by a factor of 4 (between 130 eV and 530 eV) at the same time. The mean energy of Ar^f neutrals (figure 5.5(d)) varies in a similar way: it changes by a factor of about 5.4 (from about 45 eV to 245 eV) in case of four harmonics, and by a factor of about 3.3 (between 70 eV and 230 eV) in case of two harmonics, as θ is varied from 0° to 180°.

As the surface processes depend on the particle energy, the interactions of heavy
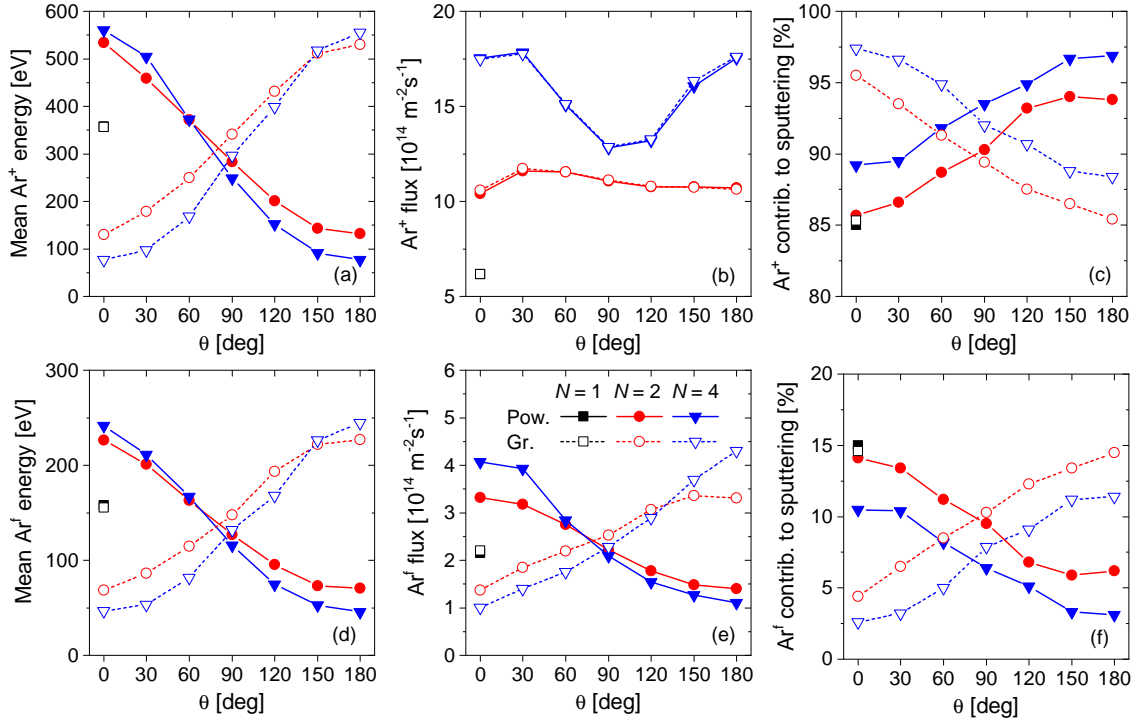
FIGURE 5.5: The mean energy (first column) and flux (second column) of Ar^+ ions (first row) and Ar^f neutrals (second row) at the electrodes, as well as their relative contributions to the sputtering of the Cu electrodes (third column) for different numbers of applied harmonics, N, as a function of the phase angle(s), θ. Discharge conditions: $p = 0.5$ Pa, $L = 6.7$ cm, $f = 13.56$ MHz, $\phi_{tot} = 1000$ V. Note that the symbols completely overlap in some cases. The legend in panel (e) applies to all panels [72].

particles with the electrodes, such as SEE and sputtering, are expected to be affected by the variation of θ. An earlier PIC/MCC simulation study of low-pressure discharges operated in argon, driven by TVWs (in which the heavy-particle induced SEE was modelled realistically but the electron induced SEE was ignored), showed that the phase angle of the even harmonics affected the effective γ^* up to a factor of 4 [71]. The explanation was that the variation of θ resulted in the variation of the heavy-particle energies and consequently the variation of the energy-dependent SE yields. However, under the conditions in the current study, γ^* is hardly affected by changing the phase shifts of the driving harmonics. For all N and θ, γ^* is calculated to be ~ 0.07 at both electrodes. The reason is that under particle energies below 500 eV, the SE yield for ions takes a constant value of 0.07 and it is zero for fast

atoms (see figure 5.2(b)). γ^* values up to 3% higher than 0.07 are obtained for the highest ion energies appearing in this study. Note that the energy of fast atoms is always below the SEE limit, see figure 5.5(d).

The fluxes of heavy particles at the electrodes also change while θ is varied between 0° and 180°, see the second column of figure 5.5. The Ar^f flux decreases at the powered electrode and increases at the grounded electrode (for $N > 1$, see figure 5.5(e)). The reason of this is that the sheath width also changes as θ is varied (see later in figure 5.7), and so the region where fast atoms are created. Note that the fluxes of Ar$^+$ ions are equal at the two electrodes for any θ and N, because the ionization dynamics is nonlocal (see later in figure 5.7).
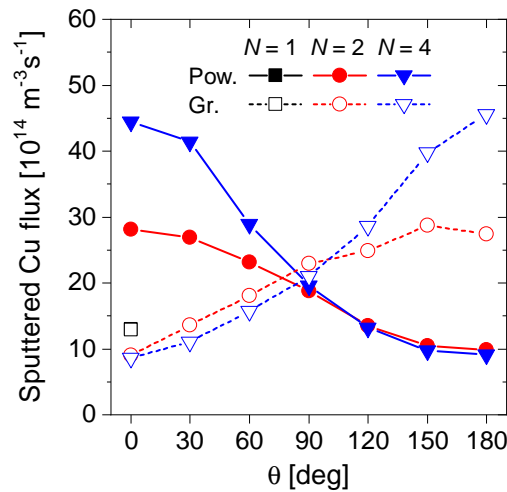

FIGURE 5.6: The (outgoing) flux of sputtered Cu atoms at both electrodes as a function of θ, for different numbers of applied harmonics. Discharge conditions: $p = 0.5$ Pa, $L = 6.7$ cm, $f = 13.56$ MHz, $\phi_{tot} = 1000$ V. Note that the symbols completely overlap in some cases [72].

Ar$^+$ ions and Ar^f atoms with energies observed here (see figure 5.5) cause significant sputtering of the Cu electrodes (see the energy-dependent sputtering yield in figure 5.2(c)). Most of the sputtering (85% to 95% depending on N and θ) is caused by Ar$^+$ ions (see figure 5.5(c)), while Ar^f atoms cause 5% to 15% of the sputtering (see figure 5.5(f)). For a given θ, more harmonics (N) result in more sputtering by Ar$^+$ ions and less by Ar^f atoms at both electrodes. As both the mean energy and the flux

of Ar^f atoms at the electrodes varies as a function of θ, the relative contribution of Ar^f atoms to the total sputtering decreases at the powered electrode and increases at the grounded one while θ is tuned from $0°$ to $180°$ (see figure 5.5(f)). Consequently, the contribution of sputtering at the same time increases at the powered electrode and decreases at the grounded electrode (figure 5.5(c)).

The flux of sputtered Cu atoms escaping the electrodes also depends on the phase angle θ and the number of harmonics. This is shown in figure 5.6. For $N = 2$, changing θ from $0°$ to $180°$ results in a variation of the sputtered Cu flux at the electrodes by ~ 3 times (increase at the grounded electrode and decrease at the powered electrode). Similar trends can be observed in case of four harmonics, in a wider range of the sputtered Cu flux: a difference by a factor of 5 is obtained between $0°$ and $180°$. These results show that in CCPs driven by TVWs, the phase angle θ serves as a control parameter for the flux of sputtered atoms at the electrodes. At $\theta = 90°$, the sputtered flux is similar at the two electrodes. At $\theta = 0°$, the sputtered Cu flux is much higher at the powered electrode than at the grounded electrode (3 times more in case $N = 2$ and 5 times more when $N = 4$), while at $\theta = 180°$ it is the other way around (see figure 5.6).
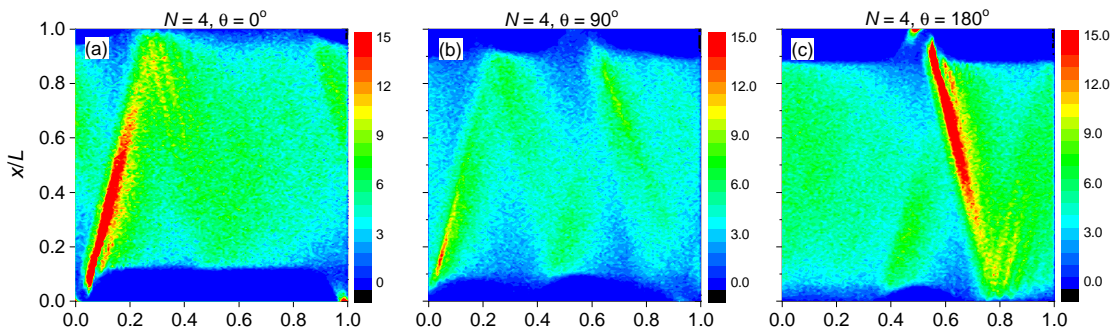
FIGURE 5.7: Spatio-temporal distribution of the ionization rate (in units of 10^{20} $m^{-3}s^{-1}$) for $N = 4$ applied harmonics, for different phase angles: (a) $\theta = 0°$, (b) $\theta = 90°$ and (c) $\theta = 180°$. The powered electrode is at $x/L = 0$, while the grounded electrode is at $x/L = 1$. T_{RF} indicates one period of the fundamental frequency. Discharge conditions: $p = 0.5$ Pa, $L = 6.7$ cm, $f = 13.56$ MHz, $N = 4$ [72].

In figure 5.7, the spatio-temporal distribution of the ionization rate is shown in case of four harmonics, for phase angles (θ) of 0°, 90° and 180°. The discharge operates in the α-mode in all cases, i.e. the main ionization pattern appears at sheath expansion. The sheaths are asymmetric at $\theta = 0°$: at the powered electrode the sheath is much wider compared to the grounded electrode side, and it is expanded during most of the RF period. In parallel, the ionization is asymmetric as well (figure 5.7(a)): strong α-mode ionization is observable in the vicinity of the powered electrode only. For $\theta = 180°$, the ionization dynamics is similar at the grounded electrode half a period later (figure 5.7(c)). At $\theta = 90°$ the ionization is more balanced (figure 5.7(b)). At this angle, the ionization peaks are much weaker than at the extreme values of the phase angle. This causes lower Ar^+ ion fluxes to the electrodes at $\theta = 90°$ than at $\theta = 0°$ and $\theta = 180°$ (see figure 5.5(b) for $N = 4$).

5.4 Summary

In this chapter, the surface processes in CCPs relevant for plasma processing applications were studied by PIC/MCC simulations. The discharges were driven by tailored voltage waveforms. In the simulations, a novel and complex approach of the interactions of plasma particles with the electrode surfaces was used. For the electron–surface interactions, a realistic model was applied, taking electron-induced SEE into account. SEE induced by heavy particles (ions and fast neutrals) was also considered by an approach considering the particle energy and the surface conditions. In addition to these, the sputtering of the copper electrodes by heavy particles was also included in the surface model, by an energy-dependent yield. In the multifrequency driving voltage waveforms up to four harmonics of the fundamental frequency ($f = 13.56$ MHz) was included, and the phases of the even harmonics, $\theta = \theta_2 = \theta_4$ were varied. In all simulations, the pressure was 0.5 Pa, the gap length was 6.7 cm and the total voltage amplitude was fixed at 1000 V.

When more than one harmonics were applied ($2 \leq N \leq 4$) to drive the discharge, a DC self-bias voltage was observed to form, which was found to be adjustable by changing the phase angle(s) of the even harmonics, θ. By increasing the number of harmonics in the driving voltage waveform, the DC self-bias was controllable in a wider interval. As a result, the mean energy of ions and fast neutrals colliding with the copper electrodes changed by factors up to 7 and 5.4, respectively.

Since SEE and the sputtering caused by heavy particles depend on the particle energies, changing θ affected these surface processes as well. By tuning the phase angle θ of the even harmonics between $0°$ and $180°$, efficient control of the sputtering yield was achieved. At $N = 2$, the sputtered Cu flux changed by 3 times at both electrodes by increasing θ. At $N = 4$, a difference by a factor of 5 was achieved in the sputtering yield. These results showed that in CCPs driven by TVWs, the phase angle θ serves as a control parameter for the flux of sputtered atoms at the electrodes.

Chapter 6

Conclusions

Although capacitively coupled plasmas (CCPs) have been studied extensively by experimental and computational methods during the last decades, and these plasmas have a wide range of industrial applications, several aspects of the physics of such systems has not been understood yet. The current thesis aimed at the fundamental understanding of the electron power absorption and ionization dynamics of CCPs and the interactions of plasma particles with the electrodes in different gases, under various discharge conditions. As a result of these studies, the optimization of plasma processing applications is facilitated based on a scientific approach.

To achieve the objectives of this work, I have carried out modelling and simulation of RF plasmas along with experiments. In particle-in-cell/Monte Carlo collisions (PIC/MCC) simulations, the realistic modelling of the surface processes between the plasma particles and the electrode material have only recently become a central issue. In order to achieve a detailed understanding of the role of plasma–surface interactions in CCPs, I implemented various surface models into PIC/MCC simulation codes, based on experimental results available in the literature.

6.1 Thesis points

The scientific findings presented in the current thesis are summarized in the following points.

1. For neon CCPs with stainless steel electrodes, I determined the unknown effective ion-induced secondary electron emission coefficient (γ) by a revised version of the γ-CAST method, a computationally assisted spectroscopic technique. A γ coefficient of 0.29 provided the best agreement between the Ne $2p_1$ excitation rate obtained from phase-resolved optical emission spectroscopy (PROES) measurement and PIC/MCC simulation [94]/[TP1].

2. I demonstrated that PROES measurements does not always probe the operation mode of a CCP. In fact, such measurements are only able to provide information about the excitation rate of the measured excited state from the ground state, which can have different spatio-temporal distribution compared to the ionization rate, based on which the operation mode of a discharge can be defined. I found that the reason behind this is the different shape of the electron-impact cross sections of the excitation of the measured excited state and the ionization. In neon CCPs, this difference in the cross sections makes high-energy γ-electrons within the sheath more likely to cause ionization than excitation, resulting in a γ-mode discharge operation unobservable by PROES measurement of the Ne $2p_1$ state [94]/[TP1].

3. I implemented a realistic model for the interaction of electrons with the electrode surface into the PIC/MCC simulation code of oxygen CCPs. Based on this, I found that electron-induced secondary electrons (δ-electrons) together with ion-induced secondary electrons (γ-electrons) play a crucial role in the ionization dynamics in high-voltage and low-pressure oxygen CCPs, which significantly increases the charged particle densities and the $O_2(a^1\Delta_g)$ metastable density, leading to the

decrease of the electronegativity of the discharge. Parallel to this, the role of the DA-mode decreases in the ionization dynamics when electron-induced secondary electron emission is treated realistically in the simulation, and a transition to the α-mode occurs with emergence of an additional ionizing electron beam at the phase of partial sheath collapse [129]/[TP2].

4. In addition to electron induced secondary electron emission, I added a realistic implementation of secondary electron emission induced by O_2^+ ions to the PIC/MCC simulation code. This way the effects of secondary electrons on the discharge characteristics were even more pronounced at high driving voltages. The simulations showed that above 800 V, the effective γ^* ion induced secondary electron emission coefficient was higher than 0.4, reaching a value of 0.62 at the highest driving voltage of 1200 V. While the electron density at 1200 V was an order of magnitude higher according to the surface model containing a realistic implementation of the electron–surface interaction compared to a simple model considering constant electron reflection coefficient and neglecting secondary electron emission, a difference by a factor of 50 was found in the electron densities between the simplest model and the realistic model which contained realistic approaches for both O_2^+ ions and electrons. Moreover, I found that the oxygen discharge became electropositive above 1000 V, when both electron and ion induced secondary electron emission were treated realistically [129]/[TP2].

5. By PIC/MCC simulations of CCPs driven by multifrequency waveforms (a sinusoidal waveform containing additional harmonics of the base harmonic) in argon at high voltage and low pressure, I found that the DC self-bias between the electrodes can be modulated between a negative and a positive peak of ≈ 500 V by changing the phase angle of the even (second and fourth) harmonics. Via the modulation of the self bias, the mean energy of heavy particles (argon ion and argon fast atom) at the electrodes can also be tuned within a range of a factor of 7 in the current

study. With the use of a realistic surface model treating heavy particle induced and electron induced secondary electron emission with energy-dependent coefficients and accounting for the sputtering of the copper electrodes with a realistic coefficient as well, I demonstrated that the sputtering yield of copper atoms caused by heavy particle impact can also be efficiently controlled by changing the phase angle of the even harmonics between $0°$ and $180°$ in the driving voltage waveforms. The domain over which the sputtered atom flux can be varied is enlarged by adding more harmonics to the driving voltage waveform. When two harmonics are used, the sputtering varies between the two electrodes by a factor of 3, while this difference rises up to a factor of 5 in case of four harmonics [72]/[TP3].

List of Publications

Thesis publications

[**TP1**]   B Horváth, A Derzsi, J Schulze, I Korolov, P Hartmann, Z Donkó: Experimental and kinetic simulation study of electron power absorption mode transitions in capacitive radiofrequency discharges in neon. *Plasma Sources Science and Technology* **29** 055002, 2020. *DOI: 10.1088/1361-6595/ab8176*

[**TP2**]   B Horváth, Z Donkó, J Schulze, A Derzsi: The critical role of electron induced secondary electrons in high-voltage and low-pressure capacitively coupled oxygen plasmas. *Plasma Sources Science and Technology* **31** 045025, 2022. *DOI: 10.1088/1361-6595/ac64bd*

[**TP3**]   A Derzsi, B Horváth, Z Donkó, J Schulze: Surface processes in low-pressure capacitive radio frequency discharges driven by tailored voltage waveforms. *Plasma Sources Science and Technology* **29** 074001, 2020. *DOI: 10.1088/1361-6595/ab9156*

Other publications

1. B Horváth, M Daksha, I Korolov, A Derzsi, J Schulze: The role of electron induced secondary electron emission from SiO_2 surfaces in capacitively coupled radio frequency plasmas operated at low pressures. *Plasma Sources Science and Technology* **26** 124001, 2017. *DOI: 10.1088/1361-6595/aa963d*

2. B Horváth, J Schulze, Z Donkó, A Derzsi: The effect of electron induced secondary electrons on the characteristics of low-pressure capacitively coupled radio frequency plasmas. *Journal of Physics D: Applied Physics* **51** 355204, 2018. *DOI: 10.1088/1361-6463/aad47b*

3. A Derzsi, B Horváth, I Korolov, Z Donkó, J Schulze: Heavy-particle induced secondary electrons in capacitive radio frequency discharges driven by tailored voltage waveforms. *Journal of Applied Physics* **126** 043303, 2019. *DOI: 10.1063/1.5100508*

4. Z Donkó, A Derzsi, M Vass, B Horváth, S Wilczek, B Hartmann, P Hartmann: eduPIC: an introductory particle based code for radio-frequency plasma simulation. *Plasma Sources Science and Technology* **30** 095017, 2021. *DOI: 10.1088/1361-6595/ac0b55*

5. M Vass, S Wilczek, A Derzsi, B Horváth, P Hartmann, Z Donkó: Evolution of the bulk electric field in capacitively coupled argon plasmas at intermediate pressures. *Plasma Sources Science and Technology* **31** 045017, 2022. *DOI: 10.1088/1361-6595/ac6361*

6. A Derzsi, P Hartmann, M Vass, B Horváth, M Gyulai, I Korolov, J Schulze, Z Donkó: Electron power absorption in capacitively coupled neon-oxygen plasmas: a comparison of experimental and computational results. *Plasma Sources Science and Technology* **31** 085009, 2022. *DOI: 10.1088/1361-6595/ac7b45*

7. K Nösges, M Klich, A Derzsi, B Horváth, J Schulze, R P Brinkmann, T Mussenbrock, S Wilczek: Nonlocal dynamics of secondary electrons in capacitively coupled radio frequency discharges. *Plasma Sources Science and Technology*, accepted for publication, 2023. DOI: *10.1088/1361-6595/ace848*

8. A Derzsi, M Vass, R Masheyeva, B Horváth, Z Donkó, P Hartmann: Frequency-dependent electron power absorption mode transitions in capacitively coupled argon-oxygen plasmas. Submitted to *Plasma Sources Science and Technology*, 2023.

9. C-W Park, B Horváth, A Derzsi, J Schulze, J H Kim, Z Donkó, H-C Lee: Experimental validation of particle-in-cell/Monte Carlo collisions simulations in low-pressure neon capacitively coupled plasmas. Submitted to *Plasma Sources Science and Technology*, 2023.

Bibliography

[1] Z. Donkó, *Alacsonyhőmérsékletű plazmafizika.* Budapest: Wigner Research Centre for Physics, 2020.

[2] M. A. Lieberman and A. J. Lichtenberg, *Principles of Plasma Discharges and Materials Processing, 2nd Edition.* Wiley, 2005.

[3] T. Makabe and Z. Petrović, *Plasma Electronics: Applications in Microelectronic Device Fabrication* (Taylor & Francis, London, 2006).

[4] R. P. Brinkmann, "Beyond the step model: Approximate expressions for the field in the plasma boundary sheath," *J. Appl. Phys.*, vol. 102, no. 9, 2007.

[5] A. V. Phelps and Z. L. Petrović, "Cold-cathode discharges and breakdown in argon: surface and gas phase production of secondary electrons," *Plasma Sources Sci. Technol.*, vol. 8, no. 3, 1999.

[6] R. Behrisch, *Sputtering by particle bombardment, vol. I: Physical sputtering of single-elements solids.* Heidelberg: Springer Berlin, 1 ed., 2005.

[7] P. R. Thornton, *Scanning Electron Microscopy: Applications to Materials and Device Science.* London: Chapman and Halls Ltd., 1968.

[8] N. Gascon, M. Dudeck, and S. Barral, "Wall material effects in stationary plasma thrusters. I. Parametric studies of an SPT-100," *Phys. Plasmas*, vol. 10, no. 10, pp. 4123–4136, 2003.

[9] D. Sydorenko, A. Smolyakov, I. Kaganovich, and Y. Raitses, "Kinetic simulation of secondary electron emission effects in Hall thrusters," *Phys. Plasmas*, vol. 13, no. 1, pp. 1–4, 2006.

[10] I. D. Kaganovich, Y. Raitses, D. Sydorenko, and A. Smolyakov, "Kinetic effects in a Hall thruster discharge," *Phys. Plasmas*, vol. 14, no. 5, 2007.

[11] F. Taccogna, S. Longo, M. Capitelli, and R. Schneider, "Anomalous transport induced by sheath instability in Hall effect thrusters," *Appl. Phys. Lett.*, vol. 94, no. 25, 2009.

[12] T. Lafleur, S. D. Baalrud, and P. Chabert, "Theory for the anomalous electron transport in Hall effect thrusters. I. Insights from particle-in-cell simulations," *Phys. Plasmas*, vol. 23, no. 5, 2016.

[13] J. P. Boeuf, "Tutorial: Physics and modeling of Hall thrusters," *J. Appl. Phys.*, vol. 121, no. 1, 2017.

[14] H. Bruining, *Physics and Applications of Secondary Electron Emission.* London: Pergamon Press, 1954.

[15] A. Dekker, "Secondary electron emission," in *Advances in Research and Applications* (F. Seitz and D. Turnbull, eds.), vol. 6 of *Solid State Physics*, pp. 251–311, Academic Press, 1958.

[16] H. Seiler, "Secondary electron emission in the scanning electron microscope," *J. Appl. Phys.*, vol. 54, no. 11, 1983.

[17] V. P. Gopinath, J. P. Verboncoeur, and C. K. Birdsall, "Multipactor electron discharge physics using an improved secondary emission model," *Phys. Plasmas*, vol. 5, no. 5, pp. 1535–1540, 1998.

[18] S. Barral, K. Makowski, Z. Peradzyński, N. Gascon, and M. Dudeck, "Wall material effects in stationary plasma thrusters. II. Near-wall and in-wall conductivity," *Phys. Plasmas*, vol. 10, no. 10, pp. 4137–4152, 2003.

[19] D. Ruzic, R. Moore, D. Manos, and S. Cohen, "Secondary Electron Yields of Carbon-Coated and Polished Stainless Steel.," *J. Vac. Sci. Technol.*, vol. 20, no. 4, pp. 1313–1316, 1981.

[20] S. Yu, W. Yi, T. Jeong, J. Lee, J. Heo, C. S. Lee, D. Jeon, and J. M. Kim, "Secondary electron emission for layered structures," *J. Vac. Sci. Technol. A Vacuum, Surfaces, Film.*, vol. 20, no. 3, pp. 950–952, 2002.

[21] J. Vaughan, "A new formula for secondary emission yield," *IEEE Transactions on Electron Devices*, vol. 36, no. 9, pp. 1963–1967, 1989.

[22] A. Derzsi, T. Lafleur, J.-P. Booth, I. Korolov, and Z. Donkó, "Experimental and simulation study of a capacitively coupled oxygen discharge driven by tailored voltage waveforms," *Plasma Sources Sci. Technol.*, vol. 25, p. 15004, dec 2016.

[23] J. Schulze, A. Derzsi, K. Dittmann, T. Hemke, J. Meichsner, and Z. Donkó, "Ionization by drift and ambipolar electric fields in electronegative capacitive radio frequency plasmas," *Phys. Rev. Lett.*, vol. 107, no. 27, pp. 1–5, 2011.

[24] P. Belenguer and J. P. Boeuf, "Transition between different regimes of rf glow discharges," *Phys. Rev. A*, vol. 41, no. 8, pp. 4447–4459, 1990.

[25] V. A. Schweigert, A. L. Alexandrov, S. F. Gimelshtein, and M. S. Ivanov, "Fast approach to kinetic simulations of RF discharge in plasma reactors," *Plasma Sources Sci. Technol.*, vol. 9, pp. B1–B3, feb 1999.

[26] J. Schulze, T. Kampschulte, D. Luggenhölscher, and U. Czarnetzki, "Diagnostics of the plasma series resonance effect in radio-frequency discharges," *J. Phys. Conf. Ser.*, vol. 86, no. 1, 2007.

[27] J. Schulze, B. G. Heil, D. Luggenhölscher, R. P. Brinkmann, and U. Czarnetzki, "Stochastic heating in asymmetric capacitively coupled RF discharges," *J. Phys. D. Appl. Phys.*, vol. 41, no. 19, 2008.

[28] J. Schulze, B. G. Heil, D. Luggenhölscher, and U. Czarnetzki, "Electron beams in capacitively coupled radio-frequency discharges," *IEEE Trans. Plasma Sci.*, vol. 36, no. 4 PART 1, pp. 1400–1401, 2008.

[29] T. Mussenbrock, R. P. Brinkmann, M. A. Lieberman, A. J. Lichtenberg, and E. Kawamura, "Enhancement of Ohmic and Stochastic Heating by Resonance Effects in Capacitive Radio Frequency Discharges: A Theoretical Approach," *Phys. Rev. Lett.*, vol. 101, p. 85004, aug 2008.

[30] M. M. Turner, "Collisionless heating in radio-frequency discharges: A review," *J. Phys. D. Appl. Phys.*, vol. 42, no. 19, 2009.

[31] C. Böhm and J. Perrin, "Retarding-field analyzer for measurements of ion energy distributions and secondary electron emission coefficients in low-pressure radio frequency discharges," *Rev. Sci. Instrum.*, vol. 64, no. 1, pp. 31–44, 1993.

[32] J. P. Booth, G. Curley, D. Marić, and P. Chabert, "Dual-frequency capacitive radiofrequency discharges: Effect of low-frequency power on electron density and ion flux," *Plasma Sources Sci. Technol.*, vol. 19, no. 1, 2010.

[33] Z. Donkó, J. Schulze, P. Hartmann, I. Korolov, U. Czarnetzki, and E. Schüngel, "The effect of secondary electrons on the separate control of ion energy and flux in dual-frequency capacitively coupled radio frequency discharges," *Appl. Phys. Lett.*, vol. 97, no. 8, 2010.

[34] J. Schulze, Z. Donkó, E. Schüngel, and U. Czarnetzki, "Secondary electrons in dual-frequency capacitive radio frequency discharges," *Plasma Sources Sci. Technol.*, vol. 20, no. 4, 2011.

[35] Z. M. Q. Liu, Y. Liu, T. Samir, "Numerical study of effect of secondary electron emission on discharge characteristics in low pressure capacitive RF argon discharge," *Phys. Plasmas*, vol. 21, no. 8, p. 083511, 2014.

[36] T. Hemke, D. Eremin, T. Mussenbrock, A. Derzsi, Z. Donkó, K. Dittmann, J. Meichsner, and J. Schulze, "Ionization by bulk heating of electrons in capacitive radio frequency atmospheric pressure microplasmas," *Plasma Sources Sci. Technol.*, vol. 22, p. 015012, feb 2013.

[37] L. Bischoff, G. Hübner, I. Korolov, Z. Donkó, P. Hartmann, T. Gans, J. Held, V. Schulz-Von Der Gathen, Y. Liu, T. Mussenbrock, and J. Schulze, "Experimental and computational investigations of electron dynamics in micro atmospheric pressure radio-frequency plasma jets operated in He/N 2 mixtures," *Plasma Sources Sci. Technol.*, vol. 27, p. 125009, dec 2018.

[38] Y. X. Liu, E. Schüngel, I. Korolov, Z. Donkó, Y. N. Wang, and J. Schulze, "Experimental Observation and Computational Analysis of Striations in Electronegative Capacitively Coupled Radio-Frequency Plasmas," *Phys. Rev. Lett.*, vol. 116, p. 255002, jun 2016.

[39] Y. X. Liu, I. Korolov, E. Schüngel, Y. N. Wang, Z. Donkó, and J. Schulze, "Striations in electronegative capacitively coupled radio-frequency plasmas: Analysis of the pattern formation and the effect of the driving frequency," *Plasma Sources Sci. Technol.*, vol. 26, p. 055024, apr 2017.

[40] L. Wang, D. Q. Wen, Q. Z. Zhang, Y. H. Song, Y. R. Zhang, and Y. N. Wang, "Disruption of self-organized striated structure induced by secondary electron emission in capacitive oxygen discharges," *Plasma Sources Sci. Technol.*, vol. 28, p. 055007, may 2019.

[41] L. Wang, P. Hartmann, Z. Donkó, Y.-H. Song, and J. Schulze, "2D particle-in-cell simulations of geometrically asymmetric low-pressure capacitive RF plasmas driven by tailored voltage waveforms," *Plasma Sources Sci. Technol.*, vol. 30, no. 5, p. 54001, 2021.

[42] Z. Donkó, J. Schulze, U. Czarnetzki, A. Derzsi, P. Hartmann, I. Korolov, and E. Schüngel, "Fundamental investigations of capacitive radio frequency plasmas: Simulations and experiments," *Plasma Phys. Control. Fusion*, vol. 54, no. 12, 2012.

[43] W. Tsai, "High selectivity plasma etching of silicon dioxide with a dual frequency 27/2 MHz capacitive radio frequency discharge," *J. Vac. Sci. Technol. B Microelectron. Nanom. Struct.*, vol. 14, no. 5, p. 3276, 1996.

[44] T. Kitajima, Y. Takeo, Z. L. Petrović, and T. Makabe, "Functional separation of biasing and sustaining voltages in two-frequency capacitively coupled plasma," *Appl. Phys. Lett.*, vol. 77, no. 4, pp. 489–491, 2000.

[45] P. C. Boyle, A. R. Ellingboe, and M. M. Turner, "Independent control of ion current and ion impact energy onto electrodes in dual frequency plasma devices," *J. Phys. D. Appl. Phys.*, vol. 37, no. 5, pp. 697–701, 2004.

[46] P. C. Boyle, A. R. Ellingboe, and M. M. Turner, "Electrostatic modelling of dual frequency rf plasma discharges," *Plasma Sources Sci. Technol.*, vol. 13, no. 3, pp. 493–503, 2004.

[47] J. K. Lee, O. V. Manuilenko, N. Y. Babaeva, H. C. Kim, and J. W. Shon, "Ion energy distribution control in single and dual frequency capacitive plasma sources," *Plasma Sources Sci. Technol.*, vol. 14, no. 1, pp. 89–97, 2005.

[48] Z. Donkó and Z. L. Petrović, "Analysis of a capacitively coupled dual-frequency CF4 discharge," *Japanese J. Appl. Physics, Part 1 Regul. Pap. Short Notes Rev. Pap.*, vol. 45, no. 10 B, pp. 8151–8156, 2006.

[49] S. Wang, X. Xu, and Y. N. Wang, "Numerical investigation of ion energy distribution and ion angle distribution in a dual-frequency capacitively coupled plasma with a hybrid model," *Phys. Plasmas*, vol. 14, no. 11, 2007.

[50] A. Derzsi, E. Schüngel, Z. Donkó, and J. Schulze, "Electron heating modes and frequency coupling effects in dual-frequency capacitive CF4plasmas," *Open Chem.*, vol. 13, no. 1, pp. 346–361, 2015.

[51] P. Hartmann, L. Wang, K. Nösges, B. Berger, S. Wilczek, R. P. Brinkmann, T. Mussenbrock, Z. Juhasz, Z. Donkó, A. Derzsi, E. Lee, and J. Schulze, "Charged particle dynamics and distribution functions in low pressure dual-frequency capacitively coupled plasmas operated at low frequencies and high voltages," *Plasma Sources Sci. Technol.*, vol. 29, no. 7, p. 75014, 2020.

[52] M. Vass, L. Wang, S. Wilczek, T. Lafleur, R. P. Brinkmann, Z. Donkó, and J. Schulze, "Frequency coupling in low-pressure dual-frequency capacitively coupled plasmas revisited based on the Boltzmann term analysis," *Plasma Sources Sci. Technol.*, vol. 31, no. 11, 2022.

[53] T. Gans, J. Schulze, D. O'Connell, U. Czarnetzki, R. Faulkner, A. R. Ellingboe, and M. M. Turner, "Frequency coupling in dual frequency capacitively coupled radio-frequency plasmas," *Appl. Phys. Lett.*, vol. 89, no. 26, pp. 1–4, 2006.

[54] M. M. Turner and P. Chabert, "Collisionless heating in capacitive discharges enhanced by dual-frequency excitation," *Phys. Rev. Lett.*, vol. 96, no. 20, pp. 1–4, 2006.

[55] J. Schulze, T. Gans, D. O'Connell, U. Czarnetzki, A. R. Ellingboe, and M. M. Turner, "Space and phase resolved plasma parameters in an industrial dual-frequency capacitively coupled radio-frequency discharge," *J. Phys. D. Appl. Phys.*, vol. 40, no. 22, pp. 7008–7018, 2007.

[56] D. O'Connell, T. Gans, E. Semmler, and P. Awakowicz, "The role of the relative voltage and phase for frequency coupling in a dual-frequency capacitively coupled plasma," *Appl. Phys. Lett.*, vol. 93, no. 8, 2008.

[57] J. Waskoenig and T. Gans, "Nonlinear frequency coupling in dual radio-frequency driven atmospheric pressure plasmas," *Appl. Phys. Lett.*, vol. 96, no. 18, pp. 3–6, 2010.

[58] A. Derzsi, Z. Donkó, and J. Schulze, "Coupling effects of driving frequencies on the electron heating in electronegative capacitive dual-frequency plasmas," *J. Phys. D. Appl. Phys.*, vol. 46, no. 48, 2013.

[59] U. Czarnetzki, J. Schulze, E. Schüngel, and Z. Donkó, "The electrical asymmetry effect in capacitively coupled radio-frequency discharges," *Plasma Sources Sci. Technol.*, vol. 20, no. 2, 2011.

[60] J. Schulze, E. Schüngel, Z. Donkó, and U. Czarnetzki, "The electrical asymmetry effect in multi-frequency capacitively coupled radio frequency discharges," *Plasma Sources Sci. Technol.*, vol. 20, no. 1, 2011.

[61] B. G. Heil, U. Czarnetzki, R. P. Brinkmann, and T. Mussenbrock, "On the possibility of making a geometrically symmetric RF-CCP discharge electrically asymmetric," *J. Phys. D. Appl. Phys.*, vol. 41, no. 16, 2008.

[62] Z. Donkó, J. Schulze, B. G. Heil, and U. Czarnetzki, "PIC simulations of the separate control of ion flux and energy in CCRF discharges via the electrical asymmetry effect," *J. Phys. D. Appl. Phys.*, vol. 42, no. 2, 2009.

[63] J. Schulze, E. Schüngel, U. Czarnetzki, and Z. Donkó, "Optimization of the electrical asymmetry effect in dual-frequency capacitively coupled radio frequency discharges: Experiment, simulation, and model," *J. Appl. Phys.*, vol. 106, no. 6, pp. 1–6, 2009.

[64] E. Schüngel, J. Schulze, Z. Donkó, and U. Czarnetzki, "Power absorption in electrically asymmetric dual frequency capacitive radio frequency discharges," *Phys. Plasmas*, vol. 18, no. 1, pp. 3–8, 2011.

[65] J. Schulze, A. Derzsi, and Z. Donkó, "Electron heating and the electrical asymmetry effect in dual-frequency capacitive CF4 discharges," *Plasma Sources Sci. Technol.*, vol. 20, no. 4, pp. 20–23, 2011.

[66] I. Korolov, Z. Donkó, U. Czarnetzki, and J. Schulze, "The effect of the driving frequencies on the electrical asymmetry of dual-frequency capacitively coupled plasmas," *J. Phys. D. Appl. Phys.*, vol. 45, no. 46, 2012.

[67] A. Derzsi, I. Korolov, E. Schüngel, Z. Donkó, and J. Schulze, "Electron heating and control of ion properties in capacitive discharges driven by customized voltage waveforms," *Plasma Sources Sci. Technol.*, vol. 22, no. 6, p. 65009, 2013.

[68] E. Schüngel, S. Brandt, Z. Donkó, I. Korolov, A. Derzsi, and J. Schulze, "Electron heating via self-excited plasma series resonance in geometrically symmetric multi-frequency capacitive plasmas," *Plasma Sources Sci. Technol.*, vol. 24, no. 4, p. 44009, 2015.

[69] A. R. Gibson and T. Gans, "Controlling plasma properties under differing degrees of electronegativity using odd harmonic dual frequency excitation," *Plasma Sources Sci. Technol.*, vol. 26, no. 11, p. 115007, 2017.

[70] S. Brandt, B. Berger, Z. Donkó, A. Derzsi, E. Schüngel, M. Koepke, and J. Schulze, "Control of charged particle dynamics in capacitively coupled plasmas driven by tailored voltage waveforms in mixtures of Ar and CF4," *Plasma Sources Sci. Technol.*, vol. 28, no. 9, 2019.

[71] A. Derzsi, B. Horváth, I. Korolov, Z. Donkó, and J. Schulze, "Heavy-particle induced secondary electrons in capacitive radio frequency discharges driven by tailored voltage waveforms," *J. Appl. Phys.*, vol. 126, no. 4, 2019.

[72] A. Derzsi, B. Horváth, Z. Donkó, and J. Schulze, "Surface processes in low-pressure capacitive radio frequency discharges driven by tailored voltage waveforms," *Plasma Sources Sci. Technol.*, vol. 29, no. 7, 2020.

[73] C. K. Birdsall and A. B. Langdon, *Plasma Physics via Computer Simulation* (McGraw-Hill, New York, 1985).

[74] R. W. Hockney and J. W. Eastwood, *Computer Simulation Using Particles.* USA: Taylor & Francis, Inc., 1988.

[75] Z. Donkó, "Particle simulation methods for studies of low-pressure plasma sources," *Plasma Sources Sci. Technol.*, vol. 20, no. 2, 2011.

[76] Z. Donkó, A. Derzsi, M. Vass, B. Horváth, S. Wilczek, B. Hartmann, and P. Hartmann, "EduPIC: An introductory particle based code for radio-frequency plasma simulation," *Plasma Sources Sci. Technol.*, vol. 30, no. 9, 2021.

[77] A. Derzsi, P. Hartmann, M. Vass, B. Horváth, M. Gyulai, I. Korolov, J. Schulze, and Z. Donkó, "Electron power absorption in capacitively coupled neon-oxygen plasmas: a comparison of experimental and computational results," *Plasma Sources Sci. Technol.*, vol. 31, no. 8, 2022.

[78] A. Derzsi, I. Korolov, E. Schüngel, Z. Donkó, and J. Schulze, "Effects of fast atoms and energy-dependent secondary electron emission yields in PIC/MCC simulations of capacitively coupled plasmas," *Plasma Sources Sci. Technol.*, vol. 24, no. 3, p. 034002, 2015.

[79] H. Hannesdottir and J. T. Gudmundsson, "The role of the metastable $O_2(b1\Sigma+g)$ and energy-dependent secondary electron emission yields in capacitively coupled oxygen discharges," *Plasma Sources Sci. Technol.*, vol. 25, no. 5, 2016.

[80] M. Daksha, A. Derzsi, S. Wilczek, J. Trieschmann, T. Mussenbrock, P. Awakowicz, Z. Donkó, and J. Schulze, "The effect of realistic heavy particle induced secondary electron emission coefficients on the electron power absorption dynamics in single- and dual-frequency capacitively coupled plasmas," *Plasma Sources Sci. Technol.*, vol. 26, no. 8, 2017.

[81] B. Horváth, M. Daksha, I. Korolov, A. Derzsi, and J. Schulze, "The role of electron induced secondary electron emission from SiO2 surfaces in capacitively coupled radio frequency plasmas operated at low pressures," *Plasma Sources Sci. Technol.*, vol. 26, no. 12, 2017.

[82] J. T. Gudmundsson and A. Proto, "Electron heating mode transitions in a low pressure capacitively coupled oxygen discharge," *Plasma Sources Sci. Technol.*, vol. 28, no. 4, 2019.

[83] L. Wang, P. Hartmann, Z. Donkó, Y.-H. Song, and J. Schulze, "Effects of structured electrodes on electron power absorption and plasma uniformity in capacitive RF discharges," *Journal of Vacuum Science & Technology A*, vol. 39, 10 2021. 063004.

[84] L. Wang, M. Vass, Z. Donkó, P. Hartmann, A. Derzsi, Y. H. Song, and J. Schulze, "Magnetic attenuation of the self-excitation of the plasma series resonance in low-pressure capacitively coupled discharges," *Plasma Sources Sci. Technol.*, vol. 30, no. 10, 2021.

[85] T. Gans, V. Schulz-von Der Gathen, and H. F. Döbele, "Prospects of phase resolved optical emission spectroscopy as a powerful diagnostic tool for RF-discharges," *Contrib. to Plasma Phys.*, vol. 44, no. 5-6, pp. 523–528, 2004.

[86] T. Gans, D. O'Connell, V. Schulz-Von Der Gathen, and J. Waskoenig, "The challenge of revealing and tailoring the dynamics of radio-frequency plasmas," *Plasma Sources Sci. Technol.*, vol. 19, no. 3, 2010.

[87] J. Schulze, E. Schüngel, Z. Donkó, D. Luggenhölscher, and U. Czarnetzki, "Phase resolved optical emission spectroscopy: A non-intrusive diagnostic to study electron dynamics in capacitive radio frequency discharges," *J. Phys. D. Appl. Phys.*, vol. 43, no. 12, 2010.

[88] NIST Atomic Spectra Database, `https://physics.nist.gov/cgi-bin/ASD/lines1.pl?spectra=Ne&limits_type=0&low_w=&upp_w=&unit=1&`

```
submit=Retrieve+Data&de=0&format=0&line_out=0&en_unit=0&output=
0&bibrefs=1&page_size=15&show_obs_wl=1&show_calc_wl=1&unc_out=
1&order_out=0&max_low_enrg=&show_av=2&max_upp_enrg=&tsb_value=
0&min_str=&A_out=0&intens_out=on&max_str=&allowed_out=1&forbid_
out=1&min_accur=&min_intens=&conf_out=on&term_out=on&enrg_out=
on&J_out=on
```
, retrieved on September 5, 2019.

[89] J. E. Chilton, M. D. Stewart, and C. C. Lin, "Electron-impact excitation cross sections of neon," *Phys. Rev. A - At. Mol. Opt. Phys.*, vol. 61, no. 5, p. 12, 2000.

[90] U. Czarnetzki, G. Heil, J. Schulze, Z. Donkó, T. Mussenbrock, and P. Brinkmann, "The Electrical Asymmetry Effect - A novel and simple method for separate control of ion energy and flux in capacitively coupled RF discharges," *J. Phys. Conf. Ser.*, vol. 162, 2009.

[91] I. Korolov, A. Derzsi, Z. Donkó, and J. Schulze, "The influence of the secondary electron induced asymmetry on the electrical asymmetry effect in capacitively coupled plasmas," *Appl. Phys. Lett.*, vol. 103, p. 064102, aug 2013.

[92] T. Lafleur, P. Chabert, and J. P. Booth, "Secondary electron induced asymmetry in capacitively coupled plasmas," *J. Phys. D. Appl. Phys.*, vol. 46, no. 13, 2013.

[93] M. Daksha, B. Berger, E. Schuengel, I. Korolov, A. Derzsi, M. Koepke, Z. Donkó, and J. Schulze, "A computationally assisted spectroscopic technique to measure secondary electron emission coefficients in radio frequency plasmas," *J. Phys. D. Appl. Phys.*, vol. 49, no. 23, 2016.

[94] B. Horváth, A. Derzsi, J. Schulze, I. Korolov, P. Hartmann, and Z. Donkó, "Experimental and kinetic simulation study of electron power absorption mode transitions in capacitive radiofrequency discharges in neon," *Plasma Sources Sci. Technol.*, vol. 29, no. 5, 2020.

[95] Biagi-v7.1 database, `www.lxcat.net`, retrieved on April 8, 2019. Cross sections extracted from PROGRAM MAGBOLTZ, VERSION 7.1 JUNE 2004.

[96] A. V. Phelps, unpublished, `ftp://jila.colorado.edu/collision_data/`, retrieved on August 22, 2005.

[97] R. Kollath, *Encyclopedia of Physics*, vol. XXI, ed. S. Flügge (Springer, Berlin, 1956), p. 264.

[98] Z. Donkó, "Apparent secondary-electron emission coefficient and the voltage-current characteristics of argon glow discharges," *Phys. Rev. E - Stat. Physics, Plasmas, Fluids, Relat. Interdiscip. Top.*, vol. 64, no. 2, p. 9, 2001.

[99] O. Braginsky, A. Kovalev, D. Lopaev, O. Proshina, T. Rakhimova, A. Vasilieva, D. Voloshin, and S. Zyryanov, "Experimental and theoretical study of dynamic effects in low-frequency capacitively coupled discharges," *J. Phys. D. Appl. Phys.*, vol. 45, no. 1, 2012.

[100] H. Hannesdottir and J. T. Gudmundsson, "On singlet metastable states, ion flux and ion energy in single and dual frequency capacitively coupled oxygen discharges," *J. Phys. D. Appl. Phys.*, vol. 50, no. 17, p. 175201, 2017.

[101] A. Proto and J. T. Gudmundsson, "The influence of secondary electron emission and electron reflection on a capacitively coupled oxygen discharge," *Atoms*, vol. 6, no. 4, 2018.

[102] M. Daksha, A. Derzsi, Z. Mujahid, D. Schulenberg, B. Berger, Z. Donkó, and J. Schulze, "Material dependent modeling of secondary electron emission coefficients and its effects on PIC/MCC simulation results of capacitive RF plasmas," *Plasma Sources Sci. Technol.*, vol. 28, no. 3, 2019.

[103] J. Y. Sun, D. Q. Wen, Q. Z. Zhang, Y. X. Liu, and Y. N. Wang, "The effects of electron surface interactions in geometrically symmetric capacitive RF plasmas in the presence of different electrode surface materials," *Phys. Plasmas*, vol. 26, no. 6, 2019.

[104] B. Horváth, J. Schulze, Z. Donkó, and A. Derzsi, "The effect of electron in-
duced secondary electrons on the characteristics of low-pressure capacitively
coupled radio frequency plasmas," *J. Phys. D. Appl. Phys.*, vol. 51, no. 35,
2018.

[105] J. Y. Sun, Q. Z. Zhang, J. R. Liu, Y. H. Song, and Y. N. Wang, "Electrical
asymmetry effect in inhomogeneously magnetized capacitively coupled plas-
mas," *Plasma Sources Sci. Technol.*, vol. 29, no. 11, 2020.

[106] P. Hartmann, L. Wang, K. Nösges, B. Berger, S. Wilczek, R. P. Brinkmann,
T. Mussenbrock, Z. Juhasz, Z. Donkó, A. Derzsi, E. Lee, and J. Schulze,
"Control of electron velocity distributions at the wafer by tailored voltage
waveforms in capacitively coupled plasmas to compensate surface charging in
high-aspect ratio etch features," *J. Phys. D. Appl. Phys.*, vol. 54, no. 25, 2021.

[107] L. Wang, P. Hartmann, Z. Donkó, Y. H. Song, and J. Schulze, "2D Particle-
in-cell simulations of charged particle dynamics in geometrically asymmetric
low pressure capacitive RF plasmas," *Plasma Sources Sci. Technol.*, vol. 30,
no. 8, 2021.

[108] F. X. Bronold, K. Matyash, D. Tskhakaya, R. Schneider, and H. Fehske,
"Radio-frequency discharges in oxygen: I. Particle-based modelling," *J. Phys.
D. Appl. Phys.*, vol. 40, no. 21, pp. 6583–6592, 2007.

[109] K. Matyash, R. Schneider, K. Dittmann, J. Meichsner, F. X. Bronold, and
D. Tskhakaya, "Radio-frequency discharges in oxygen: III. Comparison of
modelling and experiment," *J. Phys. D. Appl. Phys.*, vol. 40, no. 21, pp. 6601–
6607, 2007.

[110] A. Derzsi, B. Bruneau, A. R. Gibson, E. Johnson, D. O'Connell, T. Gans,
J. P. Booth, and Z. Donkó, "Power coupling mode transitions induced by
tailored voltage waveforms in capacitive oxygen discharges," *Plasma Sources
Sci. Technol.*, vol. 26, no. 3, p. 34002, 2017.

[111] Z. Donkó, A. Derzsi, M. Vass, J. Schulze, E. Schuengel, and S. Hamaguchi, "Ion energy and angular distributions in low-pressure capacitive oxygen RF discharges driven by tailored voltage waveforms," *Plasma Sources Sci. Technol.*, vol. 27, no. 10, p. 104008, 2018.

[112] L. Wang, D. Q. Wen, P. Hartmann, Z. Donkó, A. Derzsi, X. F. Wang, Y. H. Song, Y. N. Wang, and J. Schulze, "Electron power absorption dynamics in magnetized capacitively coupled radio frequency oxygen discharges," *Plasma Sources Sci. Technol.*, vol. 29, no. 10, 2020.

[113] M. Vass, S. Wilczek, T. Lafleur, R. P. Brinkmann, Z. Donkó, and J. Schulze, "Electron power absorption in low pressure capacitively coupled electronegative oxygen radio frequency plasmas," *Plasma Sources Sci. Technol.*, vol. 29, p. 25019, feb 2020.

[114] M. Vass, S. Wilczek, T. Lafleur, R. P. Brinkmann, Z. Donkó, and J. Schulze, "Collisional electron momentum loss in low temperature plasmas: On the validity of the classical approximation," *Plasma Sources Sci. Technol.*, vol. 30, no. 6, 2021.

[115] J. T. Gudmundsson, D. I. Snorrason, and H. Hannesdottir, "The frequency dependence of the discharge properties in a capacitively coupled oxygen discharge," *Plasma Sources Sci. Technol.*, vol. 27, no. 2, 2018.

[116] A. Proto and J. T. Gudmundsson, "The role of surface quenching of the singlet delta molecule in a capacitively coupled oxygen discharge," *Plasma Sources Sci. Technol.*, vol. 27, no. 7, p. 74002, 2018.

[117] I. Childres, L. A. Jauregui, J. Tian, and Y. P. Chen, "Effect of oxygen plasma etching on graphene studied using Raman spectroscopy and electronic transport measurements," *New J. Phys.*, vol. 13, 2011.

[118] X. Xue, K. Zhou, J. Cai, Q. Wang, and Z. Wang, "Reactive ion etching of poly (cyclohexene carbonate) in oxygen plasma," *Microelectron. Eng.*, vol. 191, pp. 1–9, 2018.

[119] X. Lu, H. Huang, N. Nemchuk, and R. S. Ruoff, "Patterning of highly oriented pyrolytic graphite by oxygen plasma etching," *Appl. Phys. Lett.*, vol. 75, no. 2, pp. 193–195, 1999.

[120] N. J. Chou, C. H. Tang, J. Paraszczak, and E. Babich, "Mechanism of oxygen plasma etching of polydimethyl siloxane films," *Appl. Phys. Lett.*, vol. 46, no. 1, pp. 31–33, 1985.

[121] M. A. Hartney, D. W. Hess, and D. S. Soane, "Oxygen plasma etching for resist stripping and multilayer lithography," *J. Vac. Sci. Technol. B Microelectron. Process. Phenom.*, vol. 7, no. 1, pp. 1–13, 1989.

[122] Z. Donkó, A. Derzsi, I. Korolov, P. Hartmann, S. Brandt, J. Schulze, B. Berger, M. Koepke, B. Bruneau, E. Johnson, T. Lafleur, J. P. Booth, A. R. Gibson, D. O'Connell, and T. Gans, "Experimental benchmark of kinetic simulations of capacitively coupled plasmas in molecular gases," *Plasma Phys. Control. Fusion*, vol. 60, no. 1, 2018.

[123] K. H. You, J. Schulze, A. Derzsi, Z. Donkó, H. J. Yeom, J. H. Kim, D. J. Seong, and H.-C. Lee, "Experimental and computational investigations of the effect of the electrode gap on capacitively coupled radio frequency oxygen discharges," *Phys. Plasmas*, vol. 26, no. 1, p. 13503, 2019.

[124] Biagi-v8.9 database, `www.lxcat.net`, retrieved on November 25, 2014. Cross sections extracted from PROGRAM MAGBOLTZ, VERSION 8.9 March 2010.

[125] V. Vahedi and M. Surendra, "A Monte Carlo collision model for the particle-in-cell method: applications to argon and oxygen discharges," *Comput. Phys. Commun.*, vol. 87, no. 1, pp. 179–198, 1995.

[126] J. T. Gudmundsson, E. Kawamura, and M. A. Lieberman, "A benchmark study of a capacitively coupled oxygen discharge of the oopd1 particle-in-cell Monte Carlo code," *Plasma Sources Sci. Technol.*, vol. 22, no. 3, 2013.

[127] A. Greb, K. Niemi, D. O'Connell, and T. Gans, "The influence of surface properties on the plasma dynamics in radio-frequency driven oxygen plasmas: Measurements and simulations," *Appl. Phys. Lett.*, vol. 103, no. 24, 2013.

[128] A. Greb, A. R. Gibson, K. Niemi, D. O'Connell, and T. Gans, "Influence of surface conditions on plasma dynamics and electron heating in a radio-frequency driven capacitively coupled oxygen plasma," *Plasma Sources Sci. Technol.*, vol. 24, no. 4, p. 44003, 2015.

[129] B. Horváth, Z. Donkó, J. Schulze, and A. Derzsi, "The critical role of electron induced secondary electrons in high-voltage and low-pressure capacitively coupled oxygen plasmas," *Plasma Sources Sci. Technol.*, vol. 31, no. 4, 2022.

[130] A. V. Phelps, "The application of scattering cross sections to ion flux models in discharge sheaths," *J. Appl. Phys.*, vol. 76, no. 2, pp. 747–753, 1994.

[131] A. V. Phelps, "Cross Sections and Swarm Coefficients for Nitrogen Ions and Neutrals in N2 and Argon Ions and Neutrals in Ar for Energies from 0.1 eV to 10 keV," *Journal of Physical and Chemical Reference Data*, vol. 20, pp. 557–573, 05 1991.

[132] J. Lindhard, M. Scharff, and H. E. Schioett, "Range concepts and heavy ion ranges (notes on atomic collisions, ii)," *Kgl. Danske Videnskab. Selskab. Mat. Fys. Medd.*

[133] C. G. Walker, M. M. El-Gomati, A. M. Assa'd, and M. Zadražil, "The secondary electron emission yield for 24 solid elements excited by primary electrons in the range 250-5000 ev: A theory/experiment comparison," *Scanning*, vol. 30, no. 5, pp. 365–380, 2008.

[134] Y. Raitses, I. D. Kaganovich, A. Khrabrov, D. Sydorenko, N. J. Fisch, and A. Smolyakov, "Effect of secondary electron emission on electron cross-field current in e × B discharges," *IEEE Trans. Plasma Sci.*, vol. 39, no. 4 PART 1, pp. 995–1006, 2011.

[135] L. A. Gonzalez, M. Angelucci, R. Larciprete, and R. Cimino, "The secondary electron yield of noble metal surfaces," *AIP Adv.*, vol. 7, no. 11, pp. 1–7, 2017.

[136] N. Matsunami, Y. Yamamura, Y. Itikawa, N. Itoh, Y. Kazumata, S. Miyagawa, K. Morita, R. Shimizu, and H. Tawara, "Energy dependence of the ion-induced sputtering yields of monatomic solids," *At. Data Nucl. Data Tables*, vol. 31, no. 1, pp. 1–80, 1984.

[137] Z. Donkó, "Heavy-particle hybrid modeling of transients in a direct-current argon discharge," *J. Appl. Phys.*, vol. 88, no. 5, pp. 2226–2233, 2000.

Abstract

Capacitively coupled plasmas (CCPs) are widely applied in modern plasma processing technologies like etching, deposition and cleaning. The substrate located on one of the electrodes undergoes bombardment by plasma particles, so the control of the energy and the flux of these particles at the electrodes, which determine the various surface processes, is crucial. A detailed understanding of the complex physics of CCPs facilitates the knowledge-based optimization of plasma processing applications.

The current thesis aims the fundamental understanding of low-pressure CCPs operated under various conditions. The electron power absorption and ionization dynamics and the role of surface processes in CCPs are addressed, combining particle-based computational studies with experiments. The accurate modelling of various surface processes in particle-in-cell/Monte Carlo collisions simulations of CCPs is in focus of this work. New details of the electron power absorption and the ionization dynamics in CCPs are discovered, and the effects of various surface processes on the plasma parameters are revealed. Unkown surface coefficients are determined and the applicability of spectroscopic methods to probe the discharge operation mode is also investigated. Moreover, efficient control of the sputtering yield is achieved in low-pressure CCPs, which can facilitate the optimization of plasma processing applications based on fundamental understanding of the dynamics of CCPs.